UNIVERSITY OF CAPE TOWN
CENTRE FOR CATALYSIS RESEARCH

In situ study of Co_3O_4 morphology in the CO-PROX reaction

by
Motlokoa Khasu
BSc Eng. Chemical Engineering, University of Cape Town, South Africa

Submitted in fulfilment
of the requirements for the degree of
Master of Science in Chemical Engineering, University of Cape Town
Rondebosch, South Africa

Acknowledgements

I would like to give my sincerest gratitude to all those who made this work a success:

- Above all, I would like to thank God for giving me the strength and helping me to grind away.
- A huge thank you goes out to my supervisors, Dr. Nico Fischer and Prof. Michael Claeys for the support, inspiration and guidance through it all. Much appreciated.
- A big thank you to my colleagues for their support and friendly environment they provided, especially Moritz Wolf and Thulani Nyathi for assisting me with testing instruments and algorithms to analyse my data.
- Thank you to Mohamed Jaffer, Innocent Shuro and Miranda Waldron from Electron Microscope Unit, University of Cape Town, for making time to analyse my samples and to teach me how to operate TEM. I would also like to thank Zulfa le Riche and Jessica Heynes for AAS/ICP and BET analysis, not forgetting Anna Petersen for her uber help with TPR. Rachel Cupido, Waldo Koorts, Gideon Kaufmann and Chantal Le Roux, thank you for assistance in the laboratory.
- To my undergraduate final year sponsor whom I wish to meet one day, thank you very much for selflessly giving out to the needy, I would not have finished my undergraduate studies to do this work if it was not for your kindness. May God bless you and give you a long healthy life. Thank you.
- I would also like to thank The Catalysis Centre and NRF - University of Cape Town for their financial support in my academic development. You change lives.

Synopsis

The preferential oxidation (PROX) reaction is one of the most used and most effective processes for the removal of trace amounts of carbon monoxide (0.5–1.0 vol.%) from a reformate stream. Tricobalt tetraoxide (Co_3O_4) has been found to be a potential catalyst candidate for CO-PROX in H_2 rich reformate gas as it shows good activity for CO oxidation and could therefore be a good alternative to the rare and expensive platinum group metals (PGM) normally used.

The high activity of Co_3O_4 nanocrystals is attributed to the number of exposed Co^{3+} active sites available for reaction. However, at the conditions suitable for CO-PROX, deactivation is likely to occur through the reduction of Co^{3+} active sites to Co^{2+} and metallic Co^0, and the formation of carbonate species on the catalyst surface at elevated temperatures. Catalytic properties of Co_3O_4 nanocrystals (activity, selectivity, stability, etc.) may depend on the morphology of the crystallites exposing different surface terminations. To obtain a concise understanding of the reaction, it is of interest to investigate the effect of different Co_3O_4 morphologies on the performance in the preferential oxidation of carbon monoxide reaction.

The objective of this study is therefore to investigate the effect of Co_3O_4 crystallite morphology, namely cubes, hexagonal platelets or sheets and belts, in CO-PROX. Utilizing *in situ* magnetic and *in situ* powder X-ray diffraction (PXRD) techniques, structural and chemical changes of the catalyst will be correlated to the observed activity and selectivity. Previous reports have shown the effect of crystallite morphology in CO oxidation in the absence of hydrogen, but to the best of our knowledge no study has investigated the morphology dependency in H_2 rich atmospheres [1,2].

Different morphologies were prepared using hydrothermal and precipitation based techniques to produce cobalt hydroxide samples, followed by a subsequent direct thermal decomposition to obtain Co_3O_4. Challenges in preparing nanocubes and nanosheets prompted the use of two synthesis techniques for both morphologies, eventually yielding two batches of nanocubes (amine and HCl nanocubes) and nanosheets (amine and NaOH nanosheets). Conventional spherical nanoparticles from the work of Nyathi [3], studying the effect of crystallite size on the CO-PROX reaction, were included in the present study to compare the activity of conventional nanoparticles with nanoparticles of different morphology.

The model catalysts were supported on Stöber spheres (SiO_2) spheres which were also prepared.

Transmission electron microscopy (TEM) and powder X-ray diffraction (PXRD) were employed extensively to monitor whether the desired morphologies and phases were successfully prepared. Other characterization techniques like X-ray photoelectron spectroscopy (XPS) and Brunauer–Emmett–Teller (BET) surface area measurements were used to get important information on the chemistry and structure of the model catalysts.

The CO-PROX experiments were conducted in the *in situ* UCT-developed magnetometer and PXRD capillary cell at temperatures between 50 and 450°C. Catalytic tests showed morphology dependent distinct temperature regions of maximum activity. In the range of 150-175°C, nanoparticles (N-nanoparticles ex. study by Nyathi [3]), amine nanosheets and nanobelts show decreasing CO oxidation activity in the order mentioned. Amine nanocubes, NaOH nanosheets and HCl nanocubes display maximum PROX activity at a higher temperature range of 225 to 250°C (Amine cubes > NaOH sheets > HCl cubes). The nanobelts and sheets are superstructures that contain small particles that catalytically behave like conventional nanoparticles. The nanocubes in turn displayed single crystal morphology and outperformed all other samples in surface specific activity. Beyond morphology, the synthesis route also affects the catalytic performance with sheets prepared in the presence of amines significantly outperforming sheets of similar geometry prepared in the presence of NaOH. None of the model catalysts retained their morphology after the temperature was ramped from 50°C to 450°C, and back to 50°C. Nanosheets and nanobelts structure collapsed while nanocubes adopted a spherical morphology. The morphological change was confirmed to take place during the final reduction step from CoO to Co^0.

The *in situ* characterisation also showed that at higher temperatures the catalysts lose their activity due to the reduction of the active Co_3O_4 phase. The catalysts were partially reduced to metallic Co^0 (other phase being CoO), which was accompanied by the formation of methane. Decreasing the temperature below 450°C resulted in the decrease in methane formation, an increase, albeit to a low absolute level, of CO_2 as well as to a re-oxidation of the metallic cobalt. Two different maxima in CO_2 formation were detected which could possibly be associated to different reaction mechanisms, namely the reverse water gas shift reaction on a metallic surface and CO-PROX on the partially re-oxidized samples.

Contents

List of figures

List of tables

Nomenclature

Abbreviations

AAS	Atomic absorption spectroscopy
BET	Brunauer-Emmett-Teller
BPR	Back pressure regulator
DOR	Degree of reduction
fcc	Face-centred cubic
FIC	Flow indication and control
GC	Gas chromatography
hcp	Hexagonal closed packed
H_2-TPR	Hydrogen temperature-programmed reduction
MFC	Mass flow controller
NTP	Normal temperature and pressure (1 atm and 293 K)
PEDGE	Penta-ethylene glycol-dodecylether
PROX	Preferential oxidation
PXRD	Powder X-ray diffraction
STEM	Scanning transmission electron microscopy
TCD	Thermal conductivity detector
TEM	Transmission electron microscopy

WGSR	Water gas shift reaction
RWGSR	Reverse water gas shift reaction
^oC	Degrees Celsius

Chemical compounds

Al_2O_3	Aluminium oxide (Alumina)
Ar	Argon
Au	Gold
CH_4	Methane
CeO_2	Ceruim dioxide
Co	Cobalt
CO	Carbon monoxide
CO_2	Carbon dioxide
H_2	Hydrogen
H_2O	Water
Co_3O_4	Tricobalt tetraoxide
$Co(NO_3)_2.6H_2O$	Cobalt (II) nitrate hexahydrate
Pt	Platinum
Rh	Rhodium
Ru	Ruthenium

SiO_2	Silicon dioxide (Silica)
TEOS	Tetraethyl orthosilicate
ZrO_2	Zirconium dioxide

Notations

d	Diameter, in nm
F	Response factor
H	Enthalpy, in kJ/mol or; external magnetic field, in kOe or T
M	Sample magnetisation, in emu or; mass loading, in g
M_{rem}	Remnant magnetisation, in emu
M_S	Saturation magnetisation, in emu
n	Molar amount or; molar flow rate, in mol/min
N_A	Avogadro's number, 6.022141·1023 mol^{-1}
S	Selectivity, in C %
T	Temperature, in °C or K
T_{50}	Temperature for a CO conversion of 50%, in °C
TC	Curie temperature, in K
$T_{Hüttig}$	Hüttig temperature, in K
$T_{melting}$	Melting temperature, in K
T_N	Néel temperature, in K

T_{Tamman}	Tamman temperature, in K
TOF	Turn over frequency, in s^{-1}
X	Conversion, in C%
Y	Yield, in C%

Greek notations

γ	Fraction of ferromagnetic material displaying remnant magnetisation, wt.-%
θ	Diffraction angle, in °
λ	Wavelength, in Å
ρ	Density, in g/cm^3
σ	Mass specific magnetisation, in emu/g or; standard deviation, in n

1 Introduction

The use of fossil fuels has revolutionised global energy supply due to their high energy density and relatively wide distribution and shaped our societal and industrial development [4]. While the importance of different fossil fuels changed over the years, about 80-90% of the global energy consumed is still fossil fuel based and will remain so in the foreseeable future (see figure 1.1) [5]. However, mostly politically motivated developments in the oil price have exerted pressure on the development and implementation of renewable energy sources in the recent years [6,7].

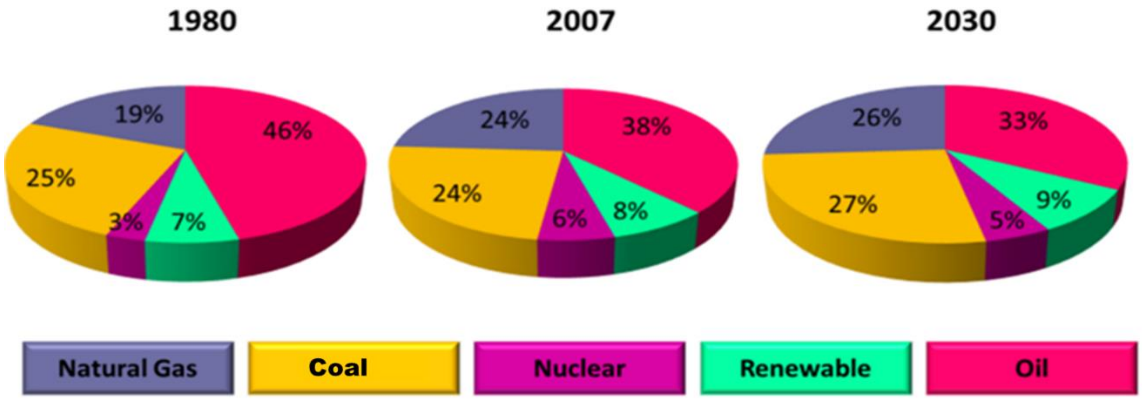

Figure 1.1: Uses of energy sources throughout the world [5]

There are two main disadvantages of fossil fuels: one is the limited availability of fossil fuels and their geographical distribution in few countries. The second crucial downside is the environmental ramifications caused by their continuous use [8]. There is therefore a growing concern about fossil fuels' impacts on the environment such as global warming, air quality deterioration, oil spills, and acid rain. This results in an increasing need for alternative fuels to replace and retrofit current technologies with clean energy, as presently used fuels threaten the future of this planet. One potentially clean alternative source of energy is hydrogen. Hydrogen is the crucial energy source best known for clean combustion and high energy density. Its demand has continuously increased due to its application in large scale industrial processes like hydrotreating and hydrocracking [9], production of methanol [10], methanol to-gasoline technology (MTG) [10], ammonia synthesis (Haber-Bosch process) [11] and Fischer-Tropsch synthesis [12].

Hydrogen is often viewed as the energy storage medium of the future [13]. Anticipated applications include power generation via fuel cells, both in stationary and mobile applications, as well as in direct combustion engines. While the availability of excess electrical power originating from renewable sources during non-peak consumption periods is forecasted and could make hydrogen generation via electrolysis of water feasible as chemical energy storage, gasification of carbon based feedstocks [14], steam and dry reforming [15] and autothermal reforming [16] are today the dominating processes to produce hydrogen, with steam reforming being by far the most popular. Biomass (agricultural residues and forest product wastes) and municipal waste can potentially be used to produce hydrogen. Biomass gasifiers resembling those of coal and solid waste gasifiers have been developed [17].

Depending on the target hydrogen consuming process, different specifications regarding purity of the hydrogen gas stream have to be considered. Hydrogen produced via any of the above mentioned carbon fuel based systems always contains carbon oxides. While carbon dioxide is inert in most downstream processes, the concentration of carbon monoxide has to be reduced significantly to avoid catalyst poisoning in, for example, fuel cell applications or the Haber-Bosch process. This is commonly achieved through a combination of an iron catalyst based high temperature and a copper catalyst based low temperature water gas shift reactions, lowering the CO content from about 10% to 1-0.1% [18]. These concentrations are still too high for fuel cell applications, as for example, the platinum based anode catalyst of a proton exchange membrane fuel cell (PEMFC) can only tolerate CO levels below 10 ppm.

There are end of pipe technologies proposed to selectively remove or minimize the amount of CO in a hydrogen rich gas stream with minimal loss of hydrogen. They include but are not limited to hydrogen selective membrane purification, pressure swing adsorption, CO methanation and preferential oxidation (PROX) of CO [19–22]. From the two catalytic processes, namely methanation and PROX, PROX has the inherent advantage that no desired product, i.e. hydrogen, is consumed under ideal operation conditions [23]. A disadvantage is naturally that oxygen has to be added to the hydrogen rich gas stream (see equation 1-1). When air is used as oxygen source the hydrogen gas stream is also further diluted by nitrogen.

$$2CO_{(g)} + O_{2(g)} \rightarrow 2CO_{2(g)} \quad \Delta H^{o}_{298} = -282.98\frac{KJ}{mol} \qquad \text{Equation 1-1}$$

From an inclusive analysis of catalytic activity, raw material abundance and cost, cobalt oxide (Co_3O_4) based catalyst have been found to be the most promising CO-PROX reaction catalyst in the purification of hydrogen for use in fuel cells [24] to potentially replace the customarily used PGM based noble metals [23]. Currently tri-cobalt tetra-oxide (Co_3O_4) is the most studied CO-PROX reaction catalyst due to its good surface redox properties that are necessary for a Mars-van Krevelen type catalytic oxidation reaction [25,26]. Unfortunately Co_3O_4 deactivates at elevated temperatures in hydrogen rich streams by reducing from active Co^{3+} to lower and inactive valencies including metallic cobalt (Co^0) [27]. Co^{2+} sites participate in the redox cycle and can be re-oxidised in the presence of oxygen to Co^{3+}, but the metallic cobalt is a potential methanation and hydrogen combustion catalyst supressing the re-oxidation pathway [25]. Studies have shown that if supported on an oxidic carrier, Co_3O_4 can be stabilized and remain active at CO-PROX relevant reaction temperatures of 80-250°C dictated by the up-steam low temperature water gas shift reactor and the downstream fuel cell. At higher temperatures deactivation through reduction is reported [1,28].

Tuning the morphology of the Co_3O_4 particles could have an effect on the activity of the catalyst as it allows for well-defined crystal planes to be exposed which are potentially not commonly exposed in ‘conventional’ spherical crystallites [2]. Nanorods of Co_3O_4 for example expose {110} planes while the surface of conventional particles is in majority comprised of a mixture of {100} and {111} planes. The different crystal planes result in different surface terminations and therefore different concentrations of active sites on the catalytic surface. It is therefore hypothesised that tuning the morphology of Co_3O_4 particles on a nanoscale level will influence the specific catalytic activity and selectivity of the CO-PROX reaction. Consequently, realising the influence the particles morphology is expected to have on activity, it becomes critical to also investigate how particle morphology affects the stability of Co_3O_4 against thermally induced deactivation processes such as reduction and sintering.

The present study focused on the *in situ* study of silica-supported tricobalt tetraoxide (Co_3O_4/SiO_2) of specific morphologies as model catalyst for CO-PROX. The project investigated the effects of Co_3O_4 morphology on thermally induced reduction in excess hydrogen using two in-house developed experimental techniques [29,30] while recording catalyst activity and selectivity.

2 Literature Review

2.1 CO Preferential oxidation reaction

The highly exothermic preferential oxidation reaction takes place during the conversion of CO with O_2 to CO_2 in a H_2-rich gas mixture as expressed by equation 1-1. Multiple other reactions can take place in the presence of H_2, CO_2 and H_2O depending on reaction conditions and catalyst composition/phase (see equations 2-1 to 2-6).

$$2H_{2(g)} + O_{2(g)} \rightarrow 2H_2O_{(g)},\ \Delta H^o_{298} = -241.82\ \frac{KJ}{mol} \qquad \text{Equation 2-1}$$

$$CO_{(g)} + H_2O_{(g)} \rightarrow CO_{2(g)} + H_{2(g)},\ \Delta H^o_{298} = -41.27\ \frac{KJ}{mol} \qquad \text{Equation 2-2}$$

$$CO_{2(g)} + H_{2(g)} \rightarrow CO_{(g)} + 2H_2O_{(g)},\ \Delta H^o_{298} = 41.27\ \frac{KJ}{mol} \qquad \text{Equation 2-3}$$

$$CO_{(g)} + 3H_{2(g)} \rightarrow CH_{4(g)} + H_2O_{(g)}, \Delta H^o_{298} = -206\ \frac{KJ}{mol} \qquad \text{Equation 2-4}$$

$$CO_{2(g)} + 4H_{2(g)} \rightarrow CH_{4(g)} + 2H_2O_{(g)}, \Delta H^o_{298} = -165\ \frac{KJ}{mol} \qquad \text{Equation 2-5}$$

$$2CO_{(g)} \rightarrow CO_{2(g)} + C_{(s)}, \Delta H^o_{298} = -172\ \frac{KJ}{mol} \qquad \text{Equation 2-6}$$

CO and H_2 oxidation (see equation 1-1 and 2-1) are the reactions that are most likely to occur in the CO-PROX reaction. They are both exothermic, irreversible and competitive [31]. While the oxidation of CO is the desired reaction, the oxidation of hydrogen results in a loss of product (hydrogen) and scavenges O_2 required for CO-PROX [32]. If dominant over CO oxidation, hydrogen oxidation can suppress the catalytic surface redox cycle and lead to catalyst deactivation. Equation 2-2 is desirable but hardly occurs in CO-PROX reaction conditions. Equation 2-3 through to Equation 2-6 fall under the category of undesired reactions and depend on reaction temperature. This means that CO-PROX reaction conditions can be controlled to prevent them. They are normally influenced by high reaction temperatures (>300°C), excess O_2 and the type of metals and supports catalyst used [33]. Equation 2-3, the reverse water gas shift reaction (RWGSR) which involves the hydrogenation of CO_2 to form CO and H_2O, occurs in the temperature range of 160-250°C [34]. As reported by Woods et al. [25], figure 2.1 below shows the decrease of CO_2 and significant increase of H_2O and CO in the temperature ranges of 160-250°C over CoO_x/CeO_2. Above 280°C, the methanation reaction is dominant.

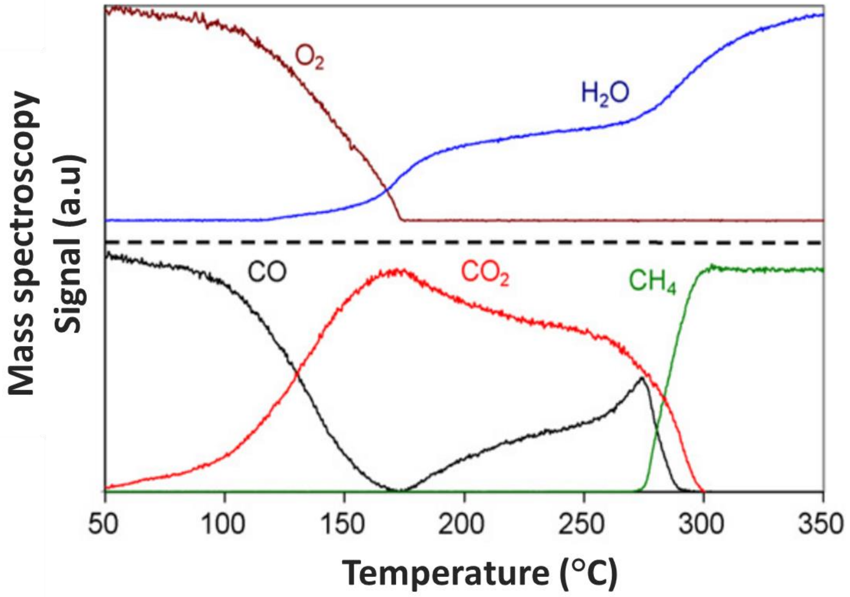

Figure 2.1 Temperature-programmed PROX reaction over CoOx/CeO_2 in the presence of 1% CO, 1% O_2, 60% H_2, balance helium [25]

Studies on catalysts for the CO-PROX reaction have gained attention in the research community over the last years. The key elements that a CO-PROX reaction catalyst must possess are high activity and selectivity as well as a tolerance to high amounts of CO_2 and H_2O present in the reformate gas [35,36]. A number of catalysts which show good activity for the CO-PROX reaction were reported [32]. They can be divided into two types. One is noble metal based catalysts that include Au, Pt, Rh, Ru and Ag. In the CO-PROX reaction typical operating temperature of 80-250°C, influenced by the PEMFC operating temperature of ~80°C and the WGSR operating temperatures of 200-250°C [37], noble metal catalysts have high CO conversion and CO_2 selectivity in the absence of CO_2 and H_2O. However, industrial hydrogen streams contain at least 10-25% CO_2 and ~10% H_2O, in which noble metal based catalytic activity and selectivity decreases [24]. The inhibiting effect of CO_2 and H_2O is reported to be due to their competition with CO for adsorption on the same active sites [38]. Noble metal based catalysts also have a problem of low oxygen content required for CO oxidation even when supported on easily reducible supports [37]. The other factor that makes noble metal based catalysts less popular is the high cost and limited availability.

The other category of catalysts suitable for CO-PROX reaction is transition metal oxide catalysts represented by Cu and Co. CuO supported on CeO_2 is the most investigated and popular catalyst for CO-PROX. Good catalytic activities and selectivity for CuO/CeO_2 were reported [39], better than those reported for noble metal based catalysts. Contrary to that, some researchers have reported deficiencies for CuO such as less H_2O resistance and large consumption of O_2 and H_2 (poor CO selectivity) [40]. On the other hand, reports on Co based catalysts claim that Co_3O_4 has better low-temperature activity, selectivity and H_2O resistance than CuO_x in excess H_2 [1,41,42].

2.2 CO-PROX for hydrogen production

Hydrogen is the simplest and most abundant gas in the universe. Despite its simplicity and abundance, it is always found in a compound because it reacts readily with other elements. As it is the lightest element, it offers the highest energy content of all fuels per unit weight. It is considered as the fuel of the future that can provide a CO_2 emission-free energy-supply [43]. Hydrogen can be stored as liquid or compressed gas bound in metal hydrides and chemical compounds, can be used to store energy from different sources and can be transported in any existing gas pipelines and distribution networks. Vehicles using hydrogen as a fuel exhaust drinkable water [44].

Hydrogen can industrially be extracted from hydrocarbon fuels such as oil, coal, natural gas as well as biomass and organic waste. It can also be produced using electrolysis by splitting water into its elemental constituents [45]. The popular hydrogen production methods are:

- Gasification or partial oxidation: In this reaction hydrocarbon or alcohol reacts with stoichiometric amounts of oxygen. The separation of oxygen used from air requires expensive equipment, but has the advantage of no heating requirement because of the exothermicity of the reaction [14,16].
- Steam reforming (STR): Traditionally called methane steam reforming, the reaction takes place between natural gas and water to produce synthesis gas. Higher carbon hydrocarbons can also be used as feedstocks in this process. Industrially, this endothermic reaction is carried out at high temperatures of 850-950°C and 15-30 pressure bars with a steam/carbon ratio around 3 [15].
- Dry reforming: The reaction takes place between hydrocarbons and carbon dioxide to produce synthesis gas. It is usually used to add value to CO_2, a greenhouse gas, but has a disadvantage of strong endothermic character with large energy requirements, optimized installations, high operational costs and catalyst deactivation due to coke formation [15].
- Autothermal reforming (ATR): It is a combination of partial oxidation (POX) and steam reforming (STR) reaction. The combination of both reactions leads to a heat integrated auto-sustainable process because the heat released from the oxidation reaction is used to drive the steam reforming reaction [16].,,,
- Pyrolysis: This is a thermal cracking process that produces CO_2, CH_4, CO, H_2O as gaseous products and carbon as a solid product. It is possible to obtain liquid products also depending on the pyrolized molecule [8].

In all the above mentioned hydrogen production process methods H_2 is always accompanied by H_2O (steam), CO and CO_2. Methane steam reforming is the most popular technique used to produce H_2. In this process, methane reacts with steam over a metal catalyst surface to produce hydrogen, carbon dioxide and trace amounts of carbon monoxide and water vapour. Downstream the reformer is the water gas shift reactors where more hydrogen is produced by reacting carbon monoxide with steam to produce hydrogen and carbon dioxide [46]. To get high purity hydrogen (<10 ppm) required by the PEMFC, the hydrogen rich gas is sent to the CO-PROX reactors to reduce CO from ~1% to less than 10 ppm.

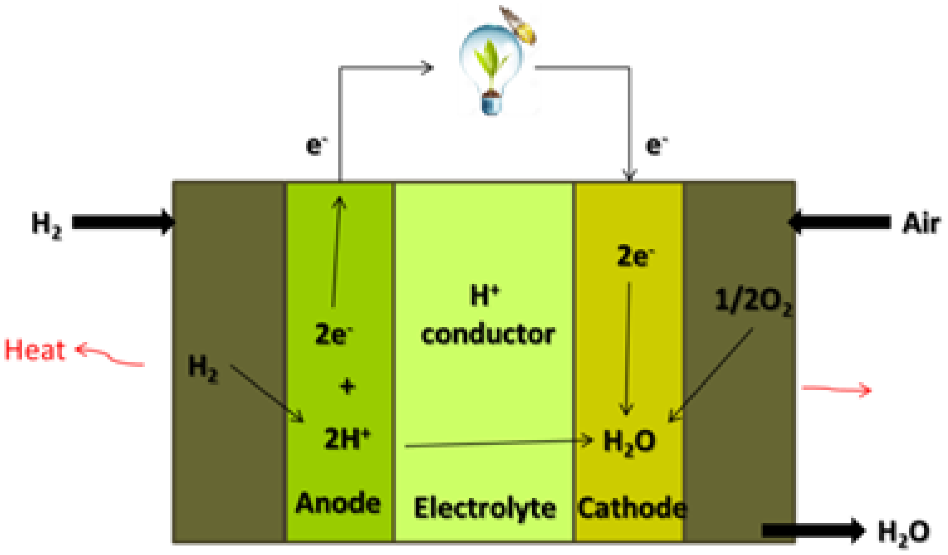

Figure 2.2: Operation of a proton exchange membrane fuel cell [5]

Figure 2.2 shows the operation of the PEMFC. Fuel cells are used to convert chemical energy stored in H_2 into electrical energy. The PEM fuel cell is one of many existing fuel cells that can offer the next generation of power sources for many applications because of high power density and easy scale-up [47]. PEM fuel cells make use of purified H_2 and oxygen from air to produce electricity. As shown in figure 2.2, H_2 enters the fuel cell at the anode where it splits into electrons and protons over a Pt catalyst. Protons and electrons are separated by a proton conducting membrane and negatively charged electrons are sent to an external circuit through wires creating electrical current. Oxygen enters the cathode side where hydrogen protons and electrons reunite, hydrogen then reacts with oxygen to form water [48]. The anode catalyst of the PEM fuel cell is the most sensitive part as it is easily poisoned by CO present in the H_2. It is therefore important to reduce the CO concentration to below 50 ppm for Pt-Ru based catalysts and 10 ppm for Pt based one.

2.3 Hydrogen production plant overview

Figure 2.3 below shows the graphical representation of an industrial process to produce hydrogen for use in a PEM fuel cell.

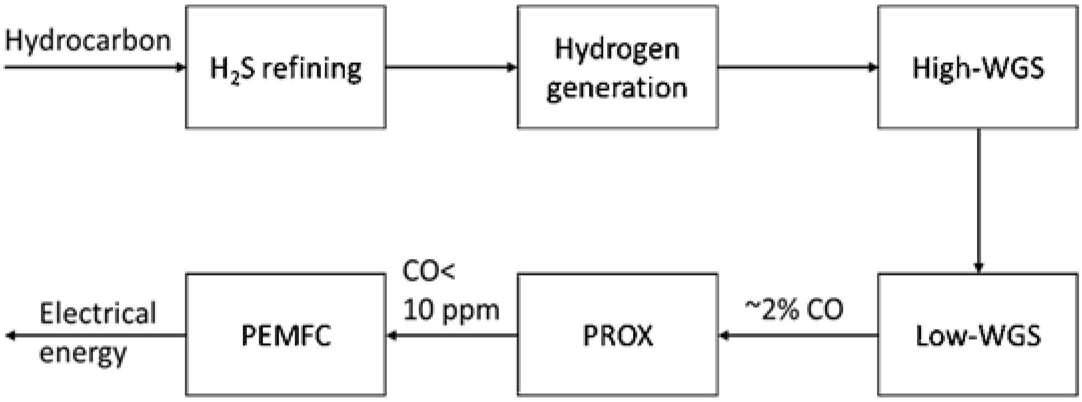

Figure 2.3: Flow diagram of hydrogen purification by CO-PROX [19]

Steam reforming of methane is regarded the best process for hydrogen production. The feed stock is first treated to remove sulphur and other contaminants. The processed feedstock and steam (3-25 bar) are converted over a nickel/alumina catalyst to syngas (mainly CO and H_2) at elevated temperatures (700-1000°C) in a reformer. The reformate gas contains about 10% CO. The heat is recovered from the syngas before the third stage, in which hydrogen yield is increased in water gas shift reactors (high and low temperature water gas shift). First the high temperature shift reaction with iron and chromium oxide catalyst is employed at 400-500°C to reduce CO to around 2-5%. Secondly the low temperature shift with $CuZnO/Al_2O_3$ is operated at 200-250°C to further reduce CO content to about 1%. The conversion of CO during the high temperature and low temperature shifts is equilibrium limited and kinetically limited respectively. In the final step, the CO-PROX reaction is employed to reduce the amount of CO to achieve the required product purity of below 10 ppm for PEMFC.

2.4 CO PROX selectivity

The basics for a good catalyst in CO-PROX systems is a high conversion of CO and a selectivity of O_2 to CO_2 over a wide temperature range (80 – 250°C) [55,56]. O_2 from air is co-fed to oxidise CO to CO_2, but also has a potential to oxidise H_2 to H_2O. Especially CuO_x based catalysts have been reported to exhibit low O_2 to CO_2 selectivities due to oxidation of hydrogen. Co_3O_4 on the other hand has however shown better selectivity and H_2O resistance than CuO_x for CO-PROX in excess H_2 (see figure 2.4).

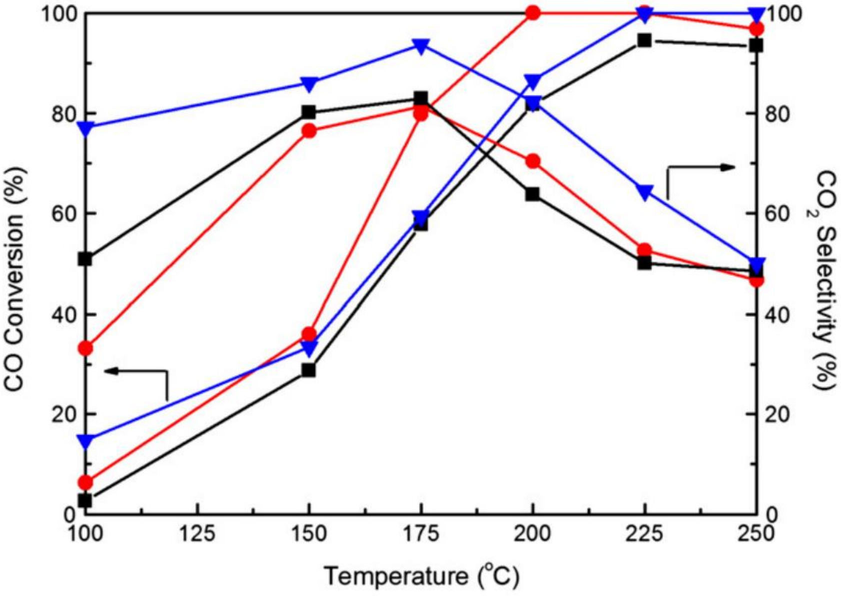

Figure 2.4: CO conversion and CO_2 selectivity on the three samples: (■) Co_3O_4/NP-CeO_2, (●) Co_3O_4/NP-$Ce_{0.8}Zr_{0.2O2}$ and (▼) Co_3O_4/NP-ZrO_2 for CO PROX reaction [57]

2.5 CO-PROX catalysts

Mishra et al. [19] compiled a report on a number of promising catalysts for CO-PROX. They are classified into three groups; precious metal catalysts (Pt, Pd, Ir, Ru or Rh) [58–60], nano-gold catalysts [61,62] and base metal oxide catalysts which are mostly transition metals (Co, Cr, Cu, Ni, Zn) [19,23,63].

2.5.1 Precious metal catalysts

Noble metal catalysts are highly active for CO oxidation and are one of the first catalysts to be recommended for CO-PROX reaction. Just like most catalysts, their catalytic properties strongly depend on the metal loading, dispersion and support type [23,64], but are inversely affected by a competitive Langmuir-Hinshelwood mechanism resulting from gases like CO, O_2 and H_2 adsorbed on the catalyst surface [51,60,65]. Among many noble metal catalysts studied, Pt and supported Pt catalysts have been found to be highly active in the CO-PROX in hydrogen rich stream [19,66].

Hulteberg et al. [66] conducted a CO-PROX study on Ir, Pd, Pt, Rh and Ru catalysts and discovered that the overall conversion of CO is dependent on catalyst's CO oxidation activity, reaction pathway (oxidation of CO or H_2, see equation 2-1), and lastly on the activity of reverse water-gas shift (RWGS) reaction. This competitive reaction is clearly demonstrated when a large temperature range is considered (see figure 2.5). Selectivity for CO combustion to CO_2 is high at lower temperatures but decreases with increasing temperature. This is because at higher temperatures, H_2 oxidation is favoured over CO oxidation, and the RWGS reaction sets in to maximise CO conversion [66].

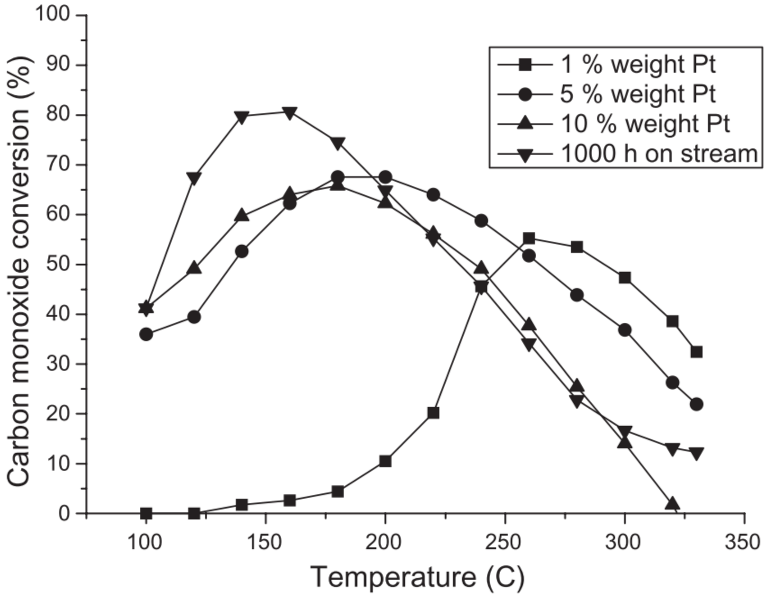

Figure 2.5: Variations of the activity with the Pt load on a cobalt-promoted sample over a temperature range of 100-325°C [66]

2.5.2 Gold metal catalysts

Gold alone is a poor catalyst for many reactions including CO-PROX due to its weak interaction with species adsorbing on the surface. A lot of research has shown that highly dispersed gold nanoparticles supported on partially reducible metal oxides (TiO_2, Fe_2O_3 and CeO_2) have good activity at low temperatures (also below 0°C) for CO oxidation. But gold catalysts lost attention due to being prone to deactivation more than precious metals [67], i.e. their selectivity for CO oxidation in H_2-rich streams is drastically affected by increase in temperature (formation of OH^- groups competes with CO oxidation) [69,70]. The catalytic performance of Au catalysts is characterised by high CO oxidation activity at low-temperatures, but poor selectivity for CO-PROX. When comparing gold and cobalt based catalysts anchored on the same support, cobalt based catalysts exhibited high selectivity for CO oxidation over a wide low temperature range. Guo and Liu [163] prepared Co_3O_4/CeO_2 modified with MnO_2 (see figures 2.6 A–C) and they were able to show that CO could completely be oxidised to CO_2 at a temperature of 80°C which is hardly observed over metal oxide catalysts [165, 166] and could easily be compared with noble metal catalysts [167, 168]. Similarly, Chang et al. [169] tested Au/CeO_2 modified with MnO_2 under CO-PROX conditions (See figures 2.6 D–F). The results from both studies might be influenced by reaction conditions and mechanisms, therefore the comparison is proposed in terms of activity and selectivity. Bion et al. [170] proposed that the decisive step for CO-PROX mechanism over Au/CeO_2 catalyst proceeds at the metal/support interface (Au-O interface), and the oxygen atom from the support oxidises CO to CO_2, probably via a Mars and van Krevelen type mechanism because of the participation of ceria oxide oxygen. The mechanism is however dependant on the oxygen mobility of the support [171, 172]. Over the Co_3O_4 catalyst, the reaction mechanism occurs via the Mars-van Krevelen mechanism as described in section 2.5.3.

The activity of almost all cobalt based catalysts reached 100% conversion and was drastically increased by addition of small amounts of MnO_x. Over the $Co_3O_4/CeMnO_2$, complete conversion of CO was achieved in a low temperature range of 80°C–180°C (see figure 2.6 A) and exhibited high selectivity, which was higher than that of gold catalysts. At the temperature of 80°C, the conversion of CO and corresponding selectivity were 100% and 98% respectively. Chang et al. [169] observed that 1% $Au/CeMnO_2$ showed very good activity for CO-PROX which decreased with increasing temperature, but poor selectivity caused by formation of water, which makes it hard to achieve CO removal to below 10 ppm. From both studies, gold based catalysts showed higher mass specific rate (higher by a factor of 10) and surface specific rate. The activity of both cobalt and gold based catalysts is comparable but attention has shifted to cobalt catalysts as its precursors are abundant and less expensive than gold catalysts.

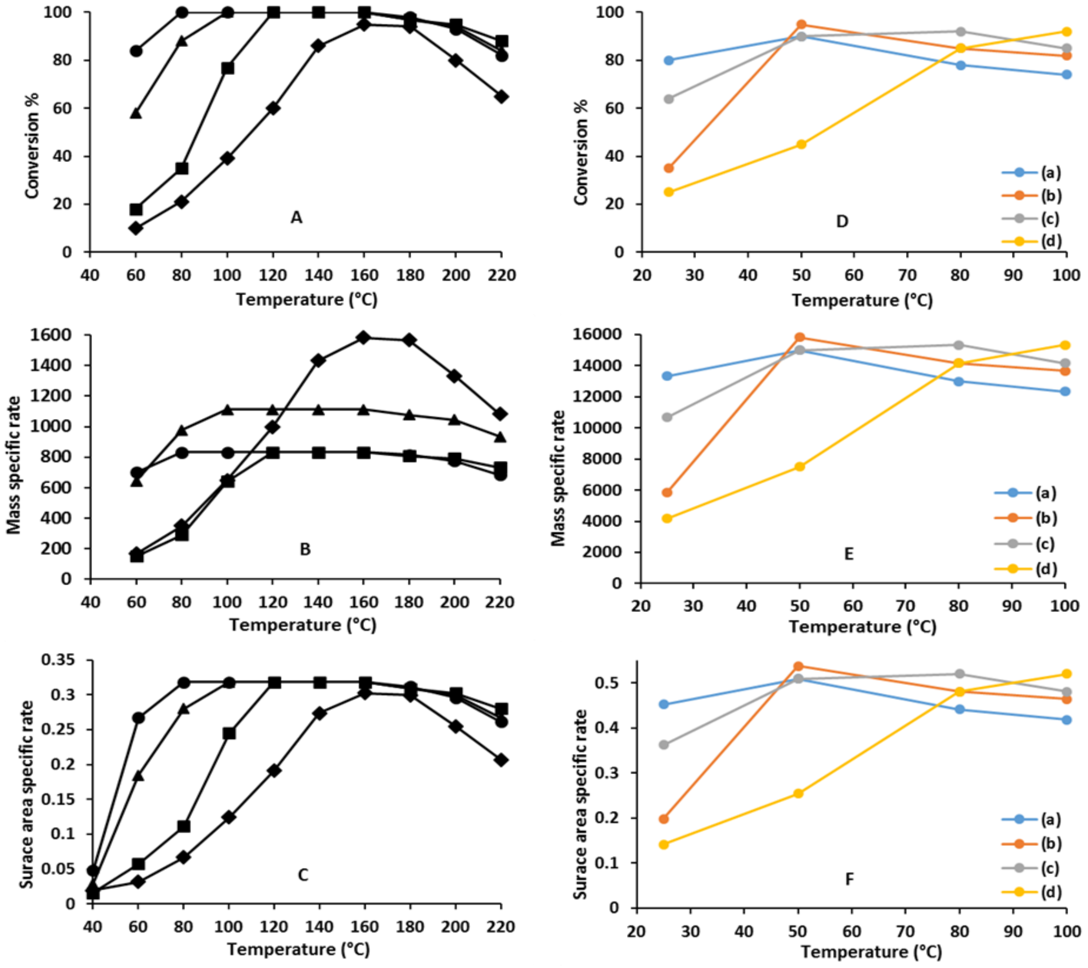

Figure 2.6: CO conversion (A), mass specific rate (B) and surface specific rate (C) over catalysts of (■) 80% Co_3O_4/CeO_2, (●) 80% $Co_3O_4/CeMnO_2$, (▲) 60% $Co_3O_4/CeMn_2O_2$ and (♦) 40% $Co_3O_4/CeMn_4O_2$ at GHSV of 40 000 $mlh^{-1}g^{-1}$. CO conversion (D), mass specific rate (F) and surface area specific rate (F) of various 1% Au/$MnCeO_2$ catalysts: (a) 1% Au/CeO_2, (b) 1% Au/$Mn_{0.1}Ce_{0.9}O_2$, (c) 1% Au/$Mn_{0.5}Ce_{0.5}O_2$, and (d) 1% Au/MnO_2 at GHSV of 30 000 $mlh^{-1}g^{-1}$ [163, 164].

2.5.3 Base metal catalysts

Due to the high cost and scarcity of precious metals and deactivating gold catalysts, a lot of research was conducted to find cheaper and easily accessible catalysts for CO-PROX [19,70]. Base/transition metal oxides catalysts have been found to be a good replacement for precious and gold based catalysts due to their good redox properties that support the Mars-van Krevelen mechanism [42,71,72]. In this mechanism, the catalyst is not merely a substrate but participates more actively in the reaction because the lattice oxygen from the metal oxide is part of the active species in the oxidation reaction. Considering figure 2.7, first the gaseous reactant (CO) diffuses to the cobalt oxide surface (see figure 2.7 (a)), where it is oxidised by lattice oxygen from the metal oxide forming carbon dioxide which subsequently diffuses into the gas phase (see figure 2.7 (b)). The last step is the re-oxidation of the resulting oxygen vacancy with the oxygen from the gas phase [73].

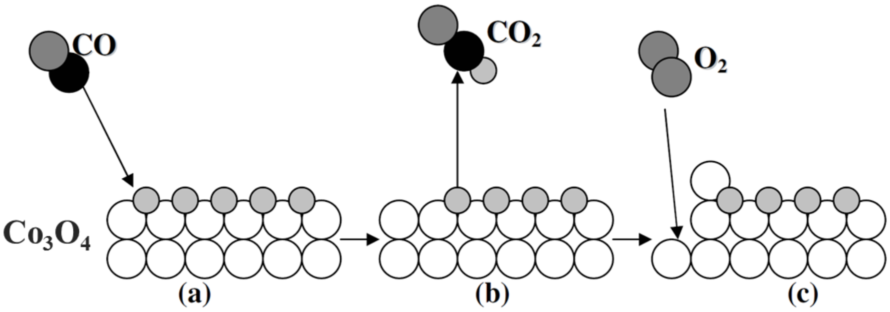

Figure 2.7: Schematic representation of the Mars-Van Krevelen mechanism [73]. The empty and grey spheres represent cobalt and oxygen atoms respectively, while the black spheres correspond to carbon atoms.

Researchers focused on preferential oxidation of CO in excess hydrogen are using mostly base metal oxides of Co [57,74], Cr [75], Cu [35,68], Ni [74,75] and Zn [74,75] supported on MgO, La_2O_3, SiO_2-Al_2O_3, CeO_2, $Ce_{0.63}Zr_{0.37}O_2$ and Co_3O_4. Their catalytic properties are strongly dependant on the synthesis method of the catalyst [76]. Of all these transition metal oxides investigated, only CuO supported on ceria or ceria-zirconia oxides catalysts were viewed a good replacement for the widely used precious metals. CuO catalyst's good activity and selectivity when supported on reducible support for CO-PROX at low temperatures (below 177°C) [77], is attributed to a synergistic effect explained by a preliminary mechanism in which surface lattice oxygen in CuO and oxygen vacancy of the support participate to start the reaction [19,78].

CuO has however been criticized to suffer from deactivation (decrease of the catalytic activity and the selectivity) in H_2O and CO_2 containing feed [39,68]. Deactivation through reduction of CuO to metallic Cu has also been reported. CuO reduces at elevated temperatures, at which increased water formation and no methane was observed. Agglomeration of CuO with time on stream was observed as another cause to deactivation [79,80].

Co_3O_4 has recently gained a lot of attention due to its good catalytic properties for CO oxidation. It is reported to have a normal spinel structure that contains two Co^{3+} and one Co^{2+} species that makes it a good catalyst for CO-PROX since it can achieve different oxidation states [81,82]. Studies show that most of the CO oxidation can be attributed to the Co^{3+} species as it strongly adsorbs CO [83]. Co_3O_4 catalysts supported on different metal oxides supports (ZrO_2, CeO_2, SiO_2, Al_2O_3, and TiO_2) were prepared and tested for the CO-PROX reaction. It was discovered that Co/ZrO_2 catalyst had the best results as it had the highest CO oxidation activity and O_2 selectivity to CO_2 over a wide temperature range (80-200°C, see figure 2.8) [84–86]. Like any catalyst, Co_3O_4 is also prone to deactivation (see section 2.6).

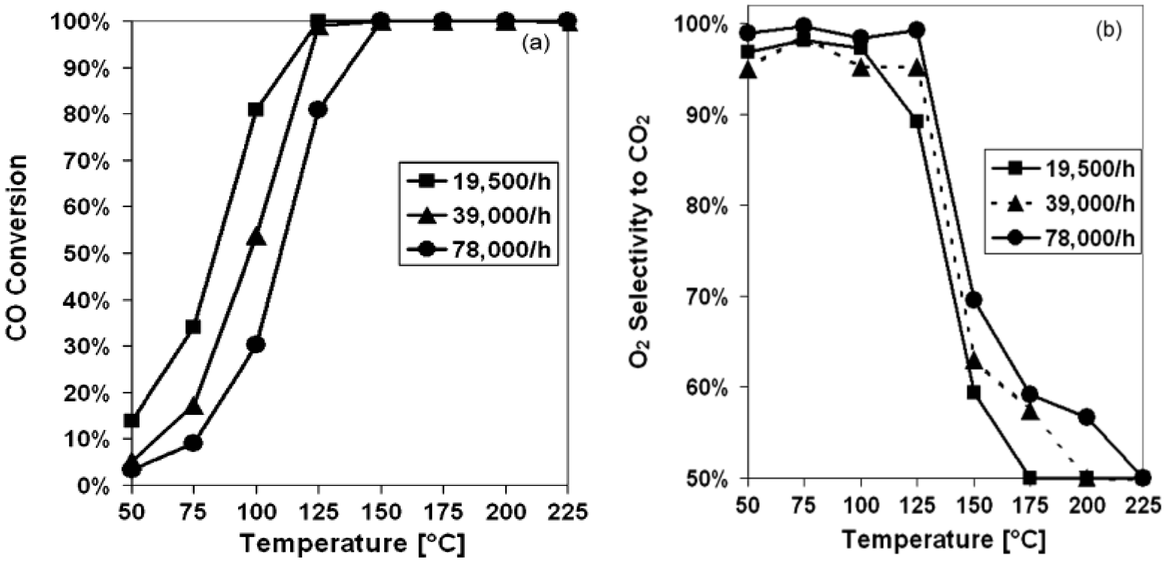

Figure 2.8: (a) CO conversion and (b) O_2 selectivity to CO_2 over $CoOx/ZrO_2$ at GHSV of (■) 19,500 h^{-1}, (▲) 39,000 h^{-1}, and (●) 78,000 h^{-1} in the presence of 5000 ppm CO, 5000 ppm O_2, 5% H_2, and balance Ar [86]

2.6 Catalyst deactivation

It is a common knowledge in the field of heterogeneous catalysis that catalysts are prone to deactivation. It is for this reason that the chosen catalyst for the CO-PROX reaction should have a practical lifetime and be cost effective in terms of lifespan activity [87]. Deactivation is an inevitable physical and/or chemical process that causes loss of catalytic activity and selectivity over time-on-stream [88]. It costs industry billions of dollars per year for catalyst replacement and shutdown of processes.

Though deactivation cannot be fully avoided for many processes, with an understanding of how it occurs, it may be postponed or reversed [89]. This understanding is important for the design of deactivating-resistant catalysts, and how industrial processes can be operated to reduce catalyst of activity [90]. Deactivation presents itself in a number of different mechanisms caused by certain reaction conditions. These include but are not limited to poisoning, phase transformation, coking or fouling and sintering. There are other forms of deactivation such as masking and loss of active elements through volatilization, erosion and attrition [90]. Deactivation can be classified into two broad classes; inherent catalyst deactivation and operational catalyst deactivation [87]. In CO-PROX, inherent deactivation occurs due to the catalyst being exposed to CO-PROX reaction conditions that consist of H_2, CO, CO_2, and H_2O, and operational deactivation can be caused by how the CO-PROX catalyst is loaded into the reactor and the type of synthesis or support used [87,89].

2.6.1 Poisoning

Poisoning can be described as a chemisorption of impurities either by competitive adsorption onto active sites, or by poison alloy formation with the active metal group sites hence impairing the performance of the catalyst [91]. The poison may affect the catalyst activity and selectivity by blocking the active sites or changing the adsorption of reactants or products which could lead to formation of new compounds [92].

During industrial CO-PROX reaction, the feed from the WGS usually contains 40-75% H_2,15-25% CO_2,10-20% H_2O, 0-25% N_2 and 0.5-1% CO. The presence of CO_2 and H_2O can have a negative impact on CO oxidation catalyst activity. In the presence of CO_2 and H_2O, the conversion of CO to CO_2 decreases when compared to CO conversion in only H_2 and CO [68,93]. CO_2 and H_2O are observed to compete with CO and O_2 for adsorption onto the catalytic surface.

The water vapour poisoning is not a problem if there is strong metal-support interaction [42]. Addition of water was also carried out during CO oxidation over 1.0 wt% Pt catalyst at 100°C. The result was an increase of CO conversion and was explained with the presence of water increasing CO conversion by the water gas shift reaction [33]. The second reason is the possible formation of formate groups which participate in the reaction, increasing CO oxidation [94]. Below 175°C, loss of catalytic activity also occurs due to accumulation of surface carbonates in the presence of CO_2 and H_2O [35]. There is a distinction between poisons and inhibitors. Poisons are those that adsorb strongly on the surface and react with it, while inhibitors weakly and reversibly adsorb on the surface. For example, oxygen containing compounds such as H_2O and CO_x which are usually present in CO oxidation reaction atmospheres merely adsorb on the surface limiting catalyst activity [92].

2.6.2 Metal oxide reduction

As mention earlier, Co_3O_4 is an excellent catalyst for low temperature carbon monoxide oxidation. The diagram in figure 2.9 shows that Co^{3+} is the active site for CO oxidation and donates oxygen in the oxidation of CO to CO_2 reducing to a Co^{2+} species. The Co^{2+} can be re-oxidized to Co^{3+} in the presence of oxygen, but over long periods in stream and with increased levels of CO_2, it becomes difficult to re-oxidize Co^{2+} to Co^{3+} due to competitive surface adsorption between CO_2 and O_2. The active Co^{3+} sites can only be regained by high temperature oxygen treatments [83].

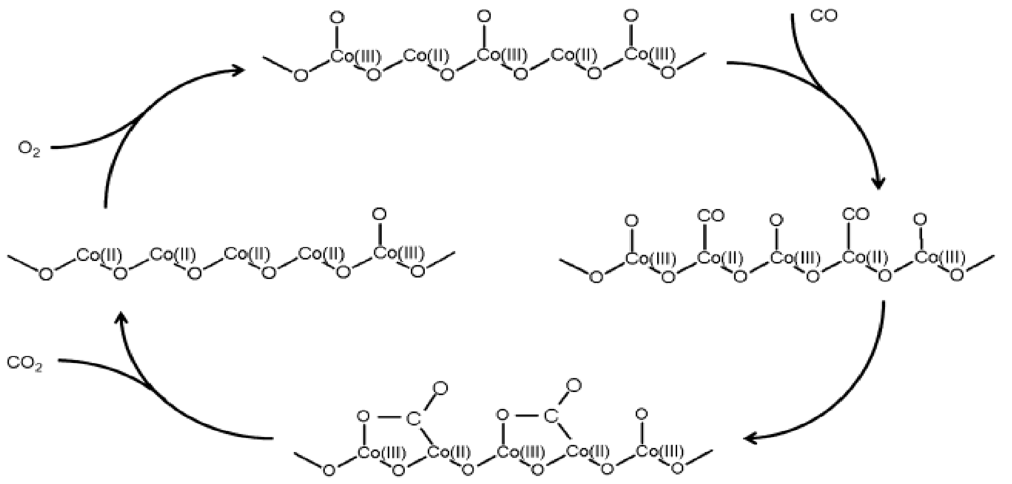

Figure 2.9: Proposed full catalytic cycle for CO oxidation to CO_2 on a cobalt oxide surface based on the calculations for the reaction of Co_3O_4 cluster with CO [95]

During preferential oxidation of CO, especially in the presence of hydrogen, Co_3O_4 is reported to be inclined to reduce to metallic cobalt which is inactive for CO oxidation. The presence of metallic cobalt in CO-PROX can lead to catalysis of other reactions like methanation and hydrogen combustion. Even though a lot of research has been done on the reducibility of Co_3O_4 catalysts in CO-PROX, some authors still believe that Co_3O_4 catalyst can be stable in hydrogen rich gas streams and still retain high activity if supported on an oxygen donating metal oxide [42].

2.6.3 Fouling, coking and carbon deposition

Fouling is a mechanical deactivation mechanism that refers to a surface covered with a deposit from a number of sources (combustion ash, soot, undesired by-products, coke or carbonaceous material, etc.) leading to deactivation as the result of active sites and/or pores blockage [89,96].

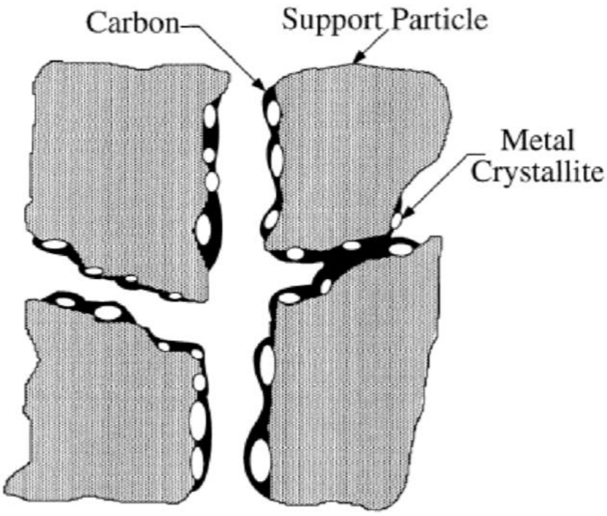

Figure 2.10: Conceptual model of fouling, crystallite encapsulation and pore plugging of a supported metal catalyst due to carbon deposition [89]

In some cases of fouling, the environment causes deposition, so the catalyst does not play the major role. However, in most cases, the catalyst is the cause of fouling especially if side reactions take place. For example, in catalytic reactions of hydrocarbons, by-product formation leads to deposits that physically cover the pores and active sites of the catalyst as illustrated in figure 2.10 above. In the context of the CO-PROX reaction, it was concluded that cobalt oxide can deactivate by CO_2 adsorption or formation of carbonate species [42,84].

2.6.4 Sintering

Thermal degradation is a significant cause of catalyst deactivation due to physical change of the catalyst surface by crystallite growth and agglomeration of small unsupported metal crystallites into larger crystallites. The process is more likely at high temperatures and is catalysed by the presence of water vapour. Sintering causes a decrease of surface metal atoms per unit mass and is therefore decreasing the number of active sites [97].

Figure 2.11 shows atomic migration (A) and (B) crystallite migration mechanisms through which sintering of supported metal catalyst can occur. In atomic migration, sintering involves metal atoms escaping from the crystallite, moving across the surface of the support or in the gas phase followed by subsequent merger of these atoms with other metal crystallites on collision. In the second model, crystallite migration, sintering occurs as a result of migration of the crystallite across the surface of the support resulting in their collision and coalescence [92].

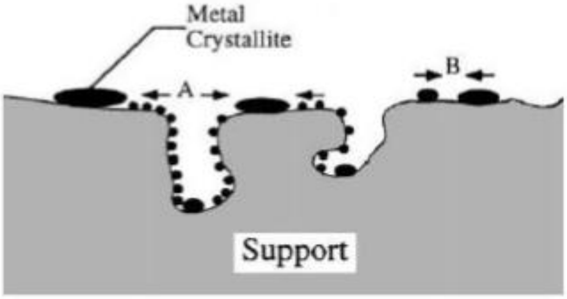

Figure 2.11: Conceptual models for crystallite growth due to sintering by (A) atomic migration or (B) crystallite migration [89]

Sintering processes are temperature dependant and the melting point plays a crucial role in sintering. The temperature at which surface species migrate is called the Huttig temperature and the temperature at which the bulk species migrate is the Tamman temperature. These temperatures may be expressed according to the semi-empirical equations equation 2-7 and equation 2-8.

$$T_{Huttig} = 0.3 \cdot T_{melting} \qquad \text{Equation 2-7}$$

$$T_{Tamman} = 0.5 \cdot T_{melting} \qquad \text{Equation 2-8}$$

When the Huttig temperature is reached, atoms at defects become mobile, while upon reaching the Tamman temperature atoms from the bulk will exhibit mobility. At the melting temperature, the mobility increases drastically and liquid-phase behaviour is observed. The temperature at which the solid phase becomes mobile depends on texture, size, and morphology [96].

Table 2.1: $T_{melting}$, T_{Tamman} and $T_{Hüttig}$ values (K) of Co_3O_4, CoO, Co and SiO_2 [96,98]

Compound	$T_{melting}$ (k)	$T_{Hüttig}$ (k)	T_{Tamman} (k)
Co_3O_4	1223	369	612
CoO	2073	622	1037
Co	1733	526	877
SiO_2	1986	596	993

It is clear from table 2.1 that the Co_3O_4 crystallites are likely to sinter since the T_{Huttig} of Co_3O_4 falls within the optimal CO-PROX conditions of 80-175°C (353-448K). The use of support is beneficial to counter sintering of Co_3O_4 crystallites. It hinders agglomeration of crystallites as it gives physical separation [97]. The silica support is a good choice for CO PROX as it possesses high Tamman temperature (see table 2.1) and is frequently classified as a thermostable support. Moreover, the small metal crystallites are often anchored to silica support by chemical bonds which creates strong metal support interaction, consequently inhibiting sintering [96].

2.7 Other CO removal methods

Proton exchange membrane fuel cell applications have gained much research attention due to several advantages that fuel cells offer over other power generation processes. The potential for high efficiency and environmentally benign nature of their exhaust makes them very attractive [18,99]. Hydrogen is an ideal fuel for PEM fuel cells; it can be produced from fossil fuels via three main chemical processes like steam reforming, partial oxidation and autothermal reforming. The hydrogen stream produced from fossil fuels contains significant amounts of CO (0.5 -1%) even after the high and low temperature water-gas shift reactions. CO poisons the anode side of the fuel cell by preferentially adsorbing to the catalyst (platinum) surface and blocking the active sites. To mitigate this effect of CO poisoning, the hydrogen stream must further be purified by lowering CO levels to 10-100 ppm [100].

Apart from CO-PROX, purification of hydrogen can be achieved by several other methods such as hydrogen membrane purification, pressure swing adsorption, CO methanation.

2.7.1 Hydrogen selective membrane purification

The hydrogen membrane purification technique is one of the alternatives for purifying hydrogen. It comes with the advantages of easy membrane preparation, low energy consumption and are cost effective at low gas volumes. The membranes are classified on the basis of their nature, separation regime and geometry. There are three categories of membranes; polymeric, inorganic and metallic membranes. Polymer membranes are economical as they are cheap and do not require large pressure drops to separate the gases. They, however, have a disadvantage of a weak mechanical structure [101,102]. Inorganic membranes have the advantage of stability at high temperatures of 200-800°C. In some applications, inorganic membranes can still be operational even at temperatures above 1000°C [103]. A third class of membranes, metallic membranes, can be classified into supported and unsupported. They have good hydrogen permeability but are affected by permanent adsorption of hydrogen on the surface causing brittleness. The adsorption of hydrogen on metallic membranes can be minimized by using alloys but this results in increased operational costs [19].

2.7.2 Pressure swing adsorption

Pressure swing adsorption (PSA) technology is widely used because of simplicity and low operating costs associated with it. As the name suggests, it uses pressure to separate gas species from a mixture of gases using their molecular characteristics and affinity to the adsorbent material. The adsorbent materials such as activated carbon, alumina and silica gel are used frequently and each adsorbent preferentially adsorb a certain group of molecules from the mixture [104]. The process has four basic steps; adsorption, depressurization, regeneration and repressurization [105].

The use of this technology has been adopted by many countries including USA, France and China, most significantly in the processes of steam-methane reforming after the water-gas shift. Many commercially available adsorbents are prone to chemical instability against contaminants and attrition. They are also not economically viable as the synthesis costs are high [106].

2.7.3 CO Methanation

The methanation reaction is the most basic reaction for hydrogenation of CO and is highly used in a number of applications, including the removal of CO from H_2 rich streams. The reactions (equation 5 and 6) represents a chemical transformation that occurs in a gas that comes from the water-gas shift process over a hydrogenation catalyst which in most cases is metallic nickel [107].

The selective CO methanation (equation 5) has its own advantages. It does not require the introduction of any gases such as air as it is required in CO-PROX reaction, and can reduce CO concentration from 0.5% to 20 ppm [108]. Although CO methanation is applied in many industries, hydrogen is consumed in large amounts during hydrogenation of CO and CO_2, so the application of this method is less popular [70].

2.8 Catalyst synthesis methods

The design and fabrication of nanomaterials is an important subject in both material sciences and heterogeneous catalysis because their properties differ from those of bulk crystals [81]. Conventionally the main idea is to synthesise particles as small as possible to increase activity, but developments in morphological and structural nanomaterials allowed the synthesis of catalysts exposing more reactive planes [109]. In order to study the effects of morphology on the activity and selectivity by the characteristic planes they expose, it is important to prepare model catalysts in the nanometre scale with well-defined planes and narrow size distribution.

Interest in nanocrystals morphology has been increasing explosively due to their good chemical and physical properties. To fully utilize this properties and investigate the effect of crystallite morphology, it is necessary to find a synthetic route to obtain a well-defined nanocrystals with controlled morphology, dimensionality and surface chemistry [110].

A number of different techniques which are solution based have been proposed. Hydrothermal and solvothermal routes, and liquid phase precipitation are the most preferred techniques since they offer low temperature, easy control and large scale fabrication with controlled morphology [109]. Supercritical hydrothermal and liquid precipitation synthesis methods are used to fabricate model catalysts in this study.

2.8.1 CO Supercritical hydrothermal synthesis

There are a number of ways through which nanoparticles with specific morphology can be synthesised, but this report focusses only on hydrothermal and precipitation techniques which were used in this research. Supercritical hydrothermal synthesis has a number of definitions, but it is generally regarded as a heterogeneous chemical reaction involving aqueous solvents under high pressure and temperature. The main aim is to dissolve and recrystallize materials that are relatively insoluble at room temperature and pressure. This is possible with solvents at supercritical temperatures because their properties such as density and solubility can be changed with temperature and pressure, both of which have an effect on supersaturation and nucleation [111].

The properties of water; ionic product, density, thermal conductivity, viscosity, heat capacity and dielectric constant are temperature and pressure dependant [112]. Therefore, by manipulating the synthesis variables (temperature and pressure), certain properties of the solvent can be used to get certain results. Figure 2.12 demonstrates the dielectric constant of water versus temperature at pressures from 1 bar to 500 bar [113]. The dielectric constant drops sharply with temperature at all pressures. This drop is associated with solubility and ionic species that are used for inorganic materials synthesis. The decrease of dielectric constant pushes the nucleation of particles which is followed by precipitation [112].

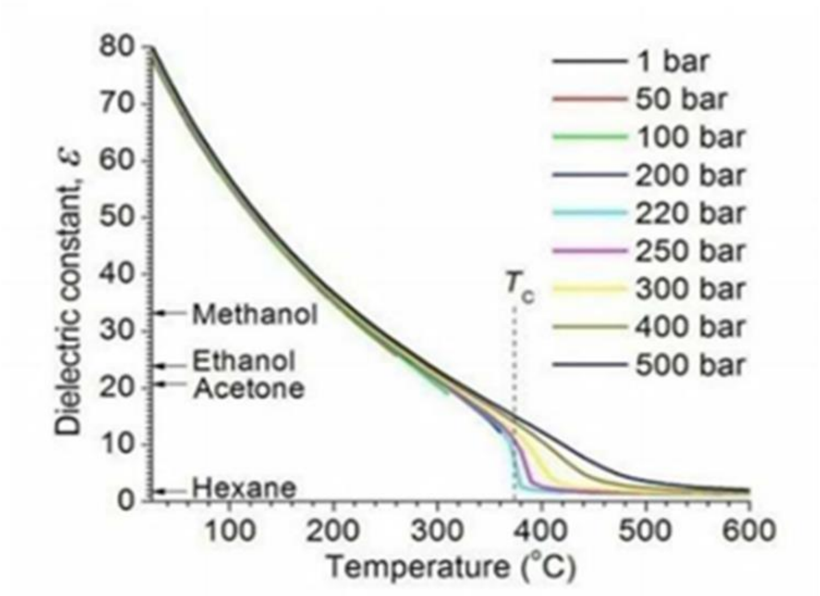

Figure 2.12: Dielectric constant of water at various temperatures and pressures. The dielectric constants for solvents at ambient conditions are indicated with arrows [113]

In many case studies, simple salts like metal chlorides, nitrates and acetates are used in the synthesis of inorganic compounds. Metal hydroxides of these salts can be obtained by addition of neutral solvents like water or ethanol and other additives for pH control and reduction or oxidation prior to hydrothermal treatment [112]. In the early 1990's, Adschiri et al. [114] suggested the following simple 2-step mechanism for the formation of particles from simple metal salt precursor.

Step 1: Hydrolysis $MX_{x(aq)} + xH2O_{(l)} \rightarrow M(OH)_{x(s)} + xHX_{(aq)}$

Step 2: Dehydration $M(OH)_{x(s)} \rightarrow MO_{x/2(s)}) + x/2H2O_{(l)}$

Where M is the metal and X the anion. The metal oxide is formed as the equilibria shifts to the right in step 1 due to an increased temperature. Many aspects of the reactions are unknown because of the quick formation of intermediates and their amorphousness [112].

If for example an aqueous solution contains the metal salt precursor and is quickly heated to temperatures above the critical point, immediately the low dielectric constant will force the nanoparticles to precipitate. Very small particles with narrow size distribution can be obtained because all the ions present in the aqueous solution will simultaneously precipitate in many particle nuclei [112,115]. Figure 2.13 illustrates a synthesis at a subcritical and supercritical conditions. In the subcritical conditions, precipitation occurs slowly because nucleation does not happen instantaneously. It is explained that the ratio of the metal ions in the precursor that do not precipitate instantaneously will slowly crystallize around the particle nuclei and thus result in a particle growth, yielding large particles with a wide size distribution [115].

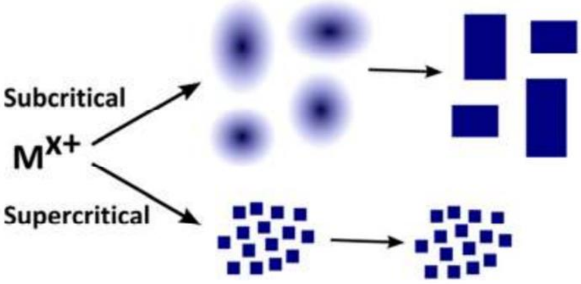

Figure 2.13: Growth of MO_x under sub- and supercritical conditions [115]

A typical hydrothermal synthesis is carried out in a batch reactor which is usually an autoclave that can withstand high temperatures and pressures. The precursor and other additives are dissolved or suspended in water and sealed in the autoclave as shown by a lab-scale version in figure 2.14 A. Depending on the synthesis, the contents of the autoclave are heated rapidly or at a certain ramping rate to a desired temperature, and the pressure is usually auto generated. It is noted that pressures of up to several hundreds of bars can be achieved depending on the degree of autoclave filling [113]. Figure 2.14 B shows pressure as a function of temperature for a degree of filling.

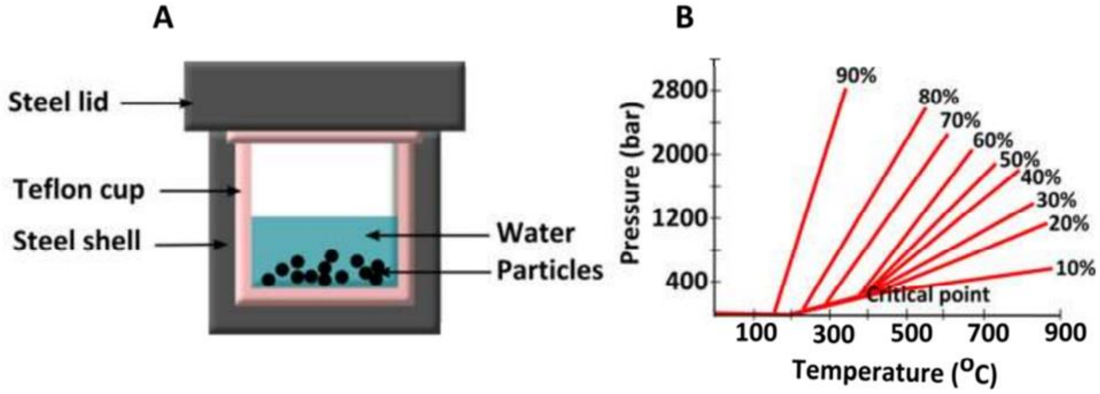

Figure 2.14: (A) Schematic drawing of a lab-scale autoclave. (B) Pressure obtained in autoclaves at different filling fractions [113]

Hydrothermal synthesis has a number of applications ranging from emeralds to preparation of nanoparticles [116]. Researchers have also used this synthesis process for materials like quartz [117]. Despite huge developments and confidence in the batch reactors to perform hydrothermal synthesis, efforts have been made in developing continuous reactors. The first developed hydrothermal flow reactors are reported to be suitable for supercritical synthesis where rapid heating rates are necessary [114].

2.8.2 Hydrothermal oxidative precipitation

Researchers have recently developed a synthetic method to develop Co_3O_4 nanoparticles via low temperature (90-120°C) chemical route, namely hydrothermal oxidative precipitation. This method can potentially offer low cost, high purity and large scale production [118]. There are also a number of methods that include hydrolysis, sol-gel and microemulsion (or reverse micelles). Compared with these methods, hydrothermal oxidative precipitation is carried out at relatively low reaction temperatures to produce morphology orientated nanoparticles, and often without the necessity of post-calcination [119]. Hydrothermal synthesis can also be done at atmospheric pressure with purified dry air bubbled through the solution for the duration of the synthesis. Different structures and morphologies can be obtained by altering reaction conditions like reaction temperatures, pH values, reactant concentrations and molar ratios, additives, and so forth [120].

2.9 Morphology and activity for PROX reaction

The effect of morphology on preferential oxidation of CO is a very significant factor to consider. From the viewpoint of traditional heterogeneous catalysis, the performance of the catalyst strongly depends on the morphology and size of the nanoparticles. The general rule of thumb is that the reactivity of the surface depends on how open the surface is, that is, how readily available the reactive species are to participate in a chemical reaction, and on their concentration. The surface reactivity depends on the density of surface atoms and the number of dangling bonds [121]. Moreover, high activity and selectivity in CO-PROX results from the number of active Co^{3+} sites and number of open spaces for the adsorption of CO molecules [1,121,122].

In order to study and understand the effect of crystallite morphology on activity, the work of Hu et al. [121] was considered. They investigated the effect of Co_3O_4 nanoparticle morphology and resulting preferential crystal plane in the methane combustion. It is important to note that like the CO-PROX reaction, methane combustion follows a Mars-Van Krevelen mechanism (see section 2.5.3) [71]. As illustrated in figure 2.15 (a), it was discovered that catalysts in the nano-size range with different morphology and uniform crystal planes exhibit different catalytic properties. Co_3O_4 nanosheets clearly show higher activity than all other configurations at any given temperature, followed by Co_3O_4 nanobelts and nanocubes. The temperature at which the conversion of methane is 50% (T_{50}) is 312°C for Co_3O_4 nanosheets, 320°C for nanobelts and 346°C nanocubes.

Figure 2.15 (b) shows the CH_4-TPR profiles to illustrate the redox properties of the Co_3O_4 nanosheets over nanobelts and nanocubes. Co_3O_4 nanosheets show a broader peak centred at 425°C while Co_3O_4 nanobelts and nanocubes have peaks centred at slightly higher temperatures of 433 and 448°C respectively. A second peak is observed at 610°C for nanosheets, 737°C nanobelts and beyond 900°C for nanocubes. Hu et al. [121] associate the first peak in all the samples to the reduction process of Co^{3+} to Co^{2+} while the reduction of Co^{2+} to Co^0 is associated to the second peak. The characteristic broadness of the first peak of nanosheets shows larger consumption of CH_4 than is seen for nanobelts and nanocubes.

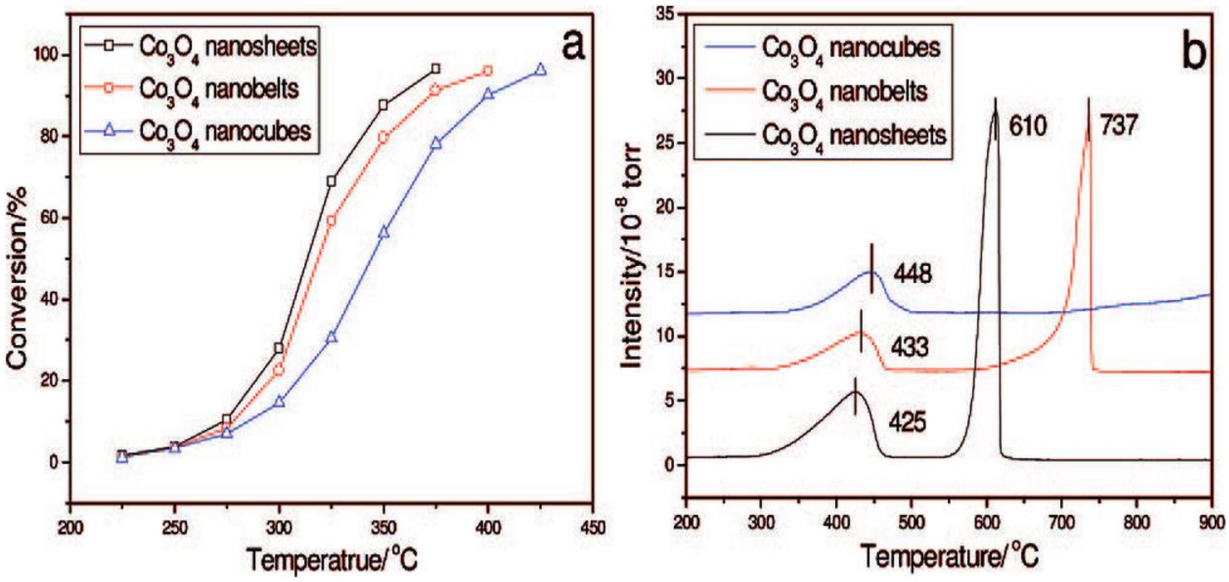

Figure 2.15: (a) Methane conversion as a function of temperature over Co_3O_4 nanosheets, nanobelts, and nanocubes at GHSV = 40 000 h^{-1}; (b) CH_4-TPR profiles of Co_3O_4 nanosheets, nanobelts, and nanocubes [121]

The stability of the three different Co_3O_4 nanocrystal morphologies after exposure to temperatures as high as 400°C during CH_4 combustion [121] was also investigated. Table *2.2* below shows the individual BET surface areas (S_{BET}) of the three Co_3O_4 nanocrystals for a fresh catalyst and two consecutive runs. The S_{BET} results for the first and second run show a very small change when compared to the fresh catalyst S_{BET} results. This shows the stability of the three different morphologies of Co_3O_4 nanocrystals at temperatures high as 400°C during methane combustion. In addition, figure 2.15 further illustrates the stability of the three morphologies over a period of 300 hrs test, with methane conversion reported to be between 90 and 98% [121].

Table 2.2: BET surface area and catalytic activity of different Co_3O_4 catalysts for CH_4 combustion [121]

	Co_3O_4 Catalyst	$T_{BET}(m^2C^{-1})$
Fresh	Nanosheets	17.8
	Nanobelts	20.1
	Nanocubes	22.6
1st run	Nanosheets	17.6
	Nanobelts	20.1
	Nanocubes	22.4
2nd run	Nanosheets	17.4
	Nanobelts	20.0
	Nanocubes	22.2

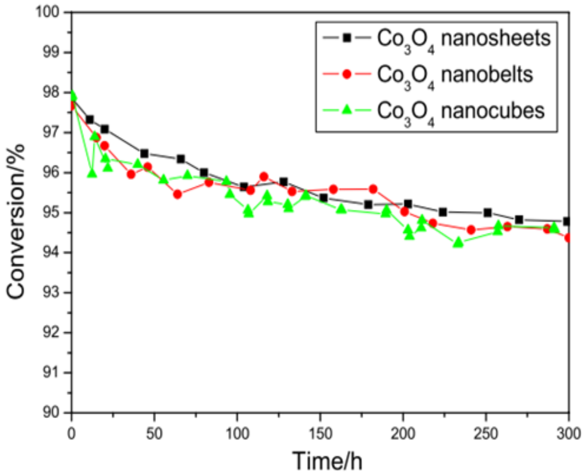

Figure 2.16: Time dependence of methane conversion over Co_3O_4 nanosheets at 375°C, Co_3O_4 nanobelts at 400°C and Co_3O_4 nanocubes at 425°C [121]

The good catalytic properties exhibited by Co_3O_4 nanosheets above other configurations is the result of exposed planes which are rich in catalytically active Co^{3+} species [121]. The analysis of the structure shows that Co_3O_4 nanosheets, nanobelts and nanocubes predominantly expose {112}, {011} and {001} planes respectively. Figure 2.17 shows the slab models used to illustrate the fact that {112} plane is the most open plane of an fcc crystal compared to the {011} and {001} plane.

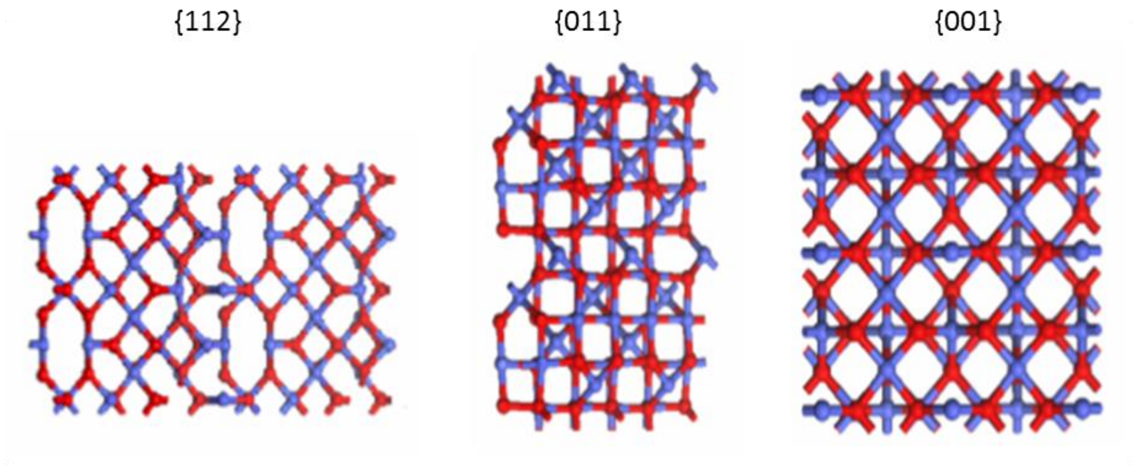

Figure 2.17: Slab model of {112} (nanosheets), {011} (nanobelts) and {001} (nanocubes) surface of fcc Co_3O_4 nanocrystal (the red and blue spheres are oxygen atoms and cobalt atoms, respectively) [121]

2.10 Magnetometer

A magnetometer is a material characterisation tool which can be used to study the behaviour of ferromagnetic materials. Magnetic measurements can be performed on a sample to obtain information about the catalyst particle size and composition. All materials can be classified as ferromagnetic, superparamagnetic, antiferromagnetic or paramagnetic in terms of their behaviour which depends on their bulk magnetic susceptibility [124].

Ferromagnetism is the characteristic of substances describing the ability to align their permanent atomic magnetic moments parallel to one another when exposed to an external magnetic field (H) [125]. In ferromagnetic materials, all the magnetic moments in the microscopic regions (domains) align during magnetisation, but have random orientation when unmagnetised, showing a zero net magnetic moment [125].

Ferromagnetic materials exhibit a phenomenon referred to as remnant magnetisation (M_r) which is a result of the strong coupling between neighbouring moments/spins. Remnant magnetisation occurs when a material is placed in an external magnetic field causing magnetic moments to align, and the external field is removed, the magnetic moments or a fraction of them stays aligned. This means that the material stays magnetised even though the magnetic field is removed.

Because of the temperature-dependency of ferromagnetism, there is a critical temperature, termed the Curie temperature (T_C), above which the ferromagnetic material loses its magnetization and becomes paramagnetic. Above the T_C, the high thermal energy causes strong interaction or randomisation of the magnetic moments, which means the material loses magnetism.

Superparamagnetism is a term used for a type of ferromagnetism in which crystallites in the nanometre scale are below or at the certain size of magnetic domain and lose magnetism upon removal of the external field. Due to the size dependency, larger crystallites will show magnetism at low field strengths. At high field strengths, saturation magnetisation (Ms), both the larger magnetic domains and the small magnetic domains will align in the direction of the external field, but the magnetisation will only be a result of the smallest crystallites. Figure 2.18 shows superparamagnetic behaviour at both low and high field strengths.

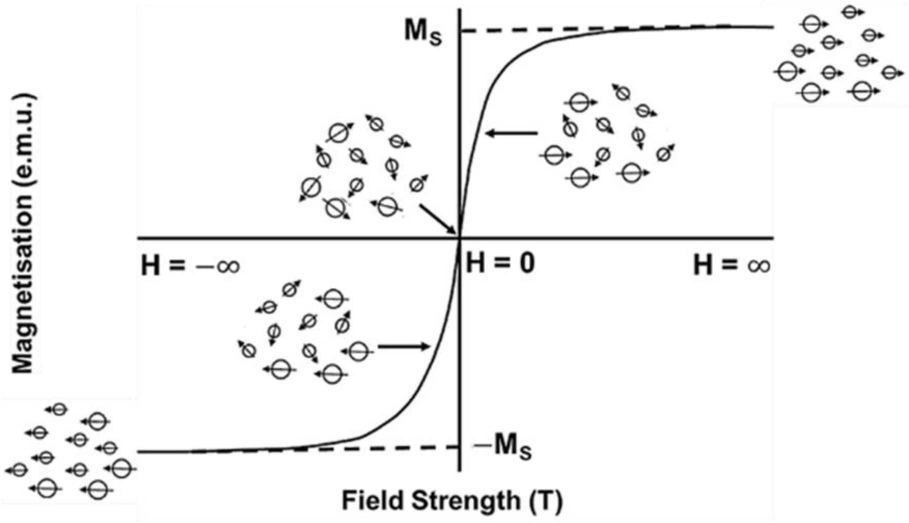

Figure 2.18: Schematic representation of the magnetisation of superparamagnetic particles in an external magnetic field [126]

At high strengths of magnetic field where all the magnetic domains in the crystallites align parallel to each other, the crystallites are said to have reached saturation magnetisation (M_s). This characteristic can be used to get information about the average crystallite size and size distribution. According to the Langevin function, equation 2-9, crystallite size is a function of temperature. Metal magnetisation can be determined as follows;

$$\frac{M}{M_s} = \coth\left(\frac{\rho \cdot \sigma_S \cdot \frac{\pi}{6} \cdot d^3 \cdot H}{k_B \cdot T}\right) - \left(\frac{k_B \cdot T}{\rho \cdot \sigma_S \cdot \frac{\pi}{6} \cdot d^3 \cdot H}\right) \qquad \text{Equation 2-9}$$

Where **M/Ms** the ratio of sample magnetisation to saturation magnetisation, ρ is the density of the magnetic material, σs the mass specific magnetisation, d the crystallite diameter, H the external applied field, T the temperature and k Boltzmann constant. The mass specific magnetisation at saturation is reported to be 168 emu.g^{-1} at room temperature, and the critical diameter of cobalt, below which crystallites will exhibit superparamagnetic behaviour is reported to be 20 nm [127,128]. Figure 2.19 shows a hysteresis plot obtained when the magnetisation of a partially ferromagnetic sample is measured as function of the applied magnetic field. When the external magnetic field is removed, the plot can be used to determine the relative amount of the sample with remnant magnetisation.

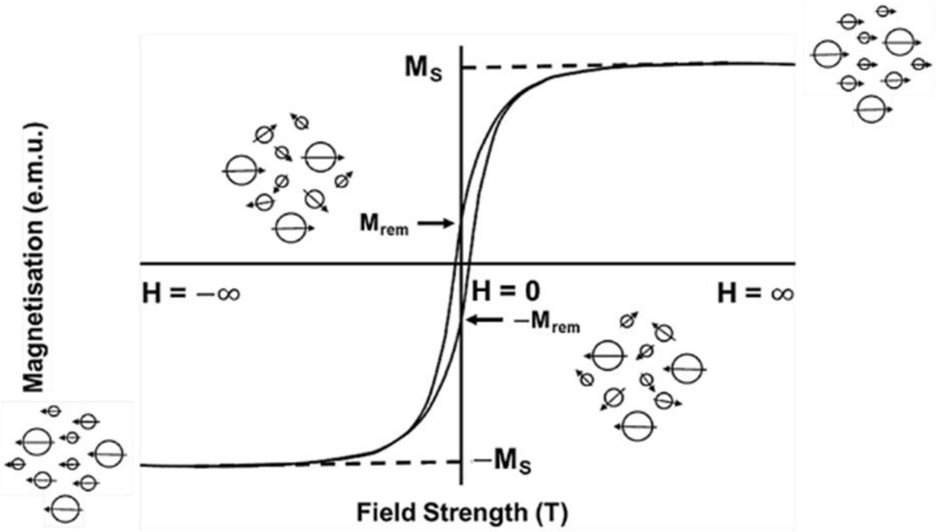

Figure 2.19: Hysteresis plot of a ferromagnetic sample [126]

This amount represents the fraction of ferromagnetic material and can therefore be used to get qualitative information about changes in the crystallite size. The percentage change of ferromagnetic material is given by equation 2-10.

$$\boldsymbol{\gamma}\,(\boldsymbol{wt}.-\%) = \frac{\boldsymbol{2M_{rem}}}{\boldsymbol{M_s}} \times \mathbf{100} \qquad \text{Equation 2-10}$$

Where γ is the percentage of ferromagnetic material, M_r the remnant magnetisation and M_s the saturation magnetisation.

In antiferromagnetic materials, the magnetic moments align themselves in opposite directions in the presence of an applied field [125]. Antiferromagnetic also changes its behaviour above the critical temperature called the Néel temperature and show signs of paramagnetism.

Paramagnetic materials are almost non-magnetic as they exhibit weak magnetism. Even though their magnetic moments align in the presence of the external field, they are immediately weakened by thermal motion that leads to randomisation of magnetic spins [125].

3 Scope of study

The preferential oxidation of CO is one of the techniques used to purify hydrogen rich stream produced on-board by steam reforming so that CO, which is poisonous to the fuel cell can be reduced to acceptable levels. More importantly, Co_3O_4 has been observed to be a good alternative catalyst for CO-PROX, and tuning the morphology can enhance its activity. The catalysts for the reaction are normally precious metals and transition metals, which are available as conventional nanoparticles that can be modelled as spherical. Nanoparticles with controlled morphology and size supported on oxygen sufficient support are believed to be a good start in developing a model catalyst with good selectivity, activity and stability to selectively oxidize CO without H_2 consumption.

The CO-PROX reaction is highly exothermic which implies that the bulk cobalt oxide (Co_3O_4) catalyst may be exposed to a range of temperatures during catalyst testing and this could lead to reduction of Co_3O_4 to metallic cobalt. Studies on the reduction of morphology-dependent Co_3O_4 have been done in CH_4 combustion and CO oxidation. However, these studies are limited as only fresh and already reduced spent catalysts could be characterised. There was no online continuous monitoring of the catalyst over the CO-PROX temperature range to get an insight on how and at what temperature does reduction occur. In addition to studying effects of morphology, it would be beneficial to carry out *in situ* characterisations in order to gain information on the changes of the catalyst structure and phase changes in real time.

The main objective of this study is to investigate the effects of different Co_3O_4 crystallite morphology (nanosheets, nanobelts, nanocubes) on thermally induced reduction under CO PROX conditions. The studies will be conducted in a state of the art equipment, *in situ* magnetometer and PXRD capillary cell, developed by the University of Cape Town, with Co_3O_4 crystallites supported on SiO_2. It is expected that the morphologically tailored Co_3O_4 crystallites will have prolonged high activity and selectivity, and will reduce to metallic Co at higher temperatures when compared to usual spherical Co_3O_4 nanoparticles, with nanosheets showing better performance.

To carry out these studies, the catalyst and support will be synthesised via hydrothermal method and SiO_2 spheres with a seeded growth technique. Three morphologies (sheets, belts, cubes) of Co_3O_4 crystallites and spherical SiO_2 support will be prepared. Different morphologies expose planes with different densities of active Co^{3+} site hence increasing the redox properties of the catalyst. It is therefore hypothesised that synthesis of different morphologies exposing different planes will result an open catalyst surface with a high concentration of Co^{3+} active sites, therefore increasing its activity.

4 Experimental methodology

Various techniques were used to synthesize unsupported Co_3O_4 nanoparticles of different morphology [2,3,96,99-111]. As support, SiO_2 spheres were prepared by a seeded growth technique termed Stöber process [129]. The unsupported and supported materials were characterised with transmission electron microscopy (TEM), scanning electron microscopy (SEM), X-ray photoelectron spectroscopy (XPS), Brunauer–Emmett–Teller (BET) surface area measurement and powder X-ray diffraction (PXRD). In addition, the model catalysts (SiO_2 supported Co_3O_4) were characterised using an *in situ* magnetometer and *in situ* PXRD.

The following sections describe in detail the techniques used for the synthesis of Co_3O_4 nanoparticles (nanocubes, nanosheets, nanobelts) and the SiO_2 support as well as the characterisation techniques supporting the synthesis followed by the catalytic testing procedure for the *in situ* experiments.

4.1 Synthesis of unsupported nanocubes

Two different techniques reported in literature [121,130] were applied to yield Co_3O_4 nanoparticles with a cubic morphology.

4.1.1 Supercritical hydrothermal synthesis– amine cubes

The method described by Hu et al. [121] is to prepare one batch of cubic Co_3O_4 nanoparticles. 0.291 g of $Co(NO_3)_2{\cdot}6H_2O$ (Sigma Aldrich 98% purity) is dissolved in 20 ml of ethanol (Kimix) yielding a 0.001 M red solution. Subsequently a mixture of 2 ml of octadecenylamine (ACROS Organics 90% purity) and 10 mL of ethanol (Kimix) are added dropwise and the mixture is left stirring for 30 min during which a colour change from red to green is observed as β-$Co(OH)_2$ forms. The solution is subsequently transferred into eight 40 ml parr acid digestion autoclaves (Parr instrument company) equipped with a Teflon liner, sealed and fixed in a rack. The rack is mounted on a rotating shaft in an oven (RKC instrument Inc.) and heated to 180°C for 12 hours. After cooling, a black paste is obtained which is sequentially washed five times with ethanol and water. The sample is dried under vacuum (100 mbar) at 60°C overnight using a rotary evaporator R-210/215 (BUCHI Switzerland) and calcined in a Nabertherm furnace at 350°C for 3 hrs to give Co_3O_4 nanocubes. The prepared cubes are labelled amine nanocubes in the present study.

4.1.2 Hydrothermal oxidative precipitation synthesis– HCl cubes

An alternative synthesis route was reported by Lee et al. [131]. Here, 60 g of $NaNO_3$ (Sigma Aldrich, 1-2 mm beads, 98% purity) are mixed with 30 ml of 1 M NaOH solution and 70 ml of deionised water. The prepared mixture is transferred into a three-necked round bottom flask equipped with a condenser, heated by an oil bath and agitated by a magnetic stirrer. A stream of purified air (50 ml/min, NTP) is continuously bubbled through the mixture. Upon heating the flask to 120°C, the $NaNO_3$ beads are dissolved.

20 ml of 1 M solution of $Co(NO_3)_2 \cdot 6H_2O$ (Sigma Aldrich 98% purity) is added dropwise at 120°C. Upon contact with the sodium nitrate/hydroxide bearing solution, a blue precipitate is instantly formed. The solution is left stirring at the temperature (120°C) for 22 hours, gradually turning to black colour signalling the formation of Co_3O_4 and the completion of the synthesis. All unreacted compounds are dissolved without stirring over the course of 48 hours through addition of 100 ml of 1 M HCl.

The slurry is centrifuged five times at 5000 rpm for 10 min to remove excess aqueous HCl and wash with deionised water, dried overnight in a Memmert oven at 120°C and calcined using the Nabertherm furnace at 200°C for 2 hours in an attempt to remove residual chlorine. These samples are referred to as HCl nanocubes in the present report.

4.2 Synthesis of unsupported nanosheets

Similar to the synthesis of Co_3O_4 cubes, two different techniques reported in literature [118,121] were applied to yield Co_3O_4 nanoparticles in a hexagonal sheet or platelet like morphology.

4.2.1 Supercritical hydrothermal synthesis - amine sheets

The synthesis technique reported by Hu et al. [121] and described in section 4.1.1 to synthesise Co_3O_4 cubes is used with only one change of solvent. $Co(NO_3)_2{\cdot}6H_2O$ (Sigma Aldrich 98% purity) is dissolved in deionised water instead of ethanol. The prepared sheets are termed amine nanosheets in the present study.

4.2.2 Hydrothermal precipitation synthesis - NaOH sheets

The group of Hou et al. [118] report a low cost and large scale synthesis route for cobalt oxide nanosheets. 1.4 g of $Co(NO_3)_2{\cdot}6H_2O$ (Sigma Aldrich 98% purity) is dissolved in 20 ml of deionized water yielding a pink solution. Under stirring, 20 ml of 0.5 M NaOH is added dropwise and the solution is left stirring at room temperature in an open beaker for 30 min. The pink precipitate is collected, washed with deionised water and dried at 60°C in a Memmert oven overnight. The hydroxide products are subsequently calcined in the Nabertherm furnace at 200°C for 3 hrs. The obtained sheets are labelled NaOH nanosheets in the present study.

4.3 Synthesis of unsupported nanobelts

The direct and scalable synthesis of nanobelts was reported in the work of Wang et al. [132]. 0.1 g of $Co(NO_3)_2{\cdot}6H_2O$ (Sigma Aldrich, 98% purity) and 0.6 g of urea are mixed in 10 ml of deionized water. The solution is rapidly heated to 95°C in a watch glass covered beaker and maintained at the set temperature for 12 hours under stirring. After cooling a pink precipitate is collected, re-suspended in deionised water and centrifuged (5000 rpm, 10 min) five times and subsequently dried at 50°C in a Memmert oven overnight. The resulting β-$Co(OH)_2$ nanobelts are calcined at 250°C in static air to yield Co_3O_4 nanobelts.

4.4 Synthesis of N-nanoparticles

In an earlier study in our laboratories, the effect of Co_3O_4 crystallite size in the CO-PROX reaction was investigated [3]. Nanocrystallites of various sizes ranging from 3.7 to 13.8 nm were prepared using a reverse micelle approach [133]. Crystallites with an average diameter of 10 nm were re-used in the present work (labelled N-nanoparticles) to allow for comparability of the two studies.

The preparation technique is described in detail elsewhere [3,133]. In short, 250 g of n-hexane (AR grade, Kimix) are combined with 25 g of Berol 050 (penta-ethyleneglycol-dodecylether: PEDGE, Akzo Nobel) and stirred for 1 hour at 800 rpm (Caframo RZR-1 overhead stirrer). A solution of 3.3 g of $Co(NO_3)_2.6H_2O$ (Sigma Aldrich, 98% purity) in 15 ml deionized water is added dropwise to the n-hexane-PEDGE mixture under stirring. A clear pink solution forms indicating the stability of the reverse micelles. 25 wt.% NH_3 aqueous solution (NH_3:Co^{2+} ratio of 4:1) is added dropwise over a period of 30 minutes upon which a colour change from red to light-green is observed indicating the formation of $Co(OH)_2$. The reverse micelles are not destabilised by this treatment and essentially retain the precipitate in their confined geometry [134]. The destabilization of the micelles and flocculation of the precipitate is achieved via the addition of acetone (Kimix). After settling, the precipitate is separated and washed several times with acetone. The washed solid is dried at room temperature in air and subsequently calcined at 200°C in a Nabertherm furnace yielding a black powder (Co_3O_4). The schematic representation of the procedure followed to perform the reverse micelle synthesis is shown in figure 4.1.

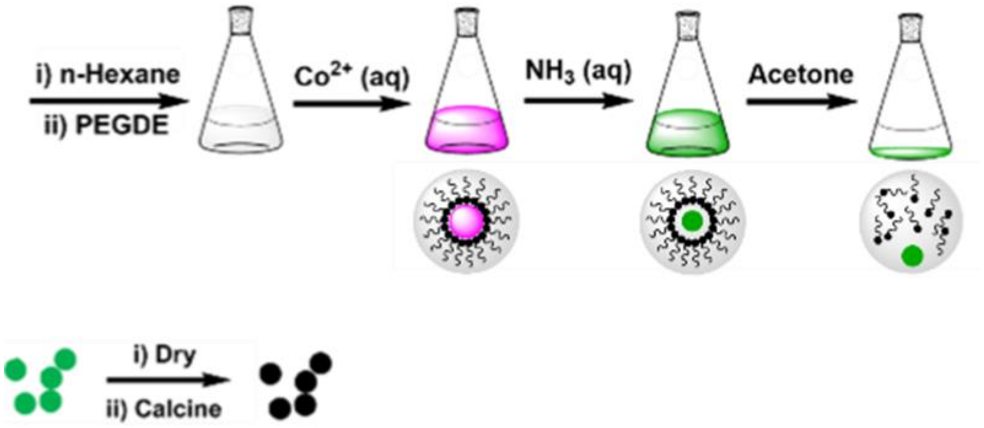

Figure 4.1: Steps followed to prepare Co_3O_4 N-nanoparticles with an average crystallite diameter of 10 nm [133]

4.5 Synthesis of support

4.5.1 Synthesis of Stöber SiO_2 spheres support

A method to prepare SiO_2 spheres or Stöber spheres via a seeded growth technique was reported by Stöber and Fink [135]. A continuous addition of Tetraethyl orthosilicate (TEOS) is used to develop monodisperse silica particles (150 nm ± 5% to 1.2 µm ± 1%) with fine spherical morphology. A solution of 0.5 ml TEOS (Sigma Aldrich reagent grade, 98%) and 2 ml of ethanol (Kimix) is quickly mixed with a solution of 50 ml of ethanol and 10 ml of 25 wt.-% ammonia (Kimix) under stirring and left for age for two hours.

A third solution containing 7 ml of TEOS and 28 ml of ethanol is transferred dropwise into the mixture under stirring and left aging for another two hours. The resulting white precipitate is washed with ethanol five times and dried at 60°C in a rotary evaporator (100 mbar) overnight.

4.6 Supporting Co_3O_4 nanoparticles

The prepared Co_3O_4 nanoparticles are loaded onto the synthesised SiO_2 support via a physical mixing procedure (target 5% Co_3O_4 loading). Co_3O_4 nanoparticles are initially suspended in deionised water for 1 hour using an erlenmeyer flask to reduce the degree of agglomeration. Under stirring, the support is added slowly to the suspension over 10 minutes. Prior to the addition of the support, the SiO_2 spheres were dried in the Nabertherm furnace at 350°C for 3 hours to remove residual moisture. After an additional sonication for 1 hour, the supernatant is dried off in a rotary evaporator (50 rpm, 60°C, 100 mbar) overnight.

4.7 Characterization of model catalyst and the support

4.7.1 Scanning Electron Microscopy (SEM), and Energy Dispersive X-ray spectroscopy (EDX)

In order to determine size and morphology and to an extent composition of the cobalt oxide and silicon dioxide particles synthesised, scanning electron microscopy coupled with EDX (LEO S444 SEM, Lα: Kα, UK) was used. The microscope is equipped with a four quadrant back scatter detector and an energy dispersive Fissons Kevex X-ray spectrometer (EDX). The chemical composition of the samples originating from synthesis techniques making use of NaOH (NaOH nanosheets) and HCl (HCl nanocubes) was determined, as the presence of these chemical compounds can potentially affect the performance of the catalyst. The samples were prepared by sprinkling the respective catalyst powder on an aluminium stub layered with sticky graphite paste to facilitate electron conductivity to/from the sample.

4.7.2 Transmission Electron Microscopy (TEM)

Transmission Electron Microscopy (TEM; Tecnai F20 TEM equipped with a field emission gun operated at 200 kV) was used to determine the size distribution and morphology of the prepared samples. The morphology, crystallite size and size distribution was obtained from the unsupported samples. The distribution on the silica carrier as well as potential morphological changes after exposure to reaction conditions were studied on the supported samples. For sample preparation, a small volume of solid is re-suspended in acetone using utrasonication. A droplet of the supernatant is transferred onto a holey carbon coated copper grid and dried in air for about 10 minutes before analysis.

The obtained micrographs were analysed with the freeware ImageJ to obtain particle size distributions. For statistical relevance about 200 - 250 particles were counted for each sample.

4.7.3 Powder X-ray diffraction (PXRD)

The crystalline phases and phase compositions were determined using Powder X-ray Diffraction (PXRD) on a Bruker AXS D8 Advance X-ray laboratory diffractometer operated at 35 kV and 40 mA utilizing a Co source ($\lambda_{Co\text{-}K\alpha1}$ = 1.78897 Å) and a VANTEC position-sensitive detector (Bruker AXS). Analysis were performed on both unsupported and supported samples with a scan range of 20° to130° 2Θ, a step-size of 0.01° and a scan rate of 0.025°/s. The diffraction peaks of the samples obtained were analysed against the peaks positions and intensities of reference patterns recorded in the ICDD PDF2 2006 database. The *in situ* studies were performed with the scan range of 20° to130° 2Θ.

4.7.4 Brunauer–Emmett–Teller surface area (BET)

The specific surface area and pore size distribution of the support was determined using the Brunauer-Emmett-Teller (BET) method based on physical adsorption and capillary condensation (Micromeritics TriStar 3000). The sample is cooled to liquid nitrogen temperature, followed by physical absorption (based on van der Waals interactions) of N_2 molecules from a known amount of gas onto the surface of the sample. From the amount of adsorbed gas, assuming a monomolecular coverage, a surface area can be calculated [136].

4.7.5 Temperature Programmed Reduction (TPR)

The reduction behaviour of the model catalysts was studied by temperature programmed reduction in a diluted hydrogen stream (Micromeritics AutoChem2910). About 100 mg of SiO_2

supported Co_3O_4 was loaded into a quartz reactor and dried in flowing argon (10 mL (NTP)/min) at 110°C (heating rate: 10°C/min) for 60 minutes. Subsequently the system was cooled to 60°C upon which a gas flow of 5% hydrogen in argon (50 mL (NTP)/min) was allowed to flow through the sample. The hydrogen consumption was monitored with a thermal conductivity detector (TCD) during a temperature ramp to 900°C (heating rate: 5°C/min).

4.7.6 Atomic Absorption Spectroscopy (AAS) and Inductively Coupled Plasma mass spectrometry (ICPMS)

To determine the metal loading of the Co_3O_4 on silica, both AAS and ICPMS were used to obtain representative metal loadings. For AAS analysis, the model catalyst was digested in a mixture of acids (6 mL concentrated hydrochloric acid (HCl), 2 mL concentrated hydrofluoric acid (HF), 2 mL concentrated nitric acid (HNO_3)) in a MARS-5 Microwave digester. Analysis was then carried out on a Varian SpectrAA-110 series instrument. The sample is introduced into a flame where it turns into atomic vapour. Cathode lamps are used to expose the sample with a radiation light. Each atom absorbs a certain wavelength of light. By measuring the radiation after passing through the sample, the concentration of the analyte can be linked to the amount of light absorbed.

For the ICPMS analysis, the sample is digested in 3 ml of HCl, 3 ml of HF and few drops of HNO_3 in a reactor containing bi-distilled water. The mixture is then heated to 130°C, stirred for about an hour and then cooled under a jet of water. To make sure that there is no residue, 60ml of H_3BO_3 is added under stirring. The solution is subsequently filtered and transferred to a volumetric flask. The solution is injected into a Varian OES 730 Series instrument as an aerosol where it is ionised as it passes through the plasma. Upon coming back to the ground state, the atoms emit energy which the instrument records in wavelength and intensity. These can then be interpreted based on the standards available and be related to the concentration of the element [137].

4.7.7 X-ray Photoelectron Spectroscopy (XPS

X-ray Photoelectron Spectroscopy (XPS) analysis was conducted externally (Cardiff University) to analyse the surface chemistry of the model catalysts. The technique is widely used to analyse the surface of the materials due to its relatively easy use and data interpretation. The spectrometer is equipped with a combination of pumps to obtain ultra-high vacuum of around 10^{-10} mbar as the analysis and detection of photoelectrons can only be achieved in a high-vacuum environment. Standard laboratory X-ray sources are used to generate X-ray photons by means of electron bombardment of a metal anode target (aluminium ($h\upsilon$ = 1486.6 eV) or magnesium ($h\upsilon$ = 1253.6 eV)) at a high potential of 15 kV emitting a $K\alpha_{1,2}$ radiation [138].

XPS is based on the photoelectric effect: X-rays (photon of energy $h\upsilon$) knock out electrons with binding energy (E_b) from the core shell of the sample molecule/compound (see figure 4.2) and the measurement of the photoelectron's kinetic energy is used to determine the elements in the sample [139]. The kinetic energy of the ejected electron is given as follows:

$$E_k = h\upsilon - E_b - \varphi \qquad \text{Equation 4-1}$$

Where υ is the is the frequency of the excitation radiation

E_b is the binding energy of the photoelectron with respect to the Fermi level of the sample.

φ is the work function of the spectrometer.

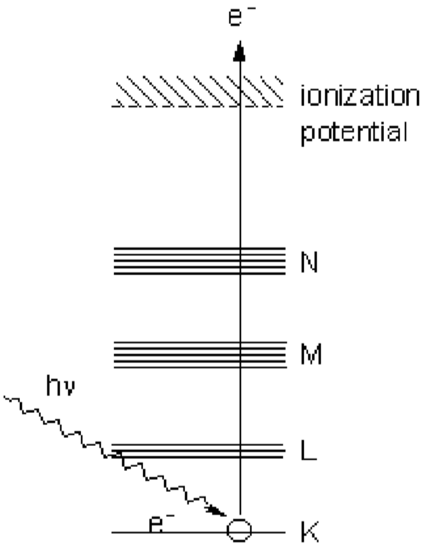

Figure 4.2: The process of photoelectron emission during XPS analysis. Adapted from Lablokov [139]

XPS was performed using a Kratos Axis Ultra-DLD photoelectron spectrometer, equipped with monochromatic Al Kα radiation, at 144 W power. Prior to analysis, samples were prepared by pressing into a layer of indium and degassing them in a vacuumed preparation chamber.

4.7.8 Magnetometer

Measurements based on sample magnetisation were carried out in an in house developed *in situ* magnetometer (schematically shown in Figure 4.3). The instrument is used to measure and monitor the degree of reduction (DOR) during CO-PROX experiments. The DOR is monitored by calculating the amount of metallic cobalt at a measured external field strength of 20 kOe [140].

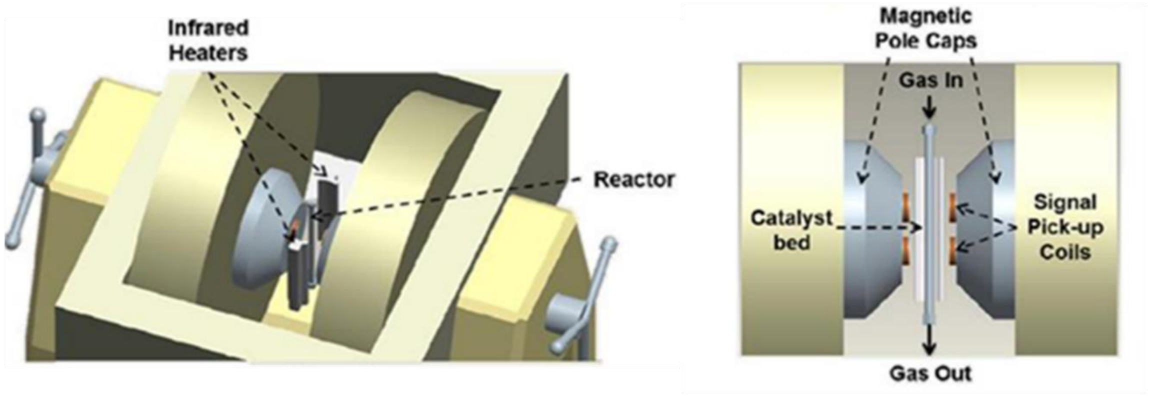

Figure 4.3: Schematic representation of in situ magnetometer. Maximum operating conditions: field strength of 20 kOe, maximum temperature of 750°C and pressure of 50 bar [29,140]

Figure 4.4 shows a process flow diagram of the *in situ* magnetometer. The setup consists of two mas flow controlled (MFC) feed gas lines supplying a premix gas (CO: 1.0%, H_2: 53.0%, N_2: balance AFROX) and synthetic air (O_2: 21.0%, N_2: balance). The gas stream can be directed either into the reactor or via a by-pass with three way valves (3WV). The reactor outlet gas is probed by an online GC-TCD system. All experiments are carried out at atmospheric pressure.

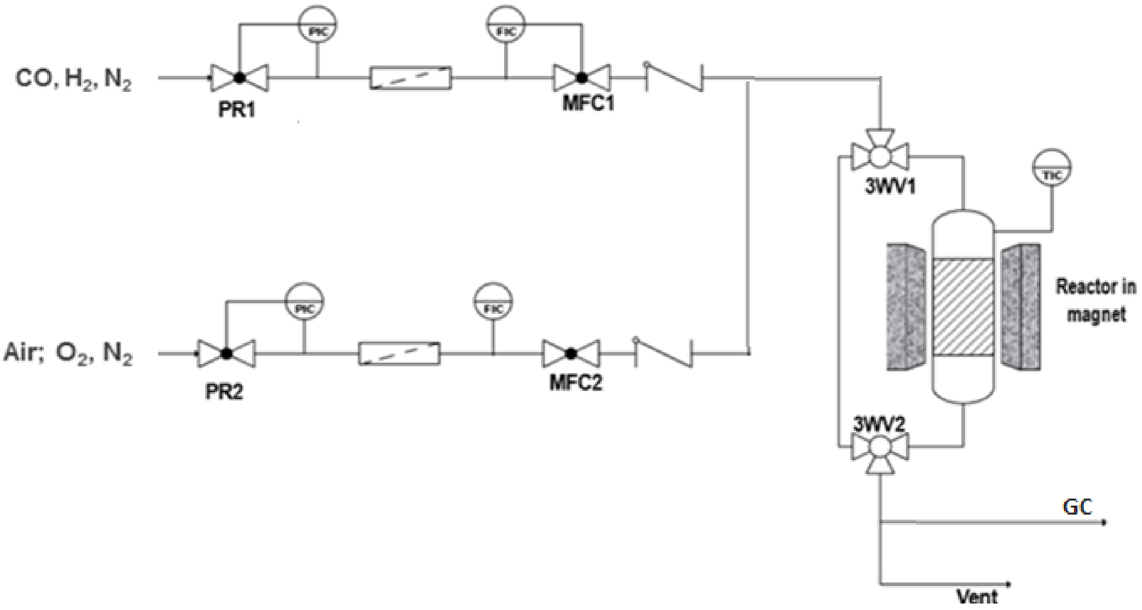

Figure 4.4: A schematic representation of a physical setup of the in situ magnetometer equipment. PR1 and PR2: pressure regulators, MFC1 and MFC2: mass flow controllers, 3WV1 and 3WV2: three way valves, GC: gas chromatograph

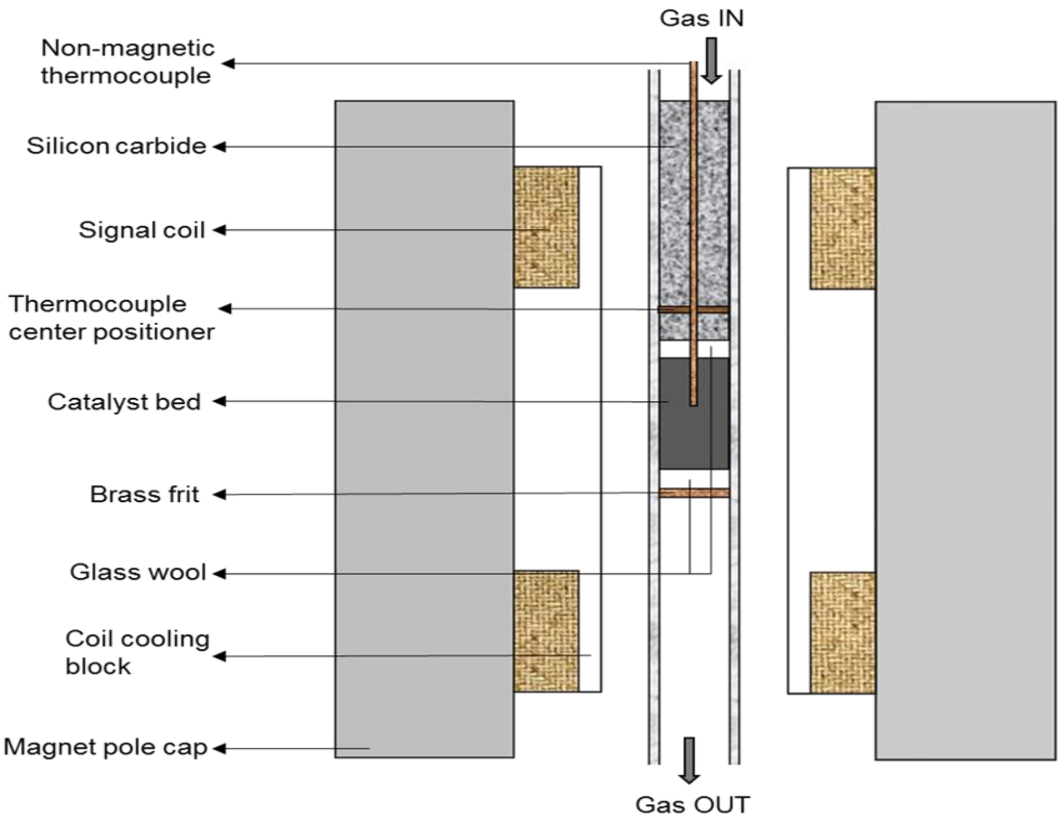

Figure 4.5: Cross section the in situ magnetometer set up showing the reactor inserted between magnetic poles [29,133]

The reactor is a ½" stainless steel tube with a fixed brass frit to stabilize the catalyst bed. The outside of the reactor is blackened in order to improve the absorption of heat from the IR heaters. The catalyst is loaded onto a bed of glass wool held in place by the brass frit and terminated with a second bed of quartz wool and a gas pre-heating zone of silicon carbide. A non-magnetic thermal-sensor (Pt 100 element) is inserted into the catalyst and a star-like guide is used to radially centre the sensor in the reactor.

In the presence of a magnetic sample, a voltage is induced in the Helmholtz signal pick-up coils by facilitating a vertical movement of the catalyst sample, i.e. the reactor, in the magnetic field. For maximum signal strength, the catalyst bed is centred between the signal pick-up coils by adjusting the position of the reactor in the holding bracket (see figure 4.6). The sample strength is calibrated with known amounts of metallic cobalt at different temperatures.

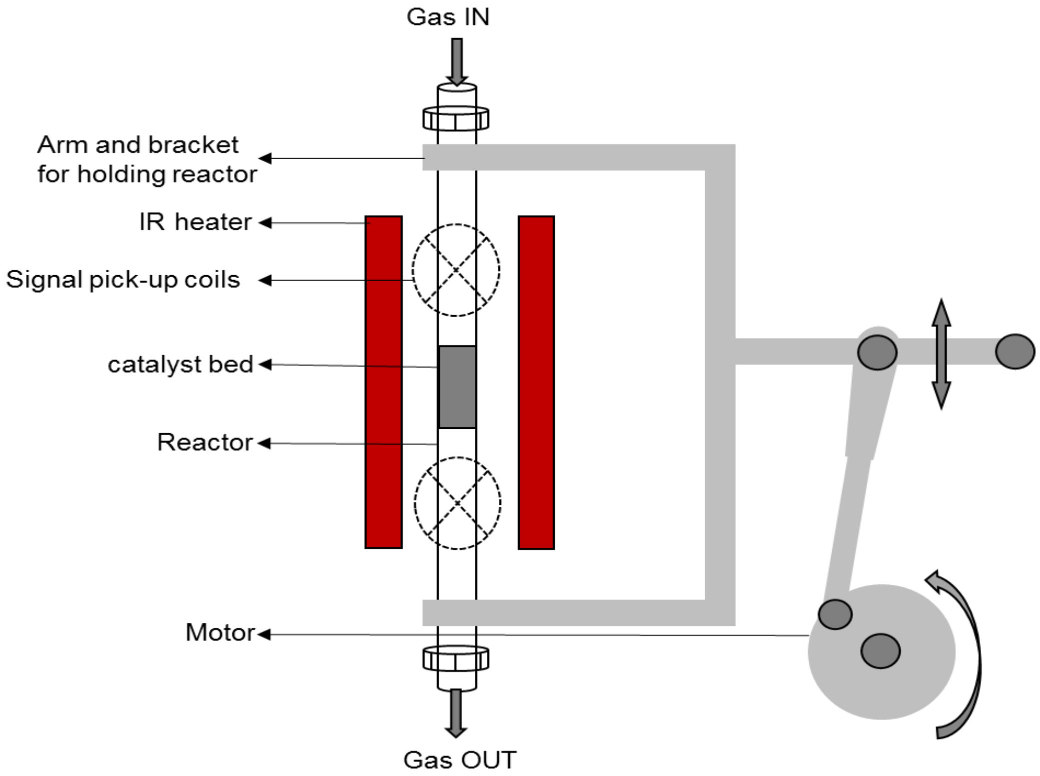

Figure 4.6: Side view In-situ magnetometer set up showing the reactor inserted between two IR heaters [29,133]

Online gas chromatography of the gases in the system is conducted using an Agilent Technologies 490 micro GC fitted with a thermal conductivity detector. The micro GC-TCD is equipped with three columns that allow independent analysis of the permanent gases. The first column is a 10 m Molecular Sieve 5A PLOT column with Ar as the carrier gas and is used for H_2 detection. The second column is a 20 m Molecular Sieve 5A PLOT column with H_2 as the carrier gas and is used for O_2, N_2, CH_4 and CO detection. The third column is made up of a 10 m PoraPlot Q column with H_2 as the carrier gas and is used for CO_2 detection.

The catalytic performance was studied at different temperature levels as outlined previously by Nyathi [3] (see figure 4.7). The temperature was ramped from 50 to 450°C and back to 50°C in steps of 25°C. Each temperature was held for 1 hour and changes of temperature were conducted at a ramp rate of 1°C/min. Magnetic readings were taken every 10 minutes at an external field strength of -20, 0, 20 and 0 kOe.

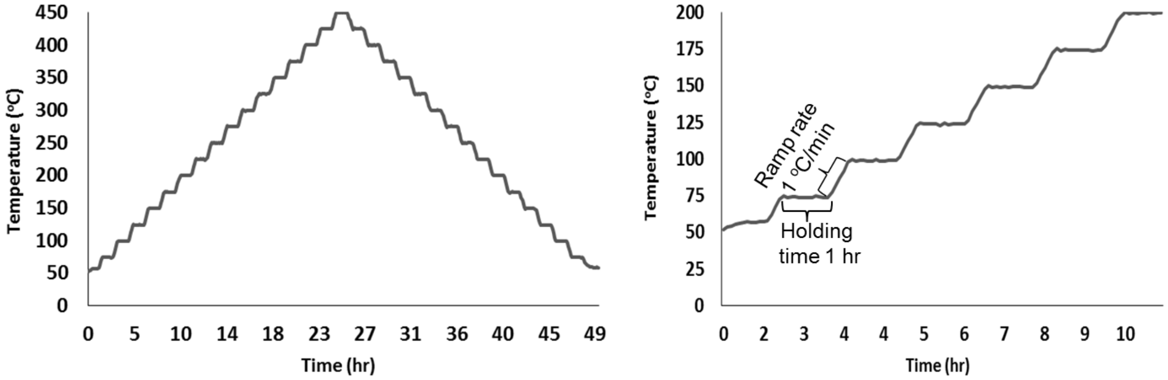

Figure 4.7: Schematic representation of the temperature program for both in situ PXRD and magnetometer

The required reactive gas mixture (CO:O_2 gas volumetric ratio of 1:1) was achieved through a volumetric mixing of synthetic air (21% O_2 in N_2, 99.99 % purity) and a pre-mixed gas consisting of 1% CO, 53% H_2 in a balance of N_2. Experiments were conducted at atmospheric pressure with 1 g of catalyst, and the gas flow rates were varied (between 90-100 ml (NTP)/min) depending on the mass of Co_3O_4 loaded to achieve a gas hourly space velocity (GHSV) of 120000 ml/(g.hr), twice the GHSV reported by in Nyathi [3] as a result of Co_3O_4 loading lower by a factor 2 in the present study.

The magnetisation of the catalyst was measured every 10 minutes at an external applied field of -20, 0, 20 kOe and again at 0 kOe during the heating phase of the experiments (50°C to 450°C), as well as the subsequent cooling of the partially reduced sample to 50°C. The magnetic results were used to determine the saturation magnetisation of the sample (M_s) at 20 kOe, and the fraction of the sample that exhibit remnant magnetisation (M_{rem}) at 0 kOe. The saturation magnetisation of the sample (M_s) is used to calculate the degree of reduction (see Appendix A). At the temperature of 50°C (end of the experiment), after cooling of the sample, a full measurement of the sample magnetisation as function of external field strength (65 magnetisation readings) was conducted.

4.7.9 *In situ* Powder X-ray Diffraction

The *in situ* PXRD equipment was used along the magnetometer to monitor the bulk phase changes (Co_3O_4 to CoO to Co) under identical conditions as described in section 4.7.8 above. 8-10 mg of catalyst could be loaded into the capillary cell reactor and the flow rates were reduced accordingly to maintain the GHSV of 120000 ml/(g.hr), and the $CO:O_2$ volumetric ratio of 1:1. The utilized cell was previously developed at the University of Cape Town [30,134,140] (see figure 4.8) and can achieve a maximum operating temperature and pressure of 500°C and 25 bar respectively. The *in situ* cell was installed in a Bruker D8 Advance X-ray diffractometer equipped with a cobalt source (Co-Kα1 wavelength 1.78897 Å). The catalyst sample was placed in a borosilicate capillary tube (75 mm long, ID = 1.0 mm, wall = 0.01 mm, Capillary Tube Supplies LTD, UK). Care was taken to ensure that the catalytic bed was loaded within the isothermal zone (15 mm length at the centre of the heating assembly) of the cell and was held in place by quartz wool plugs [142]. A thermocouple (Temperature Controls, RSA) was placed inside the capillary reactor tube (see figure 4.8) with its tip at the end of the catalyst outside the X-ray beam path to avoid diffraction of the steel components. A polyimide film (DuPont, Kapton, RS components) mounted to a stainless steel shield was used to cover the capillary reactor tube and avoid extensive heat loss through convection and improve the temperature stability.

The scan range was chosen from 40° to 80° 2Θ, with a step size of 0.03083045° and a time per step of 0.2 seconds. The short time of 4.56 minutes per scan with a 2.72 minutes (total time of 7 min 16 sec) of delay between scans was used to maximize the temporal resolution and to minimize the possibility of phase change during a scan. A total of six measurements were collected per temperature step.

.

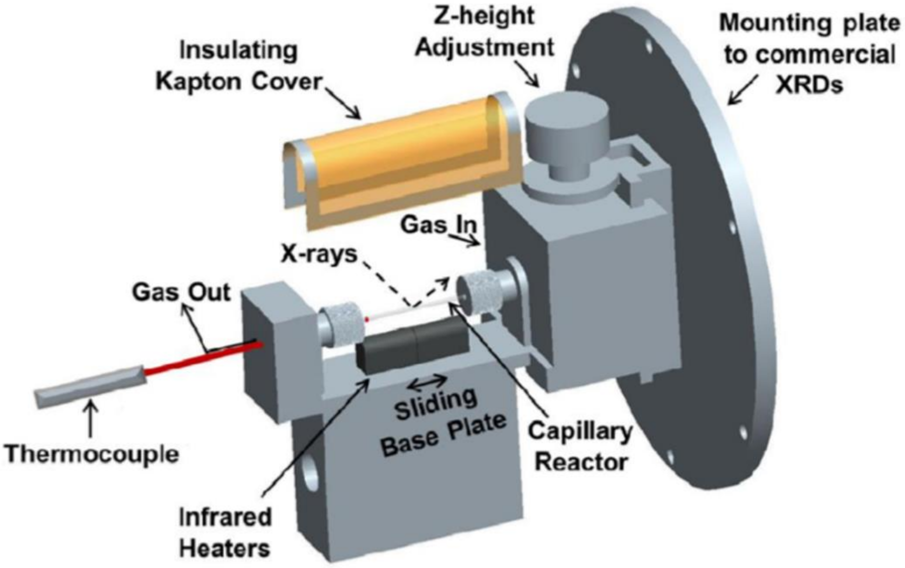

Figure 4.8: Schematic representation of the in situ Powder X-ray Diffraction capillary cell reactor. The catalyst is placed in the capillary cell. The thermocouple controls the temperature output of the infrared heaters to control the catalyst bed temperature [30,140]

4.7.10 Product analysis

The relative amounts of gaseous compounds in the reactor outlet gas were determined using their respective peaks obtained from the GC-TCD. The area of each peak was related to molar flow rates in the gas mix by their respective calibration factors and the known flow of a reference gas, here nitrogen.

$$F_i = \frac{A_{N_2} n_i}{A_i n_{N_2}} \qquad \text{Equation 4-2}$$

$$\dot{n}_i = F_i \cdot \left(\frac{A_i}{A_{N_2}}\right) \cdot \dot{n}_{N_2} \qquad \text{Equation 4-3}$$

Where $\boldsymbol{F_i}$ is the response factor of gas component $\boldsymbol{i}$ with reference to nitrogen. $\boldsymbol{A_{N_2}}$ is the measured peak area of nitrogen and $\boldsymbol{A_i}$is the measured peak area of gas component $\boldsymbol{i}$. $\boldsymbol{n_{N_2}}$ is the molar gas flow rate of nitrogen and $\boldsymbol{n_i}$ is the molar gas flow rate of gas component $\boldsymbol{i}$. The response factors relative to nitrogen of all components are obtained by analysing a calibration gas mixture with known concentrations. Based on these factors restructuring of equation 4-2 allows to obtain the different gas flow rates in the presence of the known nitrogen gas stream.

CO conversion ($\boldsymbol{X_{CO}}$), CO$_2$ yield ($\boldsymbol{Y_{CO_2}}$), O$_2$ selectivity to CO$_2$ ($\boldsymbol{S^{O_2}_{CO_2}}$); and the CH$_4$ yield ($\boldsymbol{Y_{CH_4}}$) were calculated using the following equations:

$$\boldsymbol{X_{CO}}\ (\%) = \frac{n_{CO,in}-n_{CO,out}}{n_{CO,in}} \times \mathbf{100} \qquad \text{Equation 4-4}$$

$$\boldsymbol{Y_{CO_2}}\ (\%) = \frac{n_{CO_2,out}}{n_{CO,in}} \times \mathbf{100} = \frac{n_{CO,in}-n_{CO,out}-n_{CH_4,out}}{n_{CO,in}} \times \mathbf{100} \qquad \text{Equation 4-5}$$

$$\boldsymbol{S^{O_2}_{CO_2}}\ (\%) = \frac{n_{CO_2,out}}{2\cdot(n_{O_2,in}-n_{O_2,out})} \times \mathbf{100} = \frac{n_{CO,in}-n_{CO,out}-n_{CH_4,out}}{2\cdot(n_{O_2,in}-n_{O_2,out})} \times \mathbf{100} \qquad \text{Equation 4-6}$$

$$\boldsymbol{Y_{CH_4}}\ (\%) = \frac{n_{CH_4,out}}{n_{CO,in}} \times \mathbf{100} = \frac{n_{CO,in}-n_{CO,out}-n_{CO_2,out}}{n_{CO,in}} \times \mathbf{100} \qquad \text{Equation 4-7}$$

Where $\boldsymbol{n_{CO,in}}$ is the molar gas of CO and $\boldsymbol{n_{O_2,in}}$ is the molar gas flow of O$_2$ into the reactor. $\boldsymbol{n_{CO,out}}$, $\boldsymbol{n_{O_2,out}}$, $\boldsymbol{n_{CO_2,out}}$ and $\boldsymbol{n_{CH_4,out}}$ are the respective molar gas flows at the reactor outlet.

5 Results and discussion

5.1 Characterisation of unsupported particles

Co_3O_4 nanocrystallites of different morphology and SiO_2 Stöber spheres were synthesised. To study the geometric shape and phase composition of the synthesized materials, electron microscopy as well as PXRD was applied.

5.1.1 Electron microscopy (TEM and SEM)

With the electron microscopic techniques, the success of the different synthesis techniques in yielding well defined morphologies of CO_3O_4 nanocrystallites and SiO_2 Stöber spheres could be confirmed (see figure 5.1).

Both preparation techniques targeting Co_3O_4 cubes, namely HCl and amine cubes, yielded fairly monodisperse cubic shaped crystallites. Independent of synthesis route the achieved cube sizes are very comparable with regard to edge length (amine cubes: 52.4 ± 4.3 nm, HCl cubes: 55.2 ± 5.1 nm).

Significant differences in size could be observed for the sheets or platelets. While both synthesis routes resulted in the formation of irregular hexagonal or truncated equilateral triangular shapes, their dimensions differ. The amine based route resulted in sheets of an average height/thickness of 42.5 ± 7.76nm and a length of 247.0 ± 21.9 nm. The length is defined as the distance between two opposite parallel edges. Sheets prepared based on the precipitation of the metal nitride solution with NaOH displayed an average height/thickness of 23.6 ± 8.9 nm and a length of 113 ± 14.0 (see figure 5.2). Higher resolution images of the sheets seem to indicate the presence of small crystallites (amine nanosheets: 13.6 ± 3.4 nm, NaOH nanosheets: 8.7 ± 1.8 nm) constituting the larger platelet structures. The observed agglomeration of both samples is expected based on the geometry induced strong interfacial tension [143].

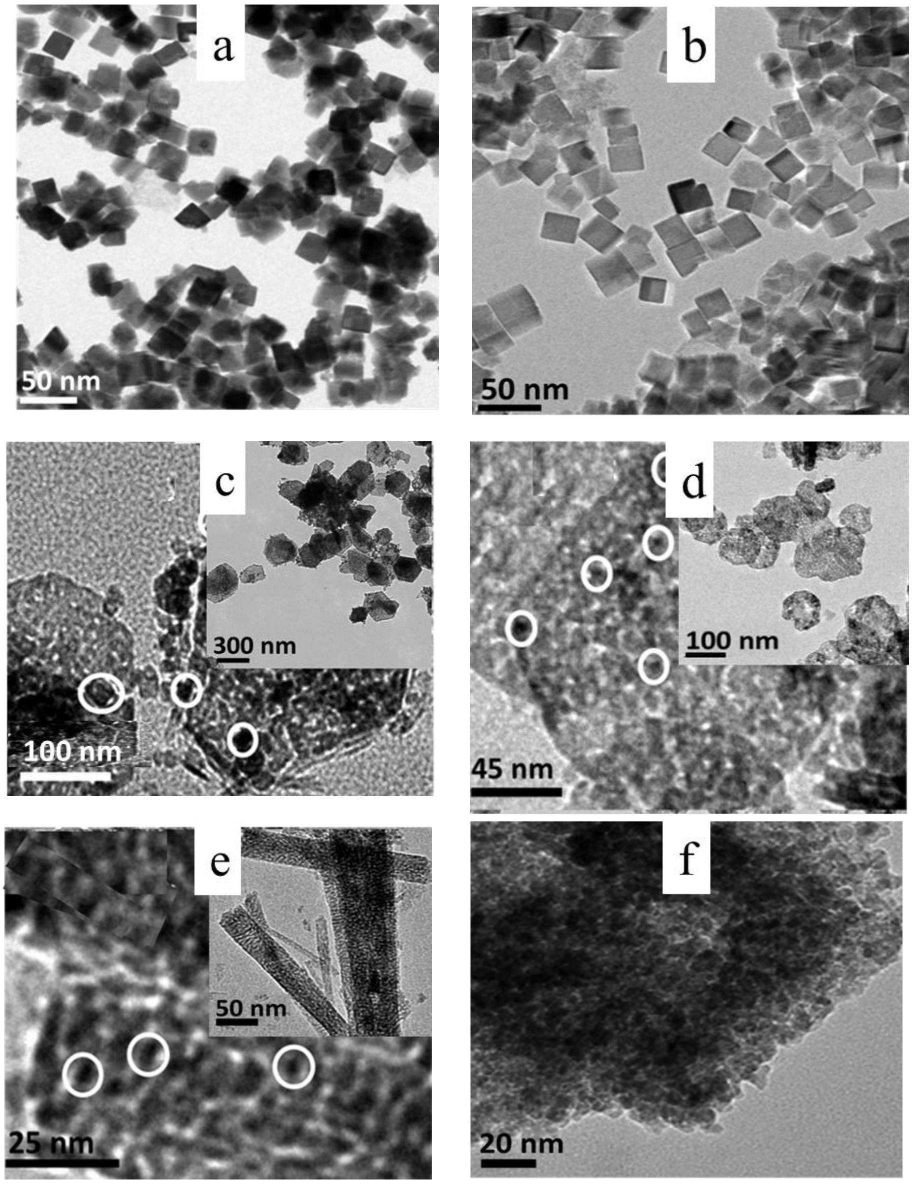

Figure 5.1: TEM micrographs for unsupported Co_3O_4 *particles for the amine nanocubes (a) and HCl nanocubes (b), amine nanosheets (c) and NaOH nanosheets (d), nanobelts (e) and N-nanoparticles (f)*

Similar to the nanosheets, the nanobelts obtained seem to be composed of self-assembled nanoparticles of an average size of 5.1 ± 1.2 nm (see figure 5.2) similar to the observations recently reported by Che et al. [144] The superstructures vary strongly in length (310-400 nm) and width (15-77 nm) as well as average thickness (19.7 ± 7.6 nm).

The conventional nanoparticles obtained from Nyathi [3] had average crystallite diameter of 10.5 ± 1.9 nm.

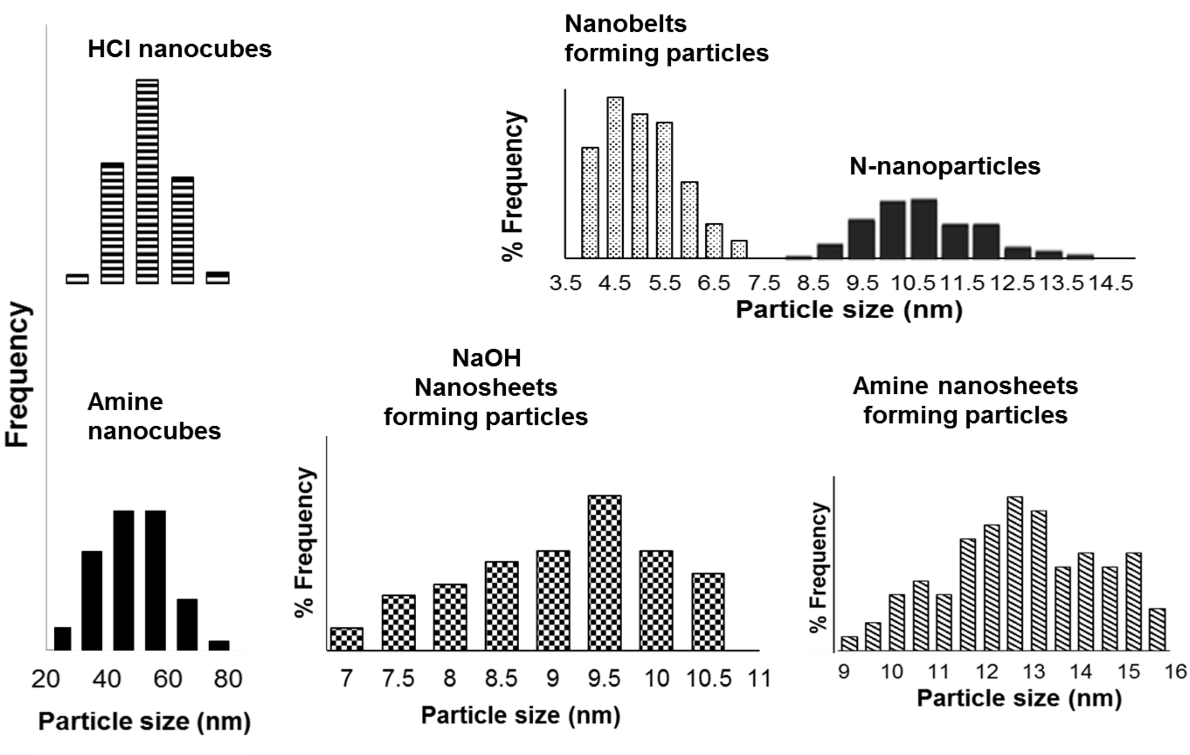

Figure 5.2: Crystallite size distribution of unsupported Co_3O_4 as determined by TEM micrographs analysis

The prepared Stöber spheres [135] (see figure 5.3) displayed a narrow size distribution and uniform spherical morphology with an average diameter of 1.47 ± 0.146 µm. The prepared morphology orientated Co_3O_4 crystallites and the nanoparticles from the study by Nyathi [3] were supported on the Stöber spheres as described in section 4.5. The cubical particles as well as the N-nanoparticles seem to show a fairly good distribution on the support spheres with intimate contact between the cobalt oxide crystallite and the SiO_2 surface (see figure 5.4 a & d). Due to their different geometry both platelets and belts show a more heterogeneous distribution of particles on the support, varying between close contact and minimal interaction, i.e. only connected via an edge of the Co_3O_4 crystallite/superstructure (see figure 5.4 b & c).

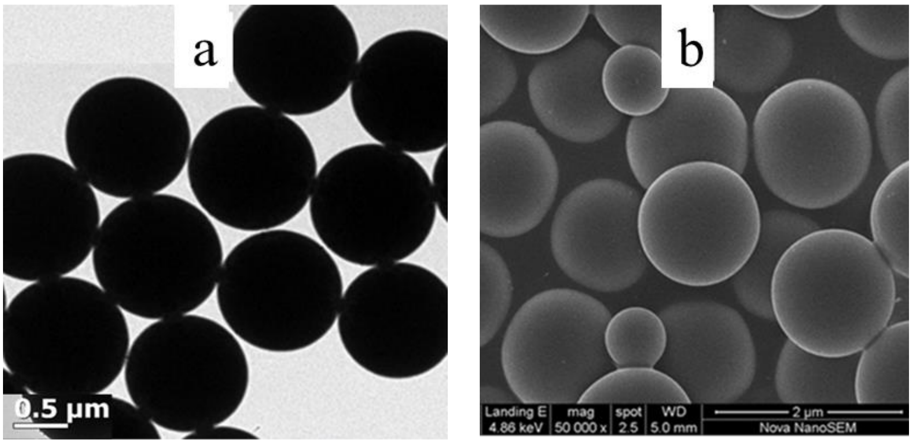

Figure 5.3: TEM (a) and SEM (b) micrographs of unloaded SiO_2 support

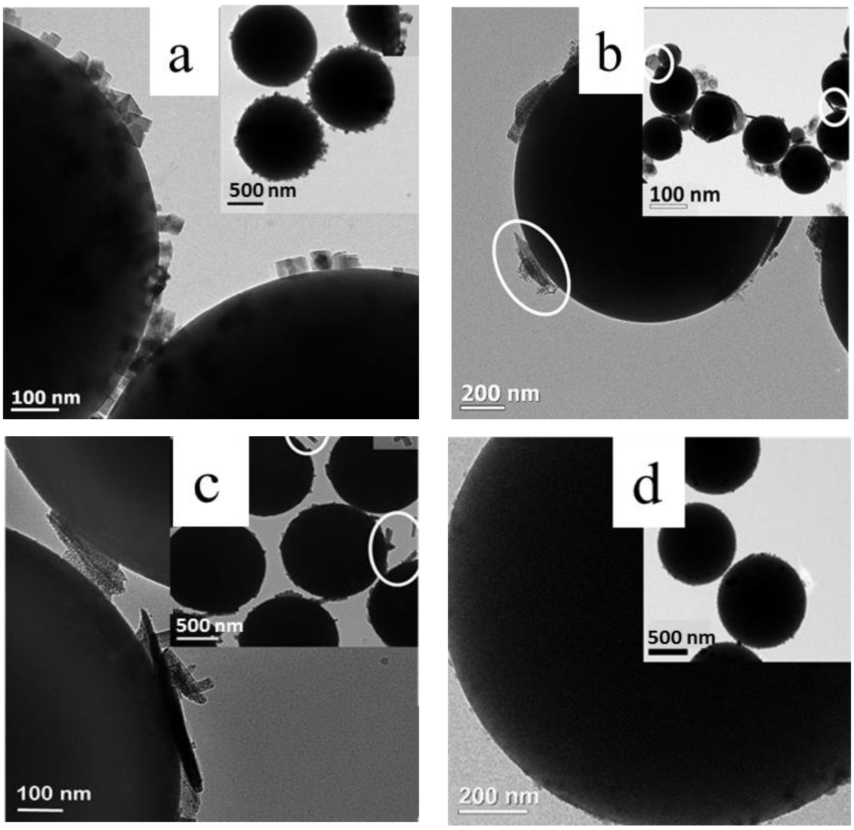

Figure 5.4: TEM of the nanocatalysts supported on spherical silica support. Amine nanocubes (a), amine nanosheets (b), nanobelts (c) and N-nanoparticles (d)

5.1.2 PXRD analysis

With PXRD the presence of a pure Co_3O_4 spinel phase was evidenced for all samples (see figure 5.5). The obtained diffraction patterns were compared visually to the reference pattern of 01-073-1701 (face-centred cubic Co_3O_4) from the ICDD PDF2 database. Although crystallite sizes obtained from a peak broadening analysis as well as Rietveld refinement is difficult to interpret due to the targeted morphologies, especially for the platelet and belt samples, the obtained average crystallite sizes are shown in table 5.1. Both cubes as well as the nanoparticles yield similar average crystallite sizes as obtained from analysis of the TEM micrographs. The slightly lower size of the cubes could stem from the presence of multiple crystalline domains within one macroscopic cubical structure which are not distinguishable in TEM. The average crystallite sizes of sheets and belts obtained from PXDR are significantly lower than expected from microscopy. Both the belts and platelets have been identified as superstructures of small crystallites, and the here obtained average crystallite diameter of 5.1 nm (nanobelts), 13.2 nm (amine nanosheets) and 8.7 nm (NaOH nanosheets) could be associated to the dimension of these crystallites (see figure 5.2).

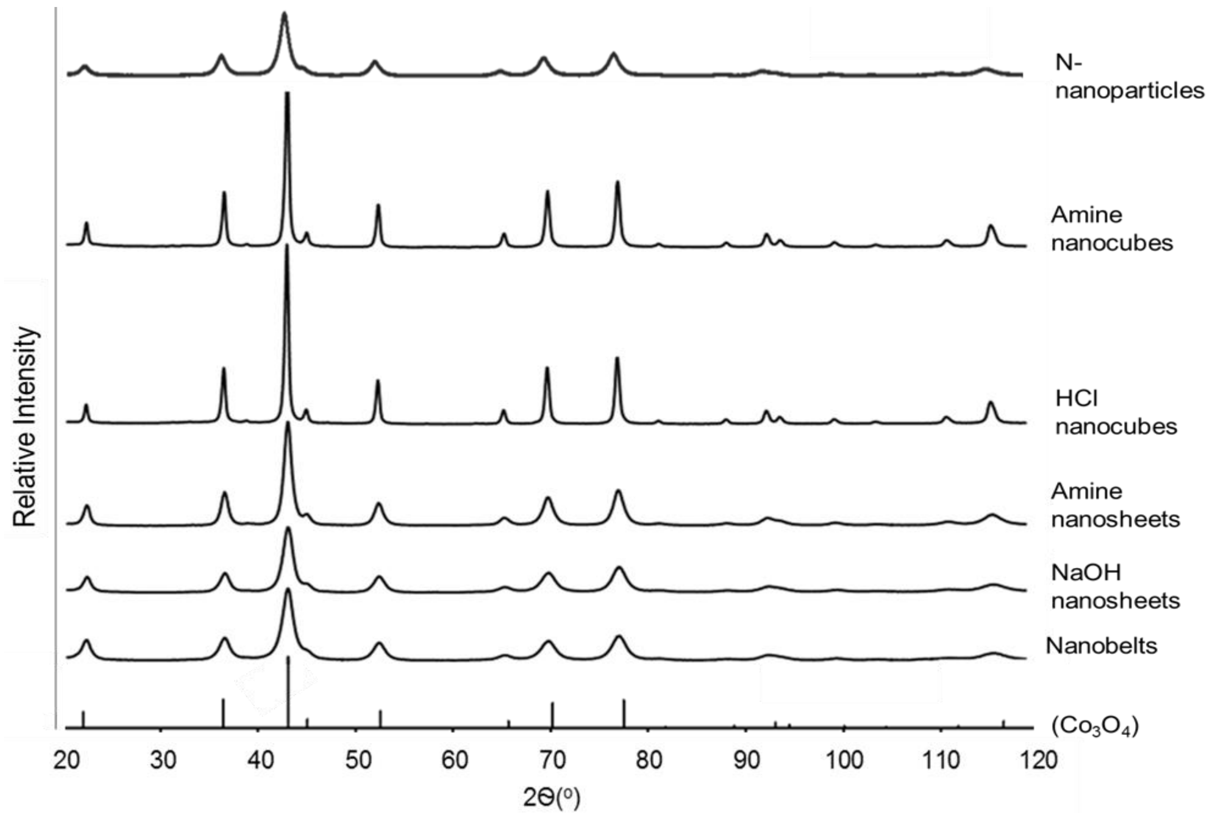

Figure 5.5: PXRD diffractograms of unsupported Co_3O_4 particles and reference pattern for Co_3O_4

Table 5.1: Average crystallite size of the six samples as obtained from PXRD

Sample	Amine cubes	HCl cubes	Amine sheets	NaOH sheets	Belts	N-nanoparticles
d_{Co3O4} (nm)	34.2	36.3	13.2	8.7	5.1	12.2
R_{WP}	9.5	11.2	9.5	8.9	8.6	8.4
Scherrer formula	22.6	22.4	10.0	7.5	5.0	10.5

5.2 Characterisation of supported particles

5.2.1 PXRD analysis of supported particles

As the process of depositing the synthesized cobalt oxide nanoparticles on the SiO_2 Stöber spheres is a mere physical mixture (see section 4.6) no changes in the phase structure or crystallite size are expected. PXRD scans of the supported model catalyst samples show the presence of the spinel oxide as only detectable cobalt species while the SiO_2 spheres appear to be amorphous, as previously described in literature [145], and only contribute to the diffraction pattern with a broad hump at 2Θ values below 40° (see figure 5.6). The obtained crystallite sizes calculated via peak broadening analysis and Rietveld refinement (the SiO_2 contribution is modelled as a single peak phase) compare well to the values obtained for the unsupported samples (see table 5.1).

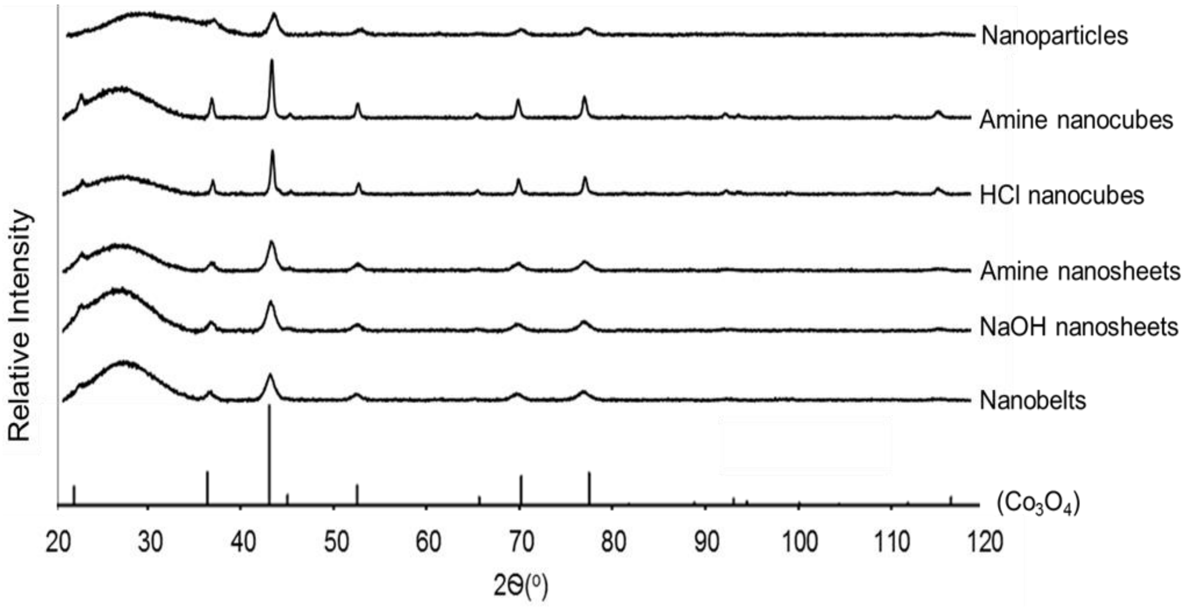

Figure 5.6: PXRD diffractograms of supported Co_3O_4 nanoparticles

5.2.2 ICP and AAS of supported particles

Due to the non-crystalline nature of the support, cobalt concentrations could not be extracted from the PXRD data. The loadings were measured by AAS and ICP (see table 5.2). Both techniques yield comparable results and close to the targeted 5 wt.-% Co_3O_4.

Table 5.2: Co_3O_4 loading on SiO_2 in weight percentage as obtained by AAS and ICP.

wt.-%	Amine cubes	HCl cubes	Amine sheets	NaOH sheets	Nanobelts	Nanoparticles
AAS	4.24	4.06	4.60	4.44	4.33	4.55
ICP	4.19	4.11	4.29	4.45	4.29	4.55

5.2.3 X-ray Photoelectron Spectroscopy (XPS) of unsupported samples

XPS analysis is a surface-sensitive spectroscopic technique powerful for characterising the surface properties of materials (approximate penetration depth is 1–5 nm). The XPS spectrum of the HCl nanocubes is shown in figure 5.7 (for spectra of other catalyst samples (see appendix C: XPS profiles). The position of the binding energy of Co $2p_{3/2}$ at ~777.0 eV and Co $2p_{1/2}$ at 792.0 eV and the weak shake-up satellites at 787.0 eV and 800.0 eV indicate the presence of Co^{3+} and Co^{2+} evidencing the main cobalt phase to be Co_3O_4. These features can be observed in all samples of the present study. Though it could not be quantified, the spectra also show contributions associated to the Cl $2p_{3/2}$ peak with a binding energy of 197.5 eV [146,147]. Clearly the applied sample washing and calcination procedure (see section 4.1.2) was not sufficient to fully remove all chlorine from the Co_3O_4 surface. Other samples did not show any evidence of chlorine.

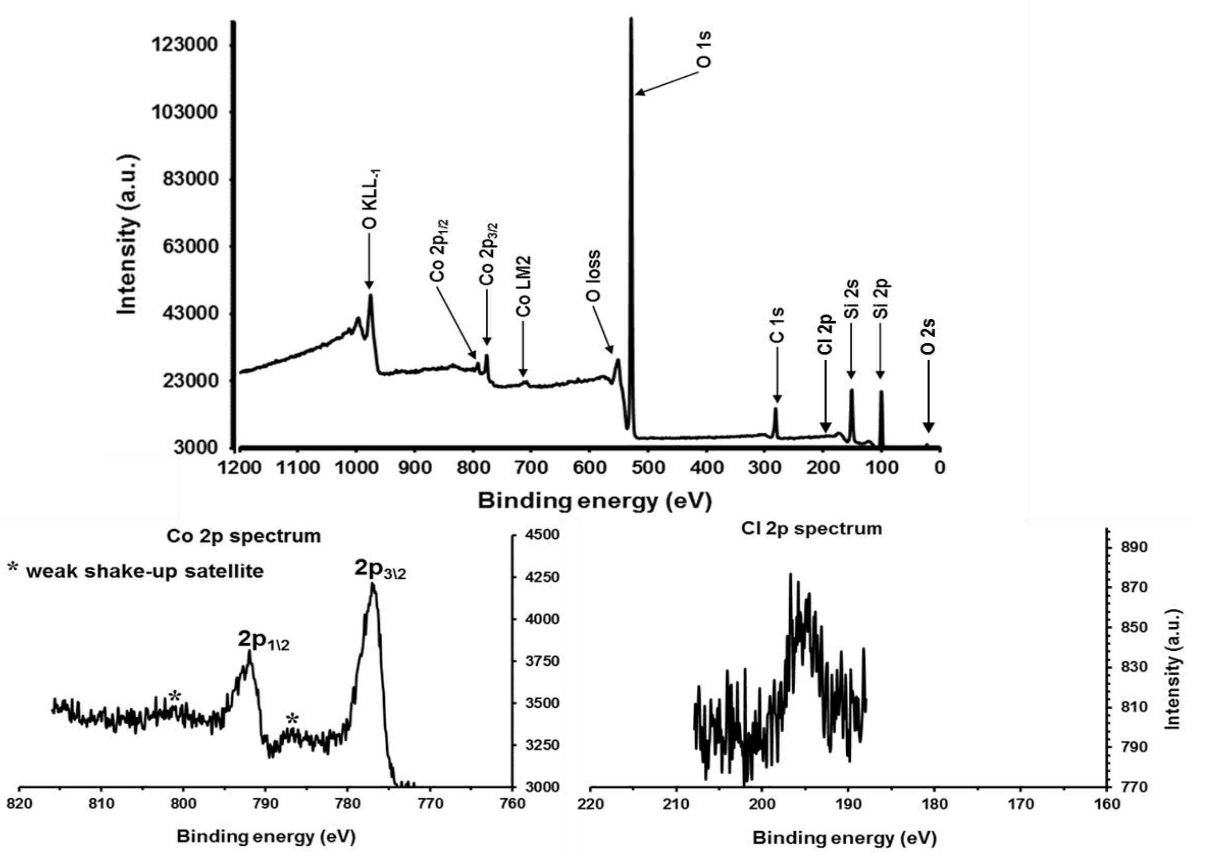

Figure 5.7: Wide scan energy spectrum of the Co_3O_4 HCl nanocubes acquired using a silver anode (top), zoom in of Co 2p spectrum (bottom left) and Cl 2p spectrum (bottom right)

5.2.4 Temperature Programmed Reduction (TPR)

The effect of morphology on the reducibility, in the context of CO-PROX the expected deactivation mechanism at elevated temperatures, was studied in H_2-TPR. These measurements can also give information about the degree of metal oxide - support interaction [148] although only low levels of interaction are expected based on the loading process [149]. By heating the samples in a diluted hydrogen stream from 60°C to 900°C and recording the hydrogen consumption as a function of temperature, both the multistep reduction of Co_3O_4 (see equation 5-1 to 5-2) as well as the degree of reduction can be resolved.

$$Co_3O_4(s) + H_2(g) \rightarrow 3CoO(s) + H_2O(g) \qquad \text{Equation 5-1}$$

$$CoO(s) + H_2(g) \rightarrow Co(s) + H_2O(g) \qquad \text{Equation 5-2}$$

Khodakov et al. [150] have demonstrated that the reduction of Co_3O_4/SiO_2 to Co/SiO_2 occurs in two steps from Co_3O_4 to CoO (see Equations 5-1) in the temperature range of 200-300°C, followed by the reduction of CoO to Co^0 (see equations 5-2) which is strongly dependant on crystallite size. Nanoparticles with the crystallites size of about 6 nm are reported to be more difficult to reduce than larger particles (20-70 nm) due to their higher degree of support interaction [3,151]. The absolute temperature of reduction as well as the observed number of apparent reduction events, i.e. distinct hydrogen consumption peaks, can vary from study to study depending on the support used (metal oxide support interaction), synthesis method, crystal size and metal loading [151–154].

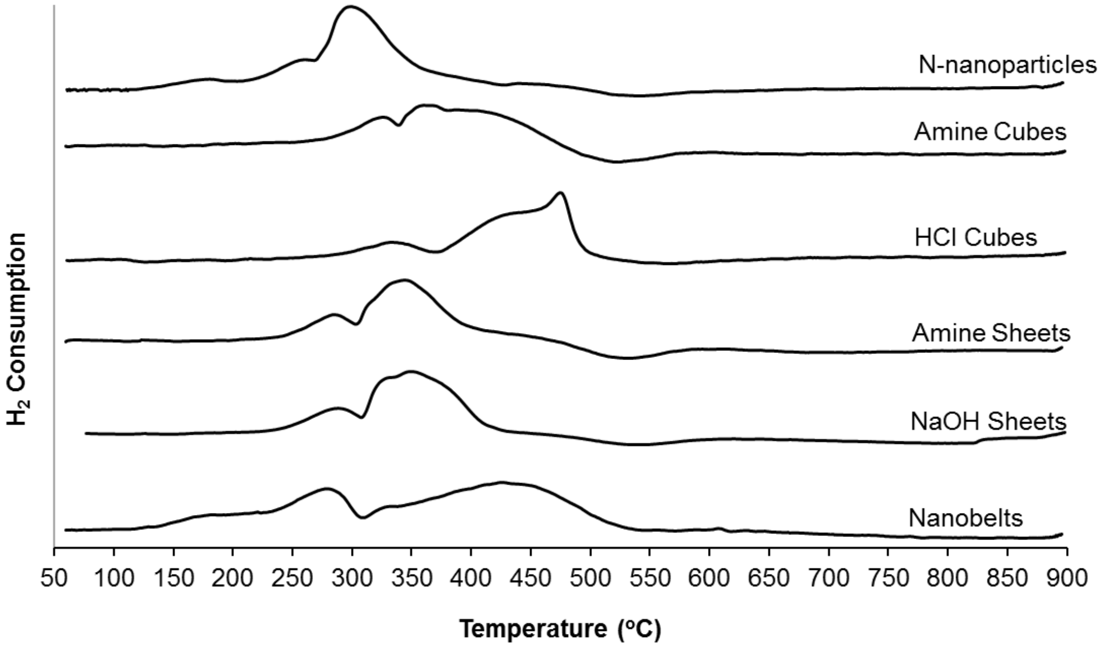

Figure 5.8: Mass normalised TPR profiles of silica supported Co_3O_4 nanoparticles

Table 5.3: Calculated degrees of reduction based on hydrogen consumption from Co_3O_4 TPR profiles

Conditions	Sample label	Mass loaded (g)	Degree of reduction %
	N-nanoparticles	0.118	96.8
Ramp rate: 5°C/min	Amine cubes	0.104	94.5
T_{max}: 900°C	HCl cubes	0.089	92.1
Gas: 5% H_2 in Ar	Amine sheets	0.199	95.5
Gas flowrate: 50ml/min	NaOH sheets	0.181	97.2
	Belts	0.143	90.8

Figure 5.8 shows the TPR profiles of all the prepared model catalysts and N-nanoparticles. All the catalysts show the major reduction events between 150°C and 500°C which is in agreement with the reduction process of Co_3O_4, indicating the presence of weak interactions between the Co^{x+} and the surface of the silica support [141,150,151]. In principle, the ratio of consumed hydrogen from a first (Co^{3+} - Co^{2+}) to a second step (Co^{2+} - Co^{o}) is 1:3. In the present study, reduction events beyond the theoretically predicted two steps are observed. At most, about a total of four peaks can be observed, which are described as the reduction of oxidic cobalt phases (Co_3O_4, CoO) directly to metallic Co^0, Co_3O_4 to CoO and cobalt support crystallite (in this case cobalt silica crystallite) [151].

For analysis and comparison purposes, the hydrogen consumption of the TPR profiles was normalized and plotted as cumulative consumption as function of temperature (see figure 5.9). From the gradient of the resulting curves as well as potential points of inflexion, the onsets of distinct reduction events can be compared. N-nanoparticles reduce earliest with an onset at approximately 150°C. A second stage reduction evidenced by an increase in hydrogen consumption rate is detected at 225°C. The increased rate could be a result of a catalytic effect of present metallic Co^0 species in the dissociation of gaseous hydrogen.

These two stages can be assigned to an initial reduction of some Co_3O_4 to CoO followed by a mixed of reduction events from Co_3O_4 to CoO or Co and CoO to Co. Just before reaching the maximum degree of reduction of 96.8%, a third step can be observed at approximately 425°C. This could be a result of cobalt oxide interacting with the support surface. Strong metal support interactions in form of cobalt silicates would be expected at even higher temperatures.

An initial hydrogen consumption of the nanobelts is registered at comparable temperatures to the N-nanoparticles. This is in accordance with the illustration of the slab model in figure 2.16 shown by Hu et al. [121]; nanobelts expose high index {112} and {011} planes respectively. The high index planes are very reactive since they have a loose packing and high concentration of atoms on the surface. The validity of this model is however unclear as the nanobelts in the present study can be described as superstructures of small crystallites rather than single crystals. A second reduction event can be measured at 240°C with no significantly increased rate of reduction, reaching maximum DOR at 500°C. Of all samples, the ratio of main first to second reduction event is the highest with a ratio of 1:4. The synthesis process for the sheets/platelets, although affecting the geometry and size, does not seem to have an effect on the reducibility. Both samples reduce initially at 220-240°C with a second reduction event at 300°C and maximum DOR reached at 425-450°C. The reduction temperature of the first reduction step is significantly higher than in the case of the nanobelts even though PXRD and TEM data suggest similar single crystallites constituting the respective superstructure. Seemingly the environment generated by the superstructure has an additional influence on the reducibility. The morphology specific behaviour in the case of the platelets is not observed for the nanocubes. While the amine nanocubes reduce to a small extent (low hydrogen consumption) at only 175°C and a second reduction event is recorded at 290°C, HCl cubes only start reducing at 225°C, a first reduction step which constitutes approximately 25% of the total Hydrogen consumption and is therefore in line with the theoretical prediction, and show a second reduction event at 375°C. Possibly the residual chlorine as evidenced by XPS (see section 5.2.3) plays a role in the retardation of the reduction.

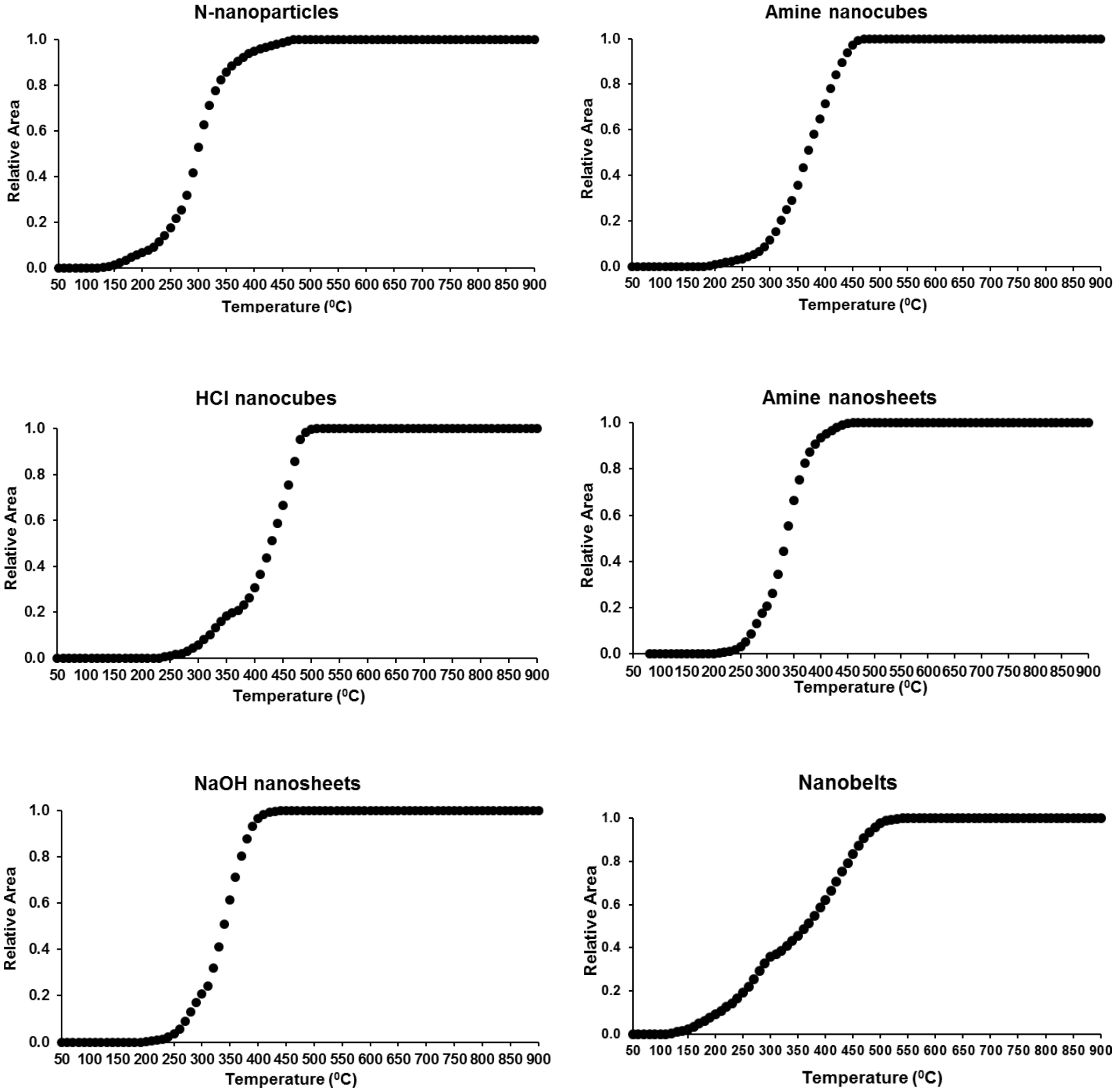

N-nanoparticles

Amine nanocubes

HCl nanocubes

Amine nanosheets

NaOH nanosheets

Nanobelts

Figure 5.9:Cumulative area under the H_2-TPR of model catalysts

5.3 Catalytic performance in CO-PROX reaction

All prepared Co_3O_4 nanoparticles were supported on SiO_2 using the loading technique described previously (see section 4.6). A Co_3O_4 concentration of 5 wt.-% was targeted with an actual loading between 4.1 and 4.6 wt.-% achieved. Potential differences in metal support interaction can therefore be assumed to originate from size and morphology differences between the various synthesized nanoparticles. To allow for comparison with a previous study in our laboratories focusing on crystallite size dependencies of alumina supported Co_3O_4 [3], Co_3O_4 nanoparticles with an average diameter of 10.9 nm prepared in said study were supported on SiO_2 spheres and incorporated in the present research.

In situ CO-PROX studies were conducted using the in house developed magnetometer [29,140] and PXRD cell [30,140]. The former gives direct evidence of the formation of metallic Co even in trace amounts and, due to the larger catalyst volume, was also used to collect activity and selectivity data. PXRD studies give insight in the composition of crystalline phases within the instrument specific detection limit. As the support material is amorphous and cannot directly be quantified with X-ray diffraction based techniques, extracted quantitative data focuses on the phase changes within the Co-containing species. Due to the small loading and the high amorphous background of the SiO_2 spheres, the quantitative data suffers from a low signal to noise ratio and should be regarded as trend rather than absolute concentration.

5.3.1 *In situ* study of Co_3O_4 N-nanoparticles

The PXRD diffraction patterns collected under reaction conditions display, as expected from offline analysis (see section 5.2.1), a pure Co_3O_4 phase on the amorphous SiO_2 support at 50°C (figure 5.10 A: 2Θ range showing SiO_2 amorphous contribution omitted for clarity). Qualitative and quantitative analysis confirms the absence of a reduction process up to temperatures of 200°C (figure 5.10 A & B), although the peak intensity of the Co_3O_4 diffraction lines is decreasing. It has to be noted though that laboratory scale PXRD is limited in its resolution both regarding crystallite size or in the present study potential shell thickness and phase concentration. The lack of a magnetic signal (figure 5.10 D) below 200°C confirms the absence of metallic Co^0. The CO conversion to CO_2 steadily increases with increasing temperature reaching a maximum conversion of 90.7% at 175°C (figure 5.10 C), with a H_2 and O_2 conversion of 2.66 and 93.3% respectively (feed gas volumetric ratios of CO:H_2 is 1:53 balance N_2). This indicates that even at these low temperatures and maximum CO oxidation activity, excess oxygen is nearly quantitatively converted to water at the expense of hydrogen. Upon reaching 200°C, a relatively rapid decrease in Co_3O_4 concentration in favour of CoO can be observed. In parallel, the CO conversion and CO_2 concentration in the reactor outlet flow decrease. The oxygen not bound by the oxidation of CO is fully consumed by hydrogen oxidation (H_2 conversion at 3.07%). Metallic Co is first detected at 250°C in the diffraction patterns accompanied by formation of CH_4. Co^0 is the dominant phase at a temperature of 300°C and the only detectable phase at a temperature of 450°C and throughout the cooling stages.

The magnetic readings first evidence the presence of metallic Co^0 during the ramping stage from 225 to 250°C (note that magnetic readings were taken throughout the experiment including the temperature ramps while PXRD diffraction patterns were only collected during the temperature holding stages). The degree of reduction gradually increases with time and temperature reaching a maximum of 79% at 450°C. Interestingly, upon cooling the degree of reduction is reduced at temperatures below 200°C reaching a stable 71% at 200-175°C. This has to be the result of a partial oxidation due to the presence of O_2 in the gas phase possibly yielding a thin oxide shell. Based on the average crystallite size of the spent catalyst analysed with TEM (see figure 5.11), the decrease in degree of reduction can be associated with an oxide shell thickness of 0.46 nm assuming CoO. This supports the apparent absence of a re-oxidation event in the XRD experiment. While re-oxidation was also described by Nyathi [3], it was observed at temperatures as high as 250°C. In parallel to the appearance of metallic Co, the catalyst selectivity changes dramatically. CO_2 formation is reduced to nil at 350°C, while the CO conversion increases to 100% yielding purely CH_4. O_2 is fully consumed by hydrogen oxidation. In fact, at temperatures above 200°C, the O_2 conversion is, independently of CO conversion and CO_2 formation, 100% indicating a strong competitive hydrogen oxidation reaction (see figure 5.12). Even at full CO conversion and 100% selectivity of CO to CO_2, i.e. in the absence of the methanation reaction, the O_2 conversion should not surpass 50% in the absence of H_2 oxidation. The catalytic and phase behaviour of the nanoparticles supported on SiO_2 is very comparable to the same particles supported on γ-Al_2O_3 as reported by Nyathi [3] up to the maximum temperature applied in said study of 350°C. Interestingly the methane formation seems to decrease slightly in the temperature range of 400 to 450°C. This can possibly be associated with a loss in surface area due to sintering of the cobalt crystallites reducing the available surface area. TEM analysis of the spent catalyst (see figure 5.11) confirm the crystallite growth with a median size of 10.2 nm in the fresh catalyst to 13.1 nm in the spent catalyst (average crystallite size of 10.9 ± 1.89 nm in the fresh catalyst to 13.2 ± 3.36 nm) after catalytic testing. This size increase relates to a loss in surface area of approximately 17.3%. Nyathi [3] did not observe any significant crystallite growth in his experiments. In parallel to the decrease in conversion, the concentration of CH_4 and CO_2 decreases and increases respectively. Upon lowering of the reaction temperature, CH_4 formation steadily decreases reaching 0% in the reactor outlet gas stream at 175°C while the CO_2 formation passes through two distinct maxima at 275°C

(28.5% in reactor outlet gas) and 175°C (19.1% in reactor outlet gas) without ever achieving the catalytic performance displayed during the heating stages.

During the higher temperature maximum, no phase change of the catalyst is observed, i.e. it has to be assumed that the catalyst has not changed during the cooling from 450°C. The low temperature maximum is observed during the partial re-oxidation of the catalyst (see figure 5.10 D). Two distinct maxima in CO_2 formation coupled with potentially different catalytic surfaces indicate a change in formation mechanism, possibly from the water gas shift (WGS) reaction to CO-PROX. Due to their similarity in overall CO consumption, the origin of CO_2 cannot be determined conclusively by the outlet gas analysis. However, it can be hypothesized that the WGS reaction is preferred on the metallic surface and through the exothermic nature of the reaction (ΔH_R= -41.27 kJ/mole) increases in rate with decreasing temperature, while on the partially re-oxidized surface the CO-PROX takes over in forming CO_2. Nyathi, [3] heating the alumina supported catalyst samples to 350°C only, observed a mirror image catalytic performance upon cooling from the maximum temperature with re-oxidation setting in at approximately 250°C. As these observations were crystallite size independent, in the studied size range from 3.7 to 13.8 nm, it is unlikely that the here observed strong deviation in catalytic performance during the heating and the cooling process is based solely on the temperature induced crystallite growth as evidenced by TEM (see figure 5.11). Moreover, it can be speculated that the higher degree of reduction 70% after treatment at 450°C versus 50% at 350°C results in the non-comparability of the catalytic performance during heating and cooling. The higher concentration of the metallic Co^0 species could also result in the observed lower temperature re-oxidation (200°C in the present study versus 250°C as reported by Nyathi [3]).

N-nanoparticles

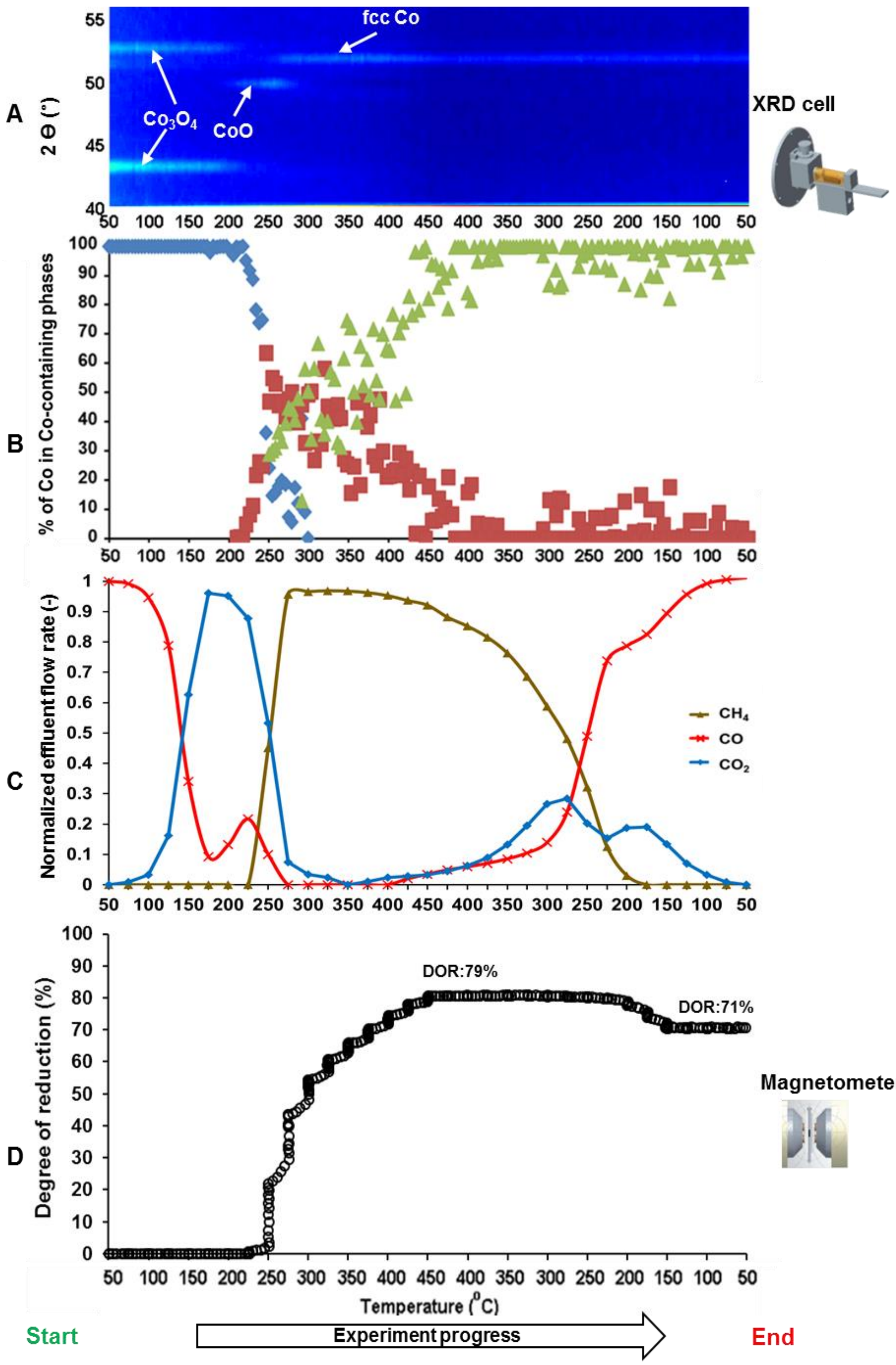

Figure 5.10: In situ PXRD scans and magnetometer degree of reduction for N-nanoparticles. A: in situ PXRD colour coded top view. B: % of Co in Co-containing phases. C: C-normalised effluent flow rate of CH_4, CO and CO_2. D: Degree of reduction measured by the magnetometer

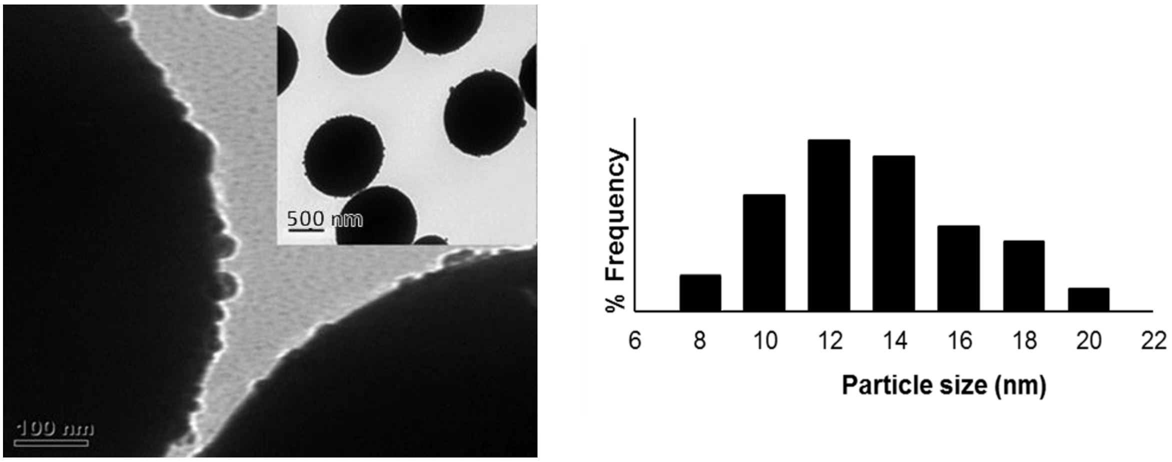

Figure 5.11: TEM micrographs and crystallite size distribution of spent Co_3O_4 N-nanoparticles

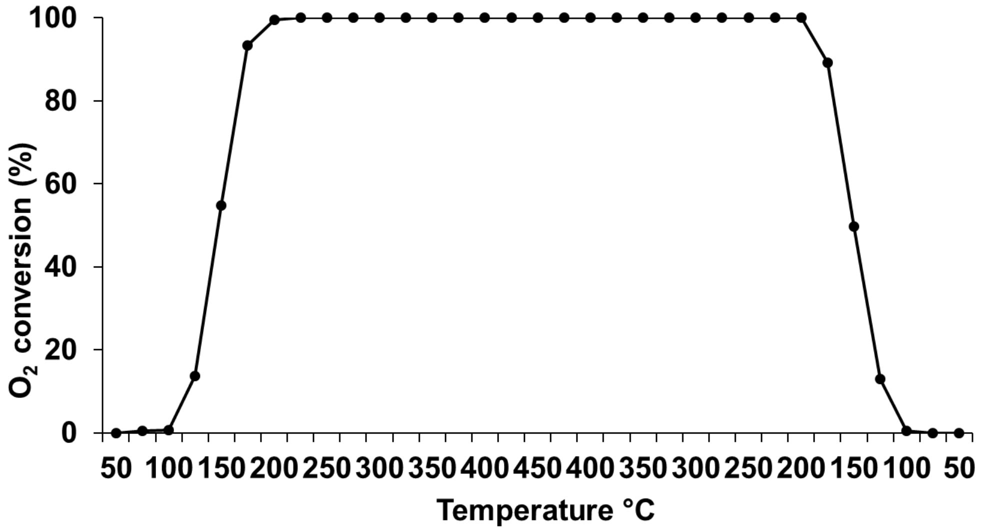

Figure 5.12: Oxygen conversion during CO-PROX over N-nanoparticles Co_3O_4/SiO_2 catalyst

Offline PXRD analysis of the spent sample offers a significantly higher resolution than the diffraction patterns collected *in situ*. A comparison with the fresh sample (see figure 5.13) confirms the reduction of Co_3O_4 to predominantly fcc Co^0. The stability of the metallic phase in an air atmosphere supports the hypothesis of the formation of an oxidic layer acting as passivation barrier [155]. Indeed, a diffraction line at 49.67° 2Θ, not detected in the *in situ* measurements, can be assigned to CoO. An additional shoulder at 49.3° 2Θ might indicate the presence of minor fractions of hcp Co^0 however the maximum intensity diffraction line reported for hcp Co at 55.7° 2Θ is not present. Nyathi [3] observed the same shoulder and was not able link it to any cobalt phase.

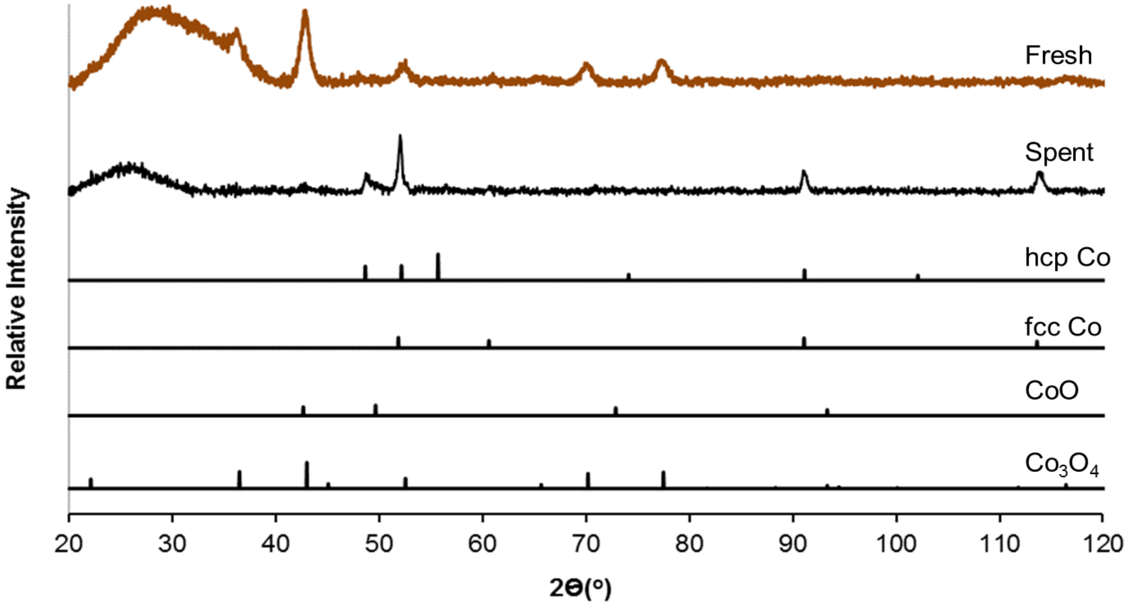

Figure 5.13: PXRD diffractograms of supported fresh and spent Co_3O_4 N-nanoparticles as well as relevant reference patterns

5.3.2 *In situ* study of Co_3O_4 nanocubes

The combined experimental results from *in situ* PXRD and magnetometer studies of the supported Co_3O_4 crystallites of cubic morphology are shown in figure 5.14 and 5.15. Direct comparison of the phase composition as function of time on stream and reaction conditions with the previously discussed N-nanoparticles shows a delayed reduction as already shown with TPR (see section 5.2.4). While PXRD detected the formation of CoO at temperatures of 200°C in case of the N-nanoparticles, the amine nanocubes undergo the first reduction step at temperature of 275°C and the HCl cubes at 250°C (figure 5.14 and 5.15 A and B). The reduction to metallic cobalt is similarly delayed with the amine nanocubes showing the formation of Co^0 first at 300°C and the HCl cubes at 275°C (as measured by the magnetometer, (figure 5.14 and 5.15 D) compared to the 225-250°C in case of the N-nanoparticles (see figure 5.10 D). The trend observed during TPR, namely that the reduction of the HCl nanocubes is suppressed compared to the amine nanocubes is therefore not confirmed under PROX conditions. Although the achieved maximum degrees of reduction are similar, 80% for the amine nanocubes and 77% for the HCl naocubes in comparison to the 79% for the N-nanoparticles (all at 450°C), the reduction process differs significantly. As indicated in the H_2-TPR measurements (see section 5.2.4) the main reduction events of the cubic Co_3O_4 recorded by the magnetometer are at 375-400°C, i.e. 75-100°C above the initial formation of metallic cobalt. N-nanoparticles undergo the dominant reduction directly upon formation of a Co^0 seed at 250 and 300°C. Interestingly the *in situ* PXRD diffraction patterns of the cubic morphologies display clear diffraction lines of CoO throughout the experiment and the Rietveld refinement based pattern analysis yield a concentration of CoO in the cobalt containing phases of 30-40% which correlates well with the magnetometer based degrees of reduction. It is noted that the diffraction patterns of the N-nanoparticles show no cobalt bearing phases besides fcc Co^0 beyond temperatures of 425°C. It can be assumed that the relatively small Co_3O_4 crystallites on the N-nanoparticles (average crystallite size diameter of 10.9 ± 1.89 nm in the fresh catalyst to 13.2 ± 3.36 nm in the spent catalyst) either result in small CoO cores and a metallic shell with the core being under the detection limit of the experimental set-up, or the expected 30% oxidic Co^0 (translating to an absolute amount of 1.35 wt.-% based on AAS and ICP loading measurements) is at the given crystallite size below the detection limit. As previously observed by Nyathi [3] and in the present study in the case of the N-nanoparticles, upon cooling the degree of reduction was reduced, i.e. a re-oxidation took place at 200-175°C from 80 to 72% for the amine nanocubes and at 150-125°C from 77 to 71% in case of the HCl nanocubes which represents a relative loss of 13-15%. The quantitative analysis of the PXRD diffraction patterns, although it displays a large variance due to the low diffraction line intensity and prominent background of the amorphous SiO_2 carrier, seems to confirm the re-oxidation and suggest the formation of CoO, not Co_3O_4. Similar re-oxidation events are reported in literature for passivation processes [155]. It has to be noted that the re-oxidation of the metallic Co^0 component coincides with the detection of O_2 in the reactor outlet gas, i.e. the decrease of the O_2 conversion from 100% (see figure 5.16).

Similar to the delayed reduction process, the CO oxidation over the cubic Co_3O_4 morphologies requires higher temperatures compared to the N-nanoparticles. While in the latter case CO_2 is formed at temperature as low as 100°C, temperatures of 125 and 175°C are required in the case of the HCl and amine nanocubes respectively (figure 5.14 and 5.15 C). Due to the later reduction to CoO, the CO oxidation peaks at 250°C with a CO conversion of 67.3% while the maximum CO conversion based purely on oxidation is achieved at 225°C with 58.4%. Comparing both nanocube based catalyst at the same reaction temperature, namely 225°C shows a very comparable conversion of 59.0% and 57.9%. With a further increase in temperature and paralleled by the reduction to CoO, both the concentration of CO_2 in the reactor effluent as well as the CO conversion decrease. At the same time the O_2 conversion, which increased in parallel to the initial CO_2 formation, reaches conversion levels of 100% indicating the strong competitive reaction of hydrogen oxidation. Nominally, at 100% CO_2 selectivity, the O_2 conversion should not surpass 50% as O_2 is available in a twofold excess in the reaction gas mixture. Indeed, the O_2 conversion remains at 100% until reaching the previously mentioned 175°C and 150°C during cooling for the amine and HCl nanocubes respectively. Both catalysts show methanation activity from 325°C onwards, reaching a maximum at 450°C. Although at this stage all converted CO (CO conversions of 95.5% and 98.1% at 450°C for amine and HCl nanocubes respectively) yield methane, the O_2 conversion is not affected, an indication that hydrogen oxidation can be catalysed on the Co_3O_4, CoO as well as the metallic Co^0 surface at high enough temperatures [156].

A subsequent lowering of the reaction temperature results in a decrease in CO conversion, a decrease in CH_4 concentration and an increase in CO_2 concentration in the reactor outlet gas. Both model catalyst show, similarly to the previously described N-nanoparticles two distinct maxima in CO_2 formation (at 300 and 175°C for the amine nanocubes and at 275 and 75°C for the HCl nanocubes). Again the high temperature maximum cannot be correlated to any phase change, while the low temperature maximum correlates well with the observed re-oxidation. As proposed for the N-nanoparticles this indicates a change of mechanism in CO_2 formation from potentially the Co^0 catalysed water-gas shift reaction to the oxide, assuming Co^{3+} surface species become available upon re-oxidation, catalysed CO oxidation. The main difference in catalytic performance between the two types of cubes seems to be their tendency to undergo reduction.

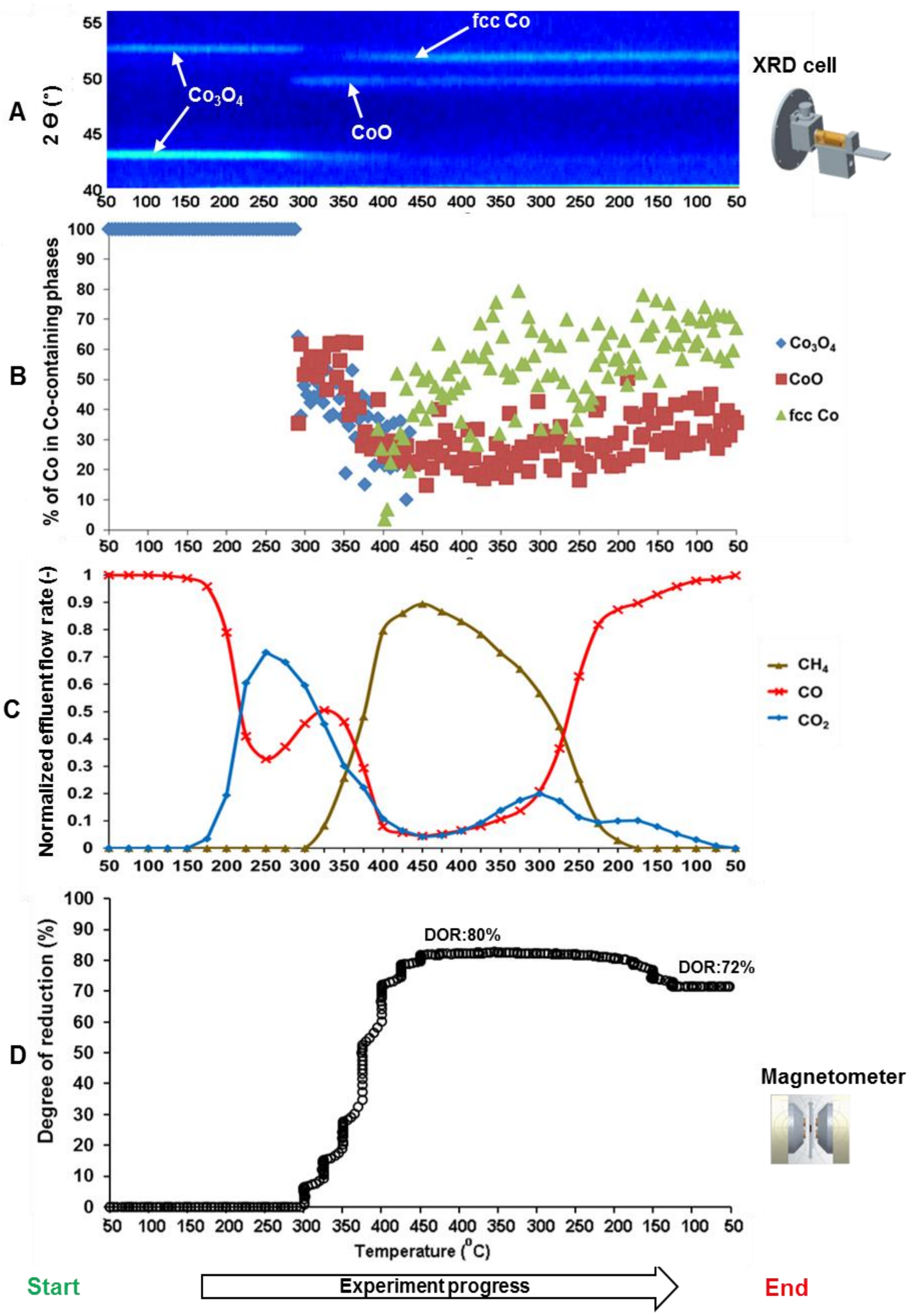

Amine nanocubes

Figure 5.14: In situ PXRD scans and magnetometer degree of reduction for amine nanocubes. A: in situ PXRD colour coded top view. B: % of Co in Co-containing phases. C: C-normalised effluent flow rate of CH_4, CO and CO_2. D: Degree of reduction measured by the magnetometer

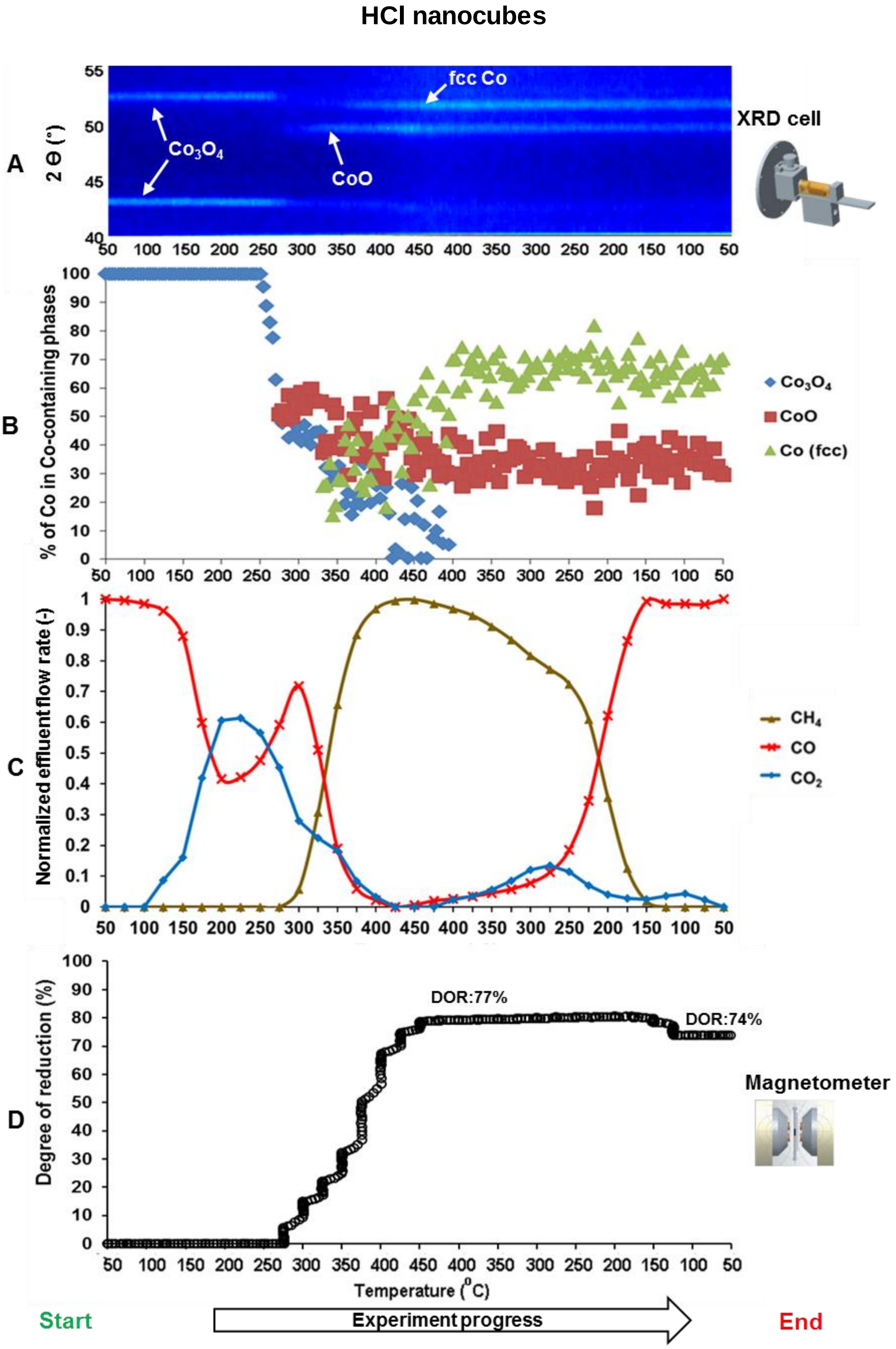

Figure 5.15: In situ PXRD scans and magnetometer degree of reduction for HCl nanocubes. A: n situ PXRD colour coded top view. B: % of Co in Co-containing phases. C: C-normalised effluent flow rate of CH_4, CO and CO_2. D: Degree of reduction measured by the magnetometer

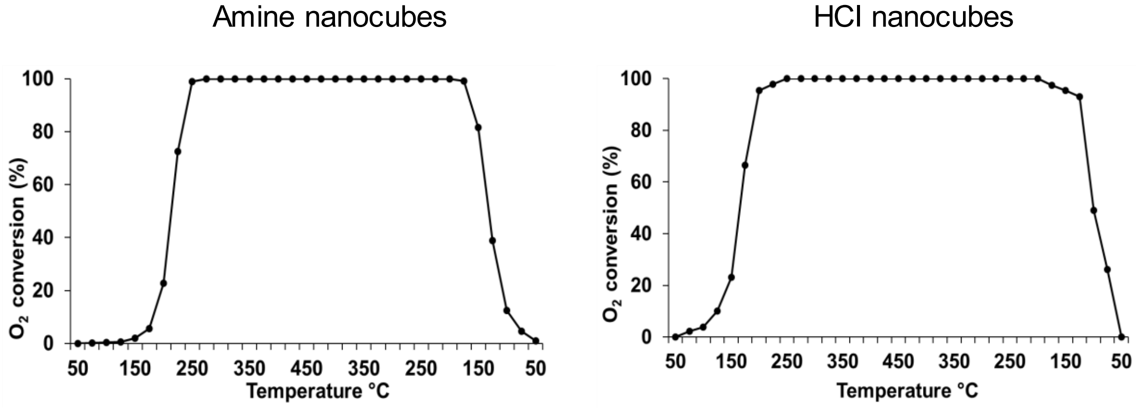
Amine nanocubes

HCl nanocubes

Figure 5.16: Oxygen conversion as a function of reaction temperature over amine and HCl nanocubes Co_3O_4/SiO_2 catalyst

TEM analysis of the spent supported nanocubes shows that the crystallites did not retain their cubic morphology over the course of the experiment (see figure 5.17) while no sintering but rather a decrease in size is observed (comparing edge length to diameter, see table 5.4), the crystallites appear to have adopted a spherical shape.

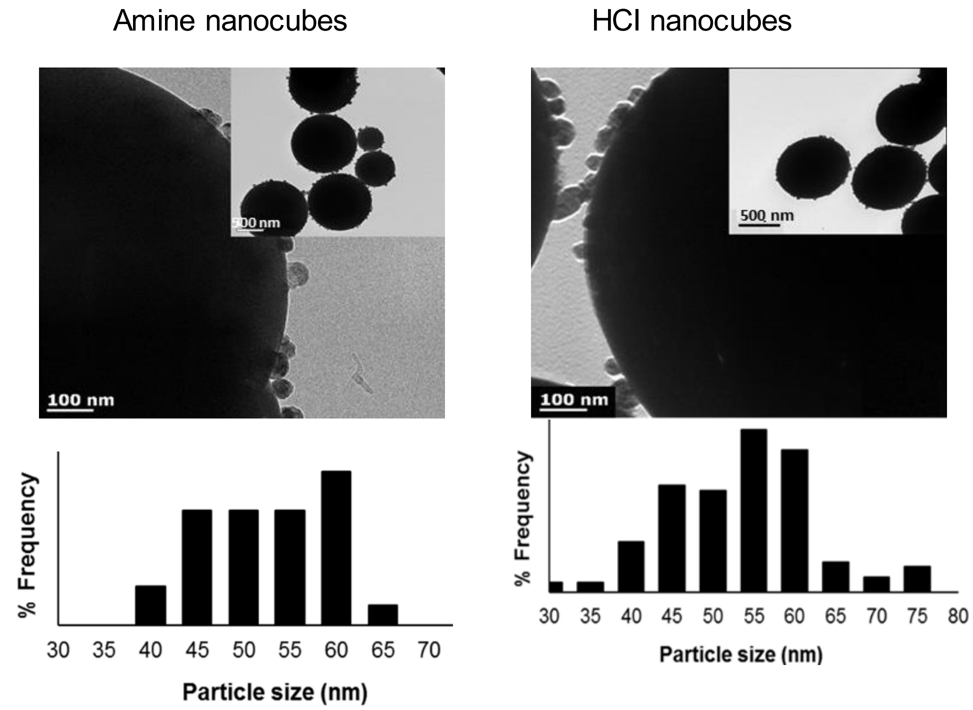
Amine nanocubes

HCl nanocubes

Figure 5.17: TEM micrographs of spent Co_3O_4 nanocubes

In an effort to understand at which stage of the experiment the observed chanage in morphology takes place, a fresh SiO_2 supported amine nanocube sample was treated under the same reaction conditions described earlier up to a temperature of 275°C. This temperature correlates to the onset of the first reduction step from Co_3O_4 to CoO. After 1 hour on stream, the catalyst sample was cooled to room temperature under argon and extracted from the reactor. TEM analysis (see figure 5.18) clearly confirmed the presence of cubic crystallites. The average edge length was reduced from 52.4 ± 4.33 nm for the fresh sample to 38.6 ± 6.89 nm. It is however not clear if the loss in morphology (see figure 5.17) can be attributed to the reduction of CoO to metallic cobalt or to an extended exposure of the metallic cobalt particles to reaction gases. The loss of morphology is accompanied by crystallite growth through sintering (edge length CoO cubes 38.6 nm vs diameter of spent sample 50.1 nm).

Table 5.4: Average crystallite size of supported nanoparticles as determined from TEM

Sample	**Fresh (nm)**	**Spent (nm)**
Amine nanocubes	52.4 ± 4.33	50.1± 7.08
HCl nanocubes	55.2 ± 5.1	51.7± 10.4

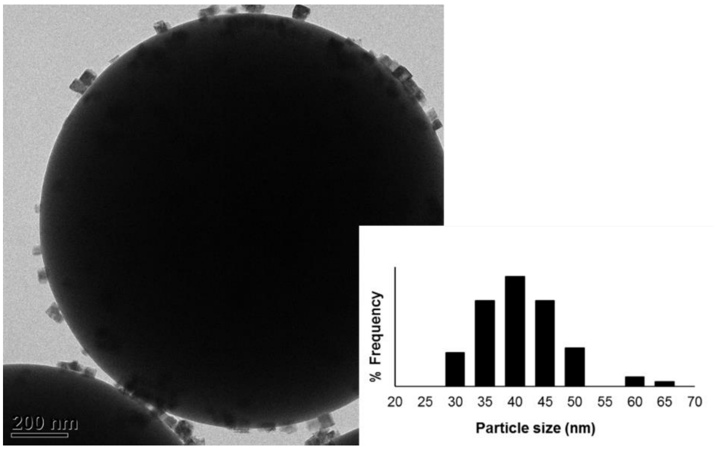

Figure 5.18: TEM micrograph and size distribution of amine nanocubes reduced to CoO

Offline PXRD patterns of the spent nanocube based catalysts were collected (see figure 5.19) as during the *in situ* application, diffraction resolution has to be balanced with temporal resolution. Both spent samples contain both CoO and fcc cobalt metal confirming the partial reduction and re-oxidation observed during the *in situ* experiments. An additional shoulder at 49.3° 2Θ which cannot be attributed to any cobalt phase is again observed for both samples.

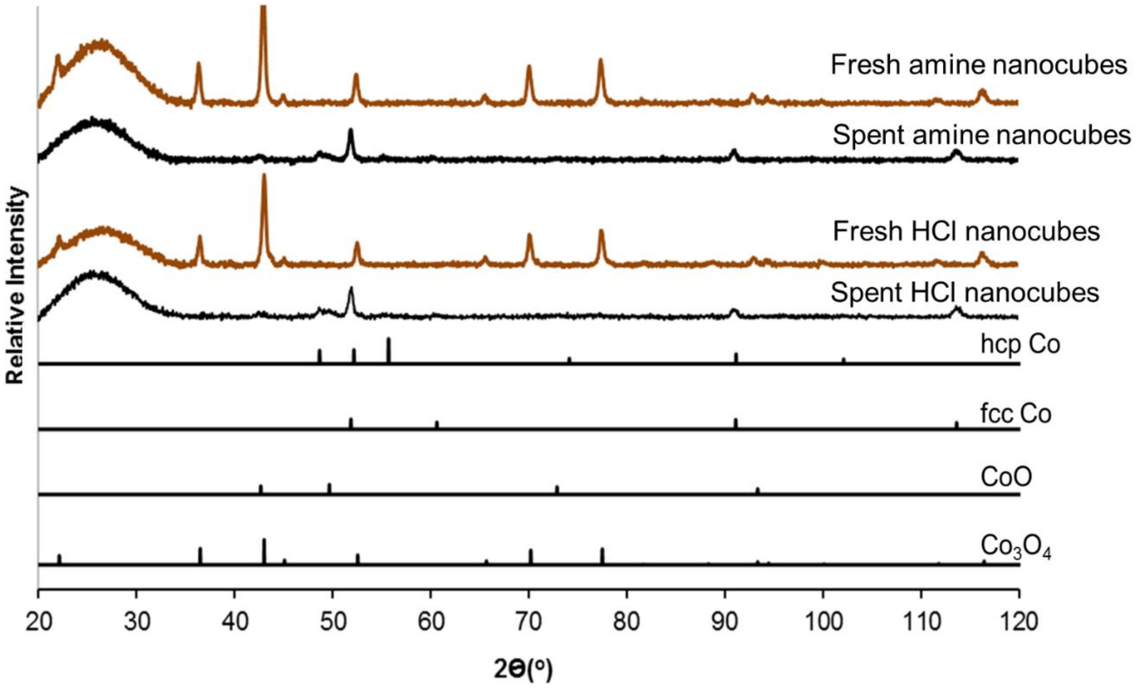

Figure 5.19: PXRD diffractograms of supported fresh and spent Co_3O_4 nanocubes

5.3.3 *In situ* study of Co_3O_4 nanosheets

Supported Co_3O_4 crystallites of sheet/platelet-like morphology were also exposed to CO-PROX conditions in the *in situ* PXRD capillary cell and magnetometer to evaluate their catalytic activity phase stability with the cumulative results shown in figure 5.20 and 5.21. Similar to the TPR results (see section 5.2.4), both types of sheets show similar reduction onsets under CO-PROX conditions. CoO is first observed via XRD at 225 and 250°C with metallic cobalt forming shortly after at 250 and 275°C in case of the amine and NaOH sheets respectively. These temperatures are very comparable to the reduction onset temperatures of the N-nanoparticles (see figure 5.10) which could be explained by the similarity in size of the N-nanoparticles and the crystallites comprising the sheets (see figure 5.2 and table 5.1). However, it has to be noted that the reduction onset temperatures during TPR experiments were found to be significantly lower for the N-nanoparticles compared to the sheets. Similarly, to the observation with regard to an enhanced or retarded reducibility of the HCl cubes, the TPR profiles clearly cannot be utilized to confidently predict deactivation/reduction of Co_3O_4 based PROX catalysts. The detection of CoO coincides with both the maximum CO_2 formation rate (with the amine nanosheets reaching higher CO_2 concentrations in the reactor effluent (67.3% vs 58.4%) as well as showing a higher initial activity evidenced through the lower temperature at the first observation of CO_2 (100 vs 150°C)) as well as with the O_2 conversion reaching 100% (see figure 5.22). The latter shows that again, besides CO-PROX, the catalysts support hydrogen oxidation and, above a certain temperature, this reaction scavenges the oxygen required for the Mars-van-Krevelen type surface re-oxidation subsequently leading to bulk reduction paralleled by deactivation for PROX.

The amine sheets in overall behave very similar to the N-nanoparticles. A maximum CO_2 formation is reached just before the first reduction to CoO is recorded. With the progression of the reduction, CO_2 concentration in the reactor outlet gas is reduced and CO conversion decreases, all at constant 100% O_2 conversion. Upon formation of metallic Co (fcc allotrope as shown by PXRD), the CO conversion rapidly increases at a high selectivity to CH_4. The methane concentration reaches a maximum below the maximum temperature (at 350°C) and below the maximum degree of reduction (at 50-60% vs 81% at 450°C). Increasing the temperature further results in a reduction in CO conversion and CH_4 yield, possibly associated to a loss in surface area through sintering. Upon cooling, the CO conversion as well as the methane concentration decrease with CO_2 concentration displaying two distinct maxima. The first at 300°C cannot be correlated to any phase changes and is proposed to be a result of WGS activity, while the low temperature maximum at 200 to 175°C is paralleled by a re-oxidation event decreasing the DOR from 81 to 77% (change only visible in the magnetometer as below signal threshold in PXRD) and could therefore possibly be assigned to regained cobalt oxide based CO-PROX activity.

The NaOH nanosheets show a very different behaviour to the other studied Co_3O_4 based model catalysts. The maximum CO_2 concentration in the reactor outlet gas measured just before the reduction to CoO is significantly lower than any other catalyst in this study, although the characterisation of the NaOH sheets did not hint on any significant differences to the amine sheets and even the N-nanoparticles regarding crystallite size and phase composition. Also with detection of metallic cobalt, methane formation is detected, but also to a significantly lower extend never constituting more than 60% of the reactor effluent gas at CO conversions below 80%. It is also noted that CO_2 concentrations remain high (15-20%) even at the maximum methane formation rate. Analysis of the XRD pattern reveal the difference in Co^0 allotrope with hcp being formed in the case of the NaOH sheets. In the Fischer-Tropsch synthesis, the metallic hcp cobalt phase is reported to show a higher activity compared to the fcc allotrope without significantly influencing the methanation rate [157] and is therefore unlikely to be the cause of the low methane concentration. In turn, discussing contaminants in hydro-processing units, sodium has been reported by Siegel & Olsen [158] to act as severe catalyst poison that can lower catalyst activity by about 40% at the level of 1.0 wt-% Na. EDX analysis of the NaOH nanosheets clearly shows the presence of residual Na on the catalyst (see table 5.5). The presence of sodium could potentially also explain the formation of the hcp Co^0 phase. The hexagonal Co^0 allotrope has been reported to form through reduction of Co_3O_4 in CO [159] or via the carburization of fcc Co^0 with carbon monoxide and subsequent decomposition [160]. While both processes are unexpected under the present high concentrations of hydrogen, the presence of an alkali ‘promoter’ could aid in the preferential adsorption of CO on the CoOx surface [161]. A maximum DOR of 92% is measured at 450°C, the highest in the present study. Upon cooling, a single maximum in CO_2 formation without measurable phase changes was observed at 300 to 275°C. Re-oxidation is only observed at 250 to 225°C reaching a stable DOR of 78% at 175°C.

Amine nanosheets

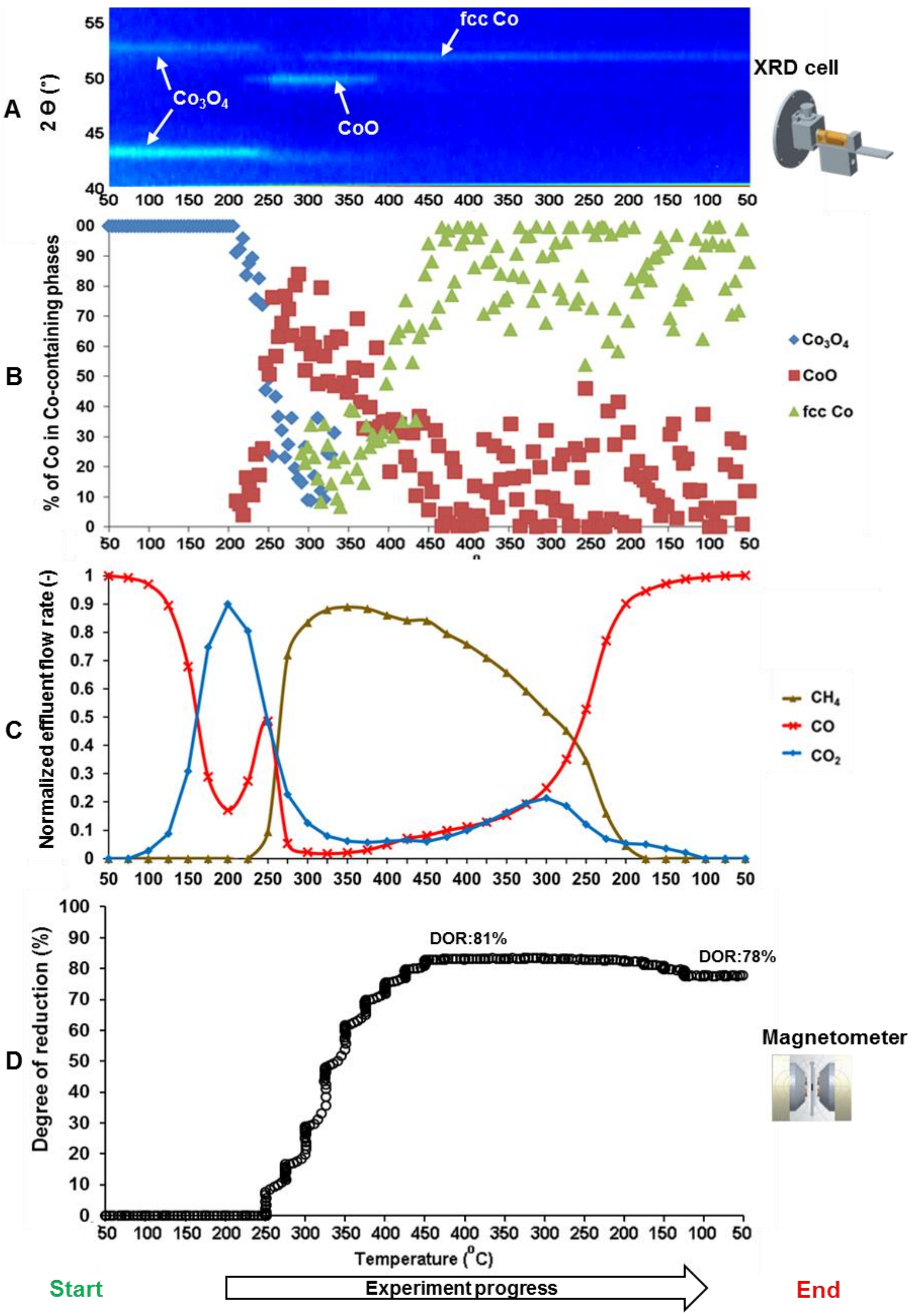

Figure 5.20: In situ PXRD scans and magnetometer degree of reduction for amine sheets. A: in situ PXRD colour coded top view. B: % of Co in Co-containing phases. C: C-normalised effluent flow rate of CH_4, CO and CO_2. D. Sample degree of reduction

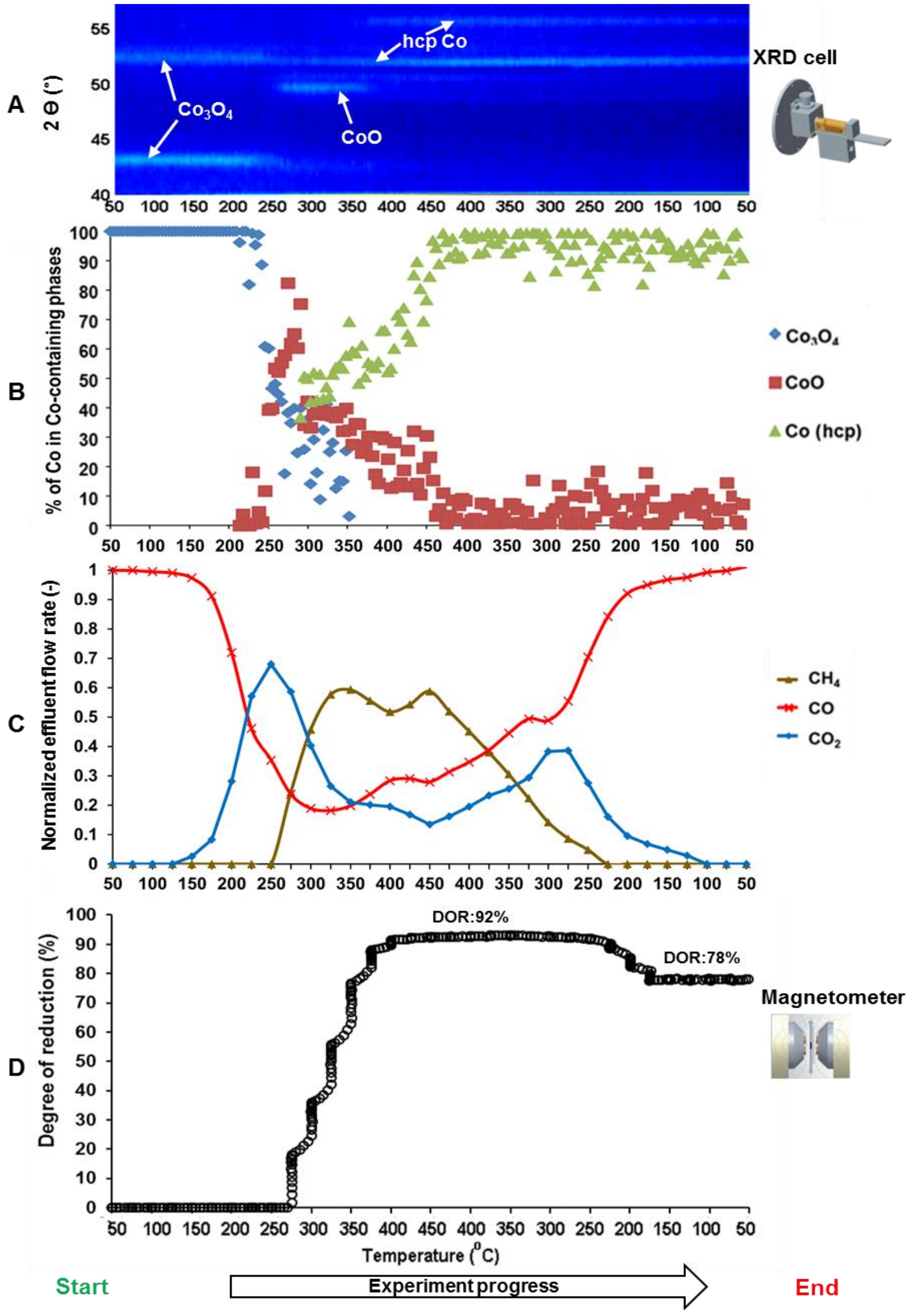

NaOH nanosheets

Figure 5.21: In situ PXRD scans and magnetometer degree of reduction for NaOH sheets. A: in situ PXRD colour coded top view. B: % of Co in Co-containing phases. C: C-normalised effluent flow rate of CH_4, CO and CO_2. D. Sample degree of reduction

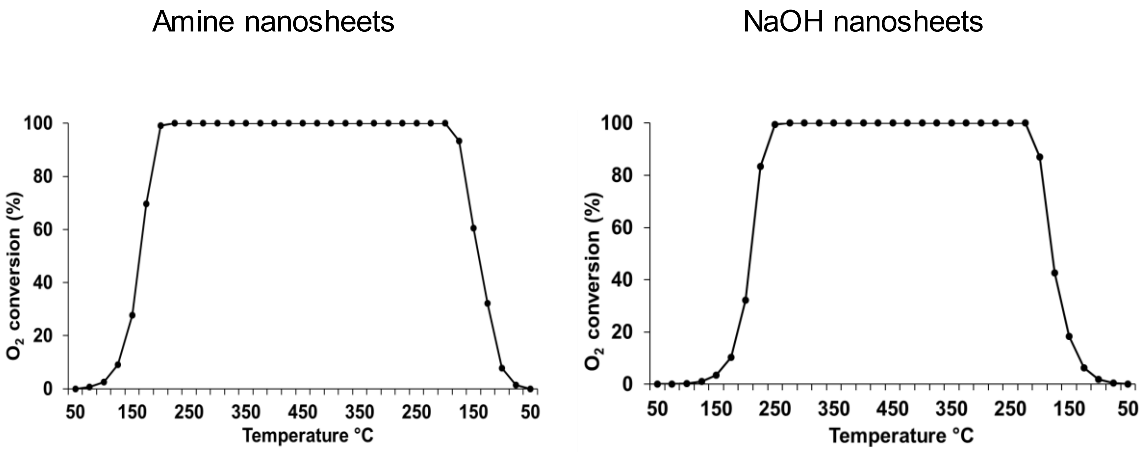
Amine nanosheets

NaOH nanosheets

Figure 5.22: Oxygen conversion as a function of reaction temperature over amine and NaOH nanosheets Co_3O_4/SiO_2 catalyst

Table 5.5: Unsupported NaOH nanosheets composition obtained using EDX spectroscopy

Element	**[wt.%]**	**[norm. wt.%]**	**[norm. at.%]**	**Error in %**
Oxygen	27.2	24.4	47.1	3.31
Silicon	0.83	0.74	0.82	0.07
Cobalt	75.5	67.6	35.4	2.04
Sodium	1.65	1.48	1.99	0.15
Carbon	6.38	5.71	14.7	0.91

Figure 5.23 shows TEM micrographs of spent amine and NaOH nanosheets samples. Comparison with the TEM images of the fresh samples clearly shows the collapse of the prepared sheets/platelets into particle agglomerates. To understand the process of the collapse, the amine nanosheets were reduced to CoO via treatment under the previously described CO-PROX conditions up to a temperature of 250°C. After one hour, the gas atmosphere was changed to argon and the sample was cooled to RT for analysis in TEM (see figure 5.23). Similar to the investigation of the nanocubes (see figure 5.18) the sheets seem to retain their morphology to an extent during the reduction to CoO.

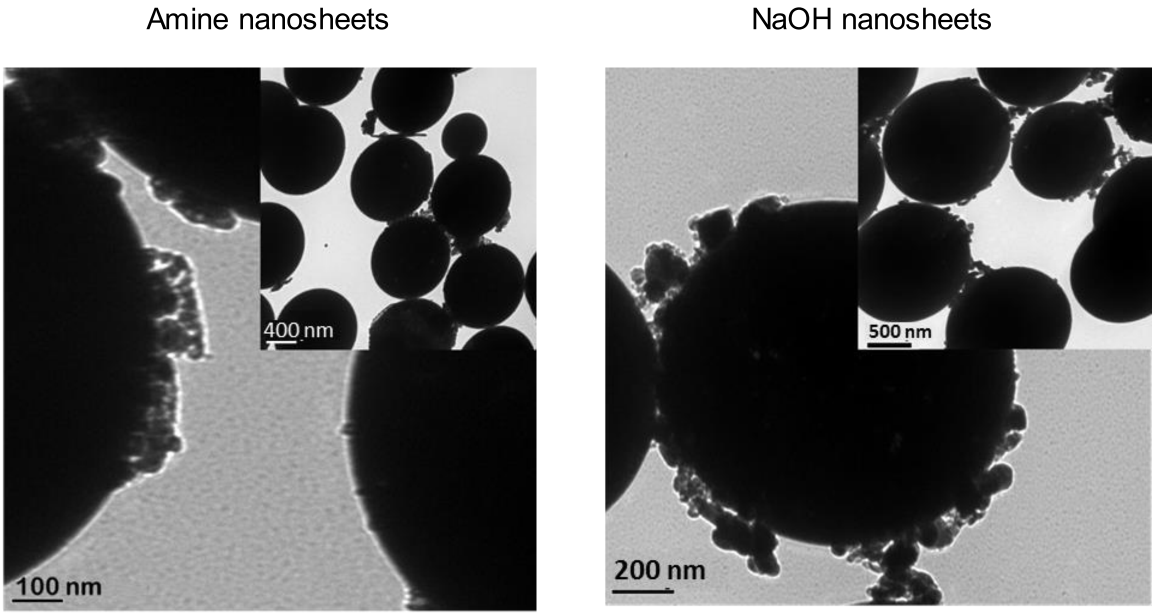

Figure 5.23: TEM micrographs of spent Co_3O_4 amine and NaOH nanosheets

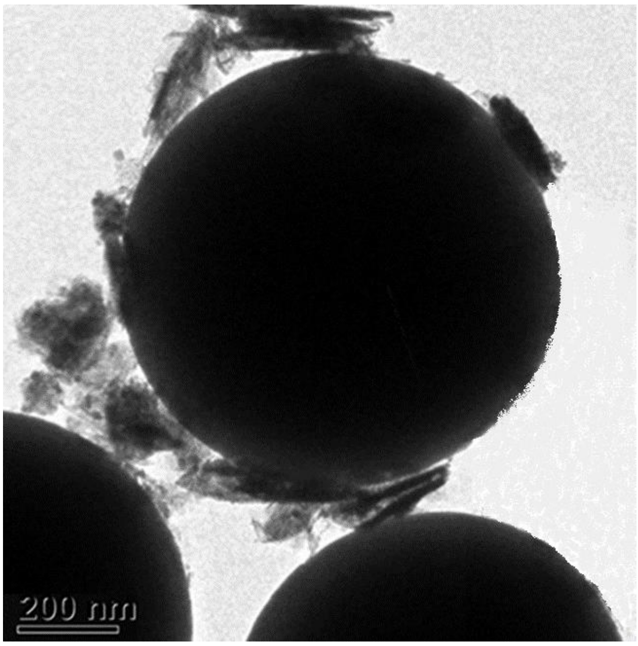

Figure 5.24:TEM micrograph obtained from TEM analysis of amine nanosheets reduced to CoO

Figure 5.25 contains the PXRD analysis of fresh and spent amine and NaOH nanosheets. From the standard diffraction peak positions of all phases of cobalt shown in the same figure, it can be seen that the fresh samples contained only Co_3O_4 phase. Amine nanosheets spent samples contained fcc Co while NaOH sheets peaks positions corresponded to the hcp Co.

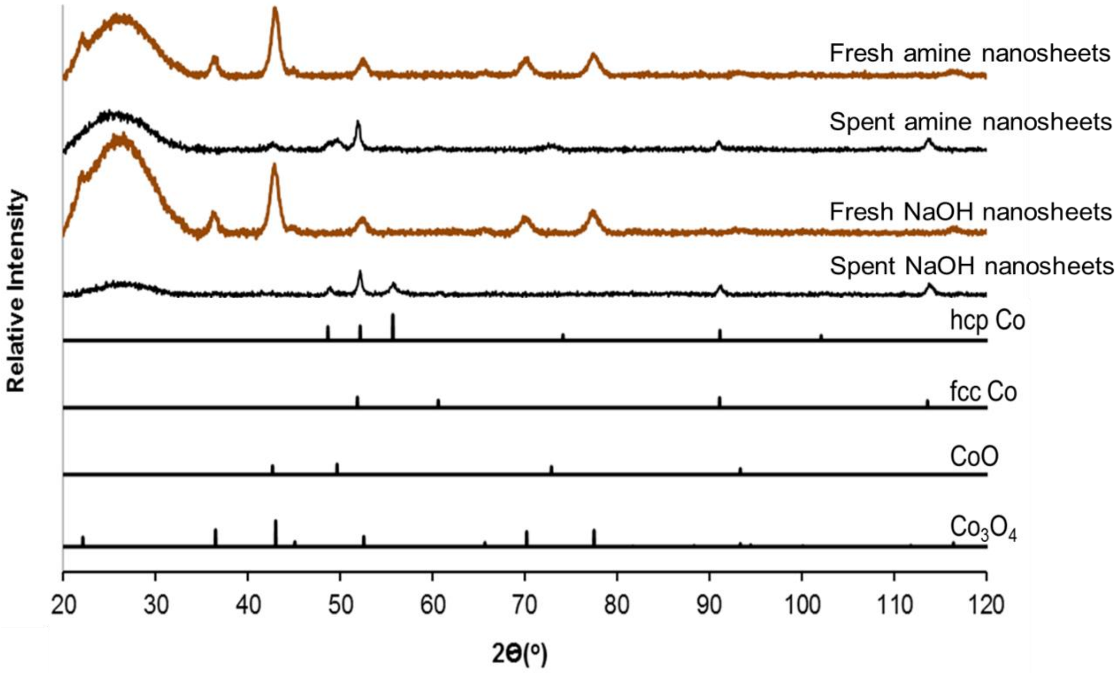

Figure 5.25: PXRD diffractograms of supported fresh and spent Co_3O_4 nanosheets

5.3.4 *In situ* study of Co_3O_4 nanobelts

The Co_3O_4 nanobelts mirror in their catalytic performance and phase transitions with the general trends observed and discussed in the present study in form of N-Nanoparticles, nanocubes as well as amine sheets. Compared to previous studies, we have not been able to synthesize single crystal belt like structures but rather superstructures constituted of small spherical shaped crystallites. Compared to the N-nanoparticles as well as the ‘building blocks’ of the nanosheets, the crystallites forming the belt structures are the smallest with an average diameter of 5-7 nm based on XRD and TEM techniques (see section 5.1.1 and 5.1.2). Nyathi et al. [3,162] observed for alumina supported Co_3O_4 crystallites of various sizes an increased difficulty to reduce the samples with decreasing crystallite size. In the present study we observe a similar trend in that while the reduction onset during TPR is similar for the nanobelts and the N-nanoparticles, the rate of reduction, especially of the second reduction event, is significantly lower.

During initial heat-up of the Co_3O_4 phase, an increase in CO_2 formation is noted up to a maximum concentration in the reactor outlet gas of 73.3% at 200 to 225°C. Over the same time, the O_2 conversion increases and reaches 100%. Subsequent temperature increase results first in the reduction to CoO paralleled by a decrease in CO_2 concentration and a decrease in conversion, followed by the reduction to metallic cobalt starting at 250°C. The formation of the metallic cobalt is rather slow at initial temperature settings, only increasing in rate at temperatures of over 400°C. Independently, maximum CO conversion (90.7%) and CH_4 yield is achieved at 375°C, at a relatively low DOR of 20 to 25%. Further increase in temperature again reduces the activity of the catalyst, most likely due to loss of surface area due to sintering events (see figure 5.28). Cooling from 450°C yields two CO_2 formation maxima, one peaking at 300°C under unchanged phase composition, i.e. at maximum DOR of 65%, and a second albeit much less pronounced one at 150°C paralleled by a re-oxidation event. As per our previous discussions in the present study we assign water gas shift activity to the high temperature peak and regained CO-PROX activity to the low temperature peak.

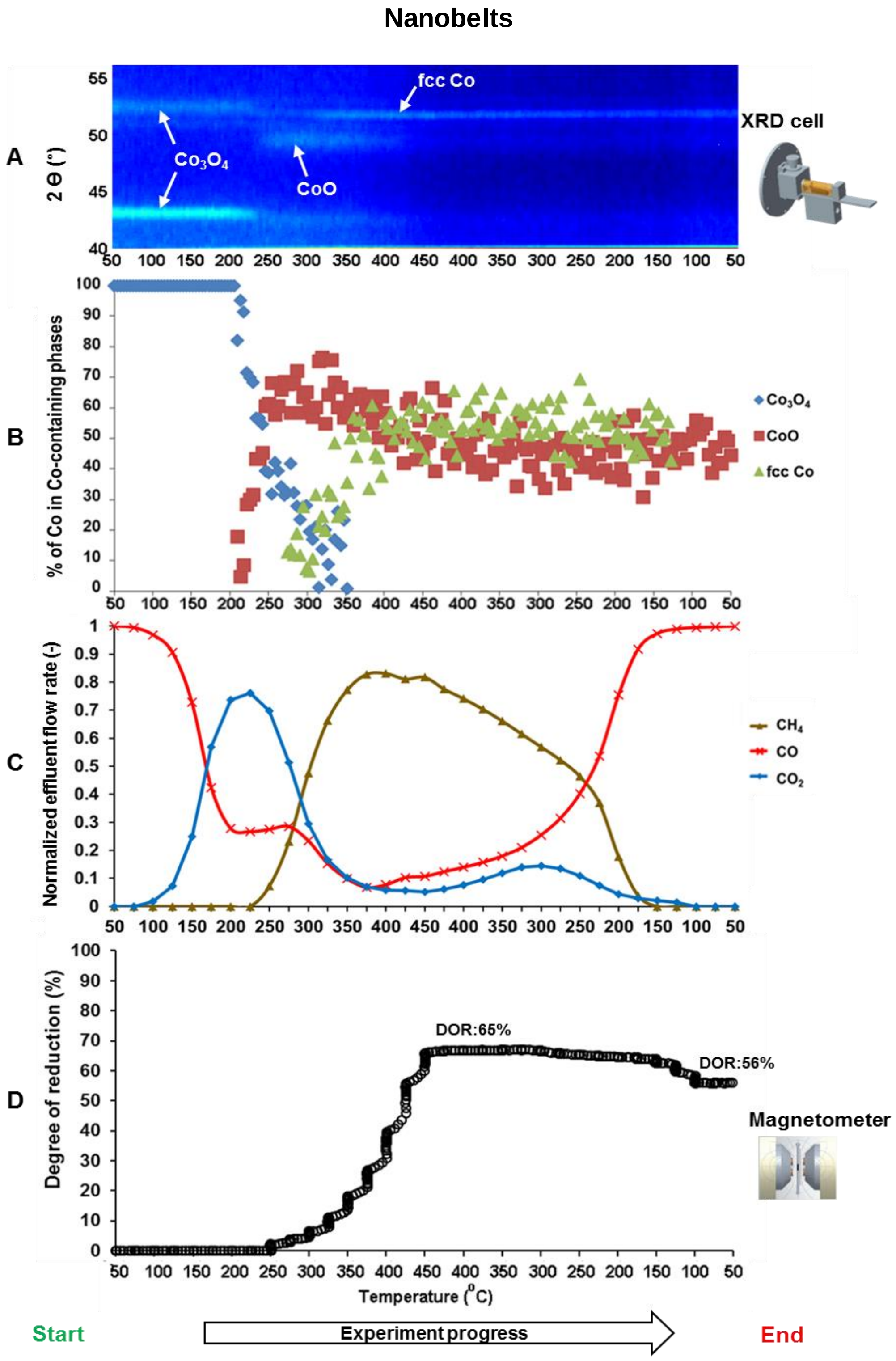

Figure 5.26: In situ PXRD scans and magnetometer degree of reduction for nanobelts. A: in situ PXRD colour coded top view. B: % of Co in Co-containing phases. C: C-normalised effluent flow rate of CH_4, CO and CO_2. D. Sample degree of reduction

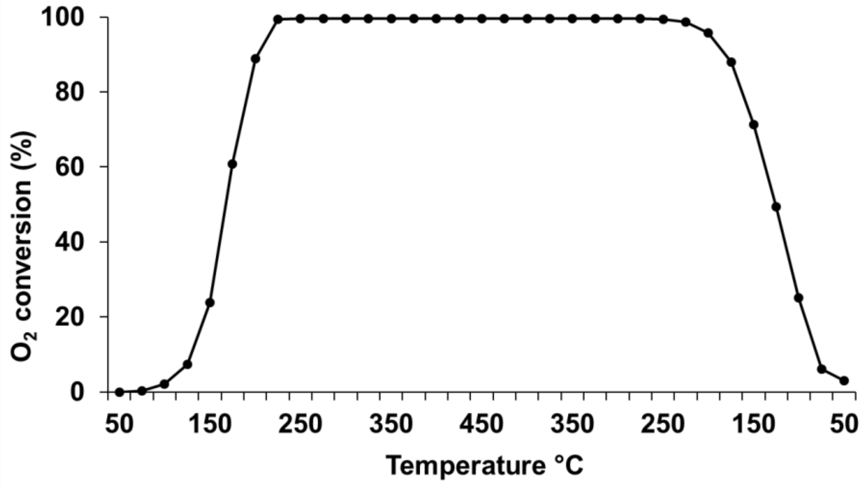

Figure 5.27: Oxygen conversion as a function of reaction temperature for Co_3O_4/SiO_2 nanobelts catalyst

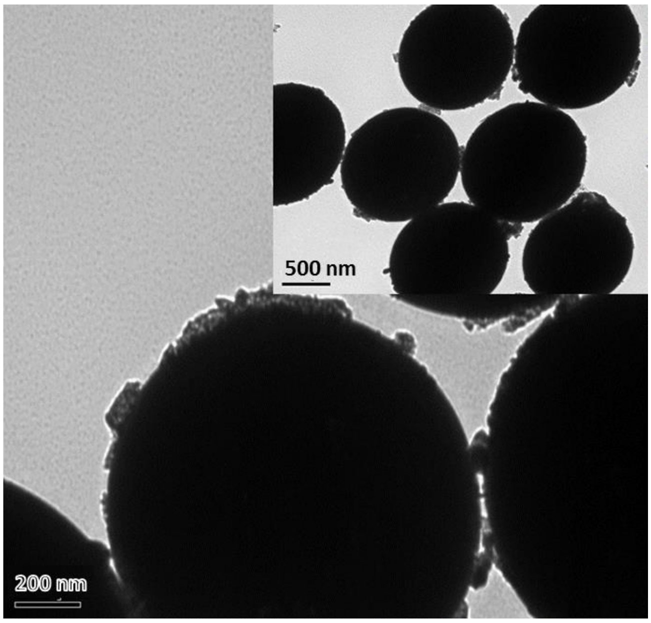

Figure 5.28: TEM micrographs of spent Co_3O_4 nanobelts

From TEM images of the spent nanobelt samples (see figure 5.28), it is clear that the nanobelts did not retain their morphology after coclusion of the experimental program either. The belt like morphology is broken up and aggregates around the silica spheres are observed. A size distribution could not be determined due to low contrast and lack of visible crystallite/particle boundaries in the agglomerates.

Just as the nanocubes and nanosheets the collapse of the morphology can to a large extend be associated to the reduction of CoO to metallic cobalt (see figure 5.29). The nanobelts were exposed to the same *in situ* experiment conditions and heating rate up to a temperature of 250°C.

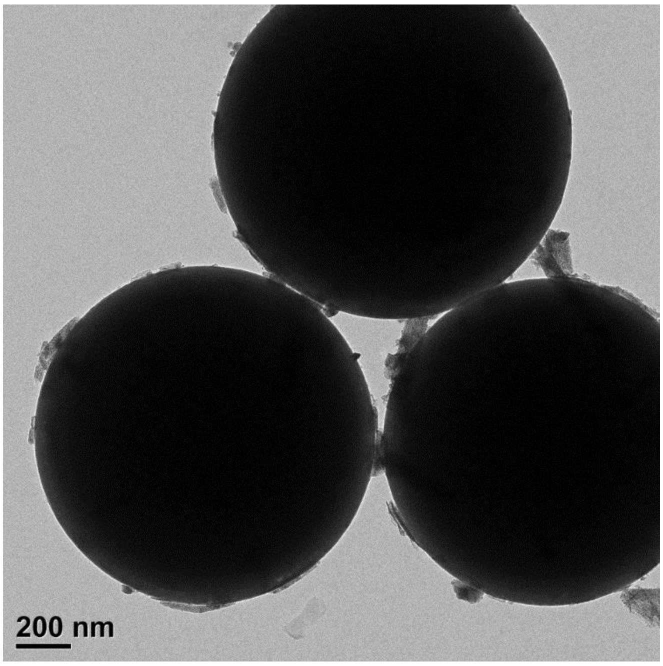

Figure 5.29: TEM micrograph and size distribution of nanobelts reduced to CoO

Due to the high resolution of offline PXRD analysis, a good comparison can be made between the fresh and spent supported nanobelts. The spent sample contain the diffraction patterns of both CoO and fcc Co^0. An additional shoulder that was observed in all other catalysts tested at 49.3° 2Ɵ can still be seen here.

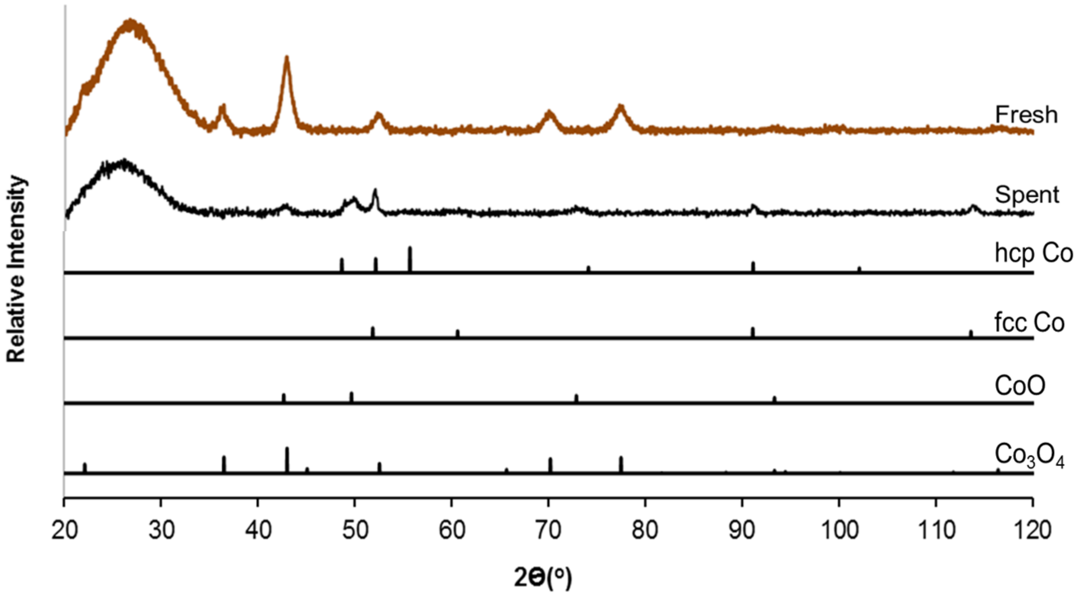

Figure 5.30: PXRD diffractograms of supported fresh and spent Co_3O_4 *nanobelts*

5.4 Summary

Figure 5.31 shows the comparison of magnetisation, degree of reduction as well as CH_4 and CO_2 yield of all catalysts investigated in the present study. The samples exhibit the same overall performance trends with varying reaction conditions. At low temperatures of 75-250°C, the CO-PROX reaction is supported. Absolute conversions and yields are hardly comparable due to the differences in mass specific surface area. With increasing temperature, the CO_2 yield decreases, in most cases in parallel with a decrease in CO conversion, which is associated to the formation of CoO. At the same stage, the O_2 conversion reaches 100%. Due to the over stoichiometric ratio of O_2 in the feed gas (O_2:CO =1), any O_2 conversion above 50% in case of 100% CO conversion and CO_2 yield, evidences the presence of the competitive and undesired H_2 oxidation (see figure 5.32). A further increase in temperature furthers the reduction process ultimately yielding fcc metallic cobalt but in the case of the NaOH nanosheets/platelets, hcp cobalt was identified in significant amounts. The degree of reduction increases in all cases up to the maximum temperature of 450°C. Formation of zero valent cobalt is directly correlated to the formation of methane on the expense of CO_2. At this stage, the CO-PROX reaction is competing on the one hand with the hydrogen oxidation for gaseous oxygen to re-oxidize the active sites in the Mars-van Krevelen type mechanism and on the other hand, with the methanation reaction for gaseous CO. A maximum CH_4 formation rate is not achieved at maximum DOR but at lower temperatures. In fact, an increase in temperature results in a loss of activity (CO conversion and as a result CH_4 yield) which is associated with a loss in surface area due to crystallite growth and structural changes. It is clearly shown that morphology changes are associated with the reduction process of CoO to metallic cobalt. Upon cooling from 450°C, CO conversion and CH_4 yield further decreases and for most catalysts, two distinct maxima in CO_2 concentration in the reactor outlet gas are recorded. The first maximum cannot be associated to a change in phase composition and is therefore hypothesized to be the result of water gas shift reaction, while the low temperature maximum is paralleled by a re-oxidation event of the cobalt phase and could therefore be based on regained CO-PROX activity. Unfortunately, due to the similar stoichiometrics of the different reaction pathways to CO_2, analysing the reactor outlet gas does not allow to differentiate between the reaction mechanisms.

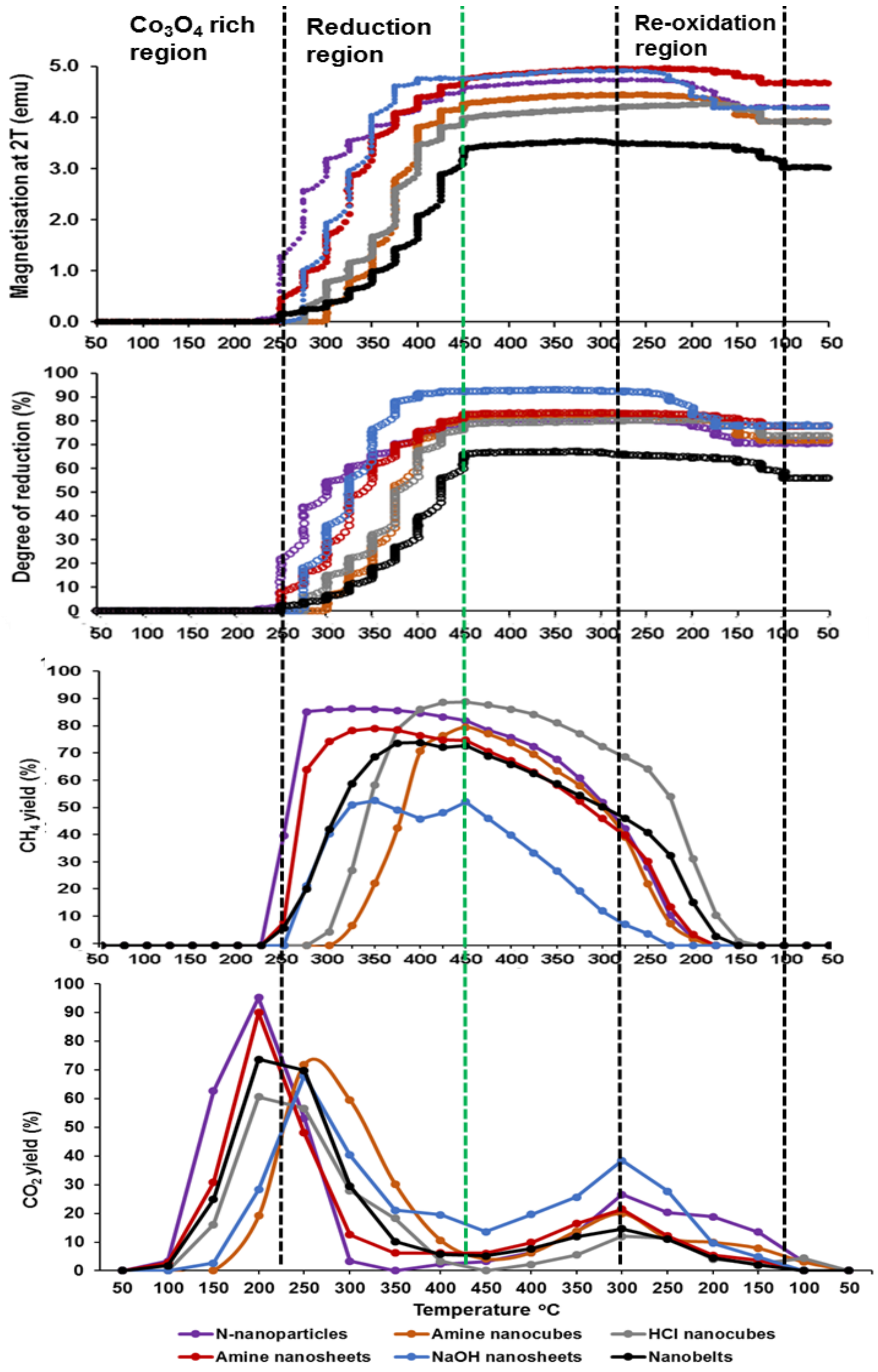

Figure 5.31: Magnetisation, degree of reduction, CH_4 yield and CO_2 yield as a function of temperature for N-nanoparticles, amine nanocubes, HCl nanocubes, amine sheets, NaOH nanosheets and nanobelts catalysts.

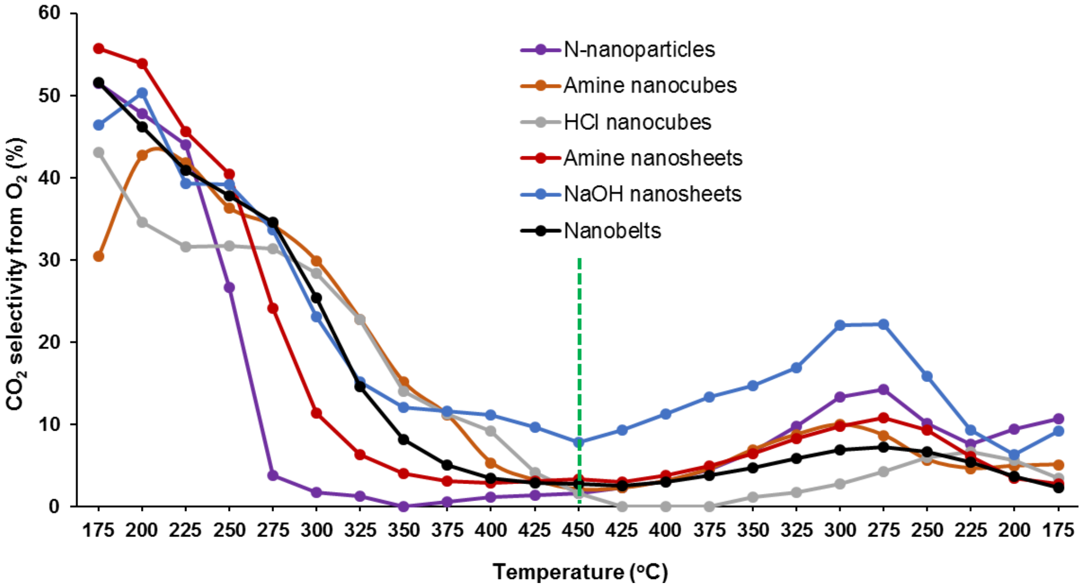

Figure 5.32: CO_2 selectivity based on the conversion of O_2 as a function of temperature for the N-nanoparticles, amine nanocubes, HCl nanocubes, amine sheets, NaOH nanosheets and nanobelts catalysts.

Figure 5.33 shows the mass specific conversion of the model catalysts for the CO oxidation reaction up to the temperature at which the reduction to CoO was observed with *in situ* PXRD. Due to the sensitivity limitations of the laboratory based X-ray diffractometer, the exact onset of the first reduction step from Co_3O_4 to CoO is possibly at slightly lower temperatures, explaining the observed loss in conversion at highest temperatures. Due to the significantly different mass specific surface areas of the prepared samples, the turn over frequencies are calculated as only true measure of comparison (see figure 5.34). It has to be noted that for the morphologies identified as superstructures via transmission electron microscopy analysis, i.e. the nanosheets and belts, the surface area of the constituting crystallites was selected for the calculation rather than the geometry of the superstructure. The nanosheets and nanobelts constituting crystallites have a calculated (based on the average crystallite sizes obtained from TEM) surface area of 60.8 m^2/g and 168 m^2/g respectively, with a corresponding experimental $S_{BET,\ nanosheets}$ = 68.5 m^2/g and $S_{BET,\ nanobelts}$ = 184 m^2/g. This confirms the presence of superstructures and furthermore that the constituting crystallites are nearly fully accessible for the catalytic reaction. A clear trend emerges, the similarly sized Co_3O_4 crystallites of the N-nanoparticles and constituting the amine nanosheets (10.9 ± 1.89 vs 13.6 ± 3.4 nm respectively) show a very similar TOF as a function of reaction temperature. The performance of the NaOH nanosheets, although also consisting of similar sized particles (8.7 ± 1.8 nm) is supressed, most likely by the residual sodium content (1.65 wt.-% on the surface as per EDX analysis). The nanobelts exhibit significantly smaller crystallites (5.1 ± 1.2 nm). As shown by the work of Nyathi et al [3,162], the TOF in the Co_3O_4 based CO-PROX is crystallite size dependent and shows a volcano type behaviour with a maximum in the rage of 8 to 9 nm. Although said maximum is measured at near full CO conversion, a more than twice as high TOF is reported versus a model catalyst exhibiting crystallites of an average size of 3.8 nm. The previously reported high activity of nanosheets and nanobelts in CO oxidation in absence of hydrogen linked to their high index crystal of {112} and {011} planes respectively [121] could not be confirmed as the present sheets and belts did not consist of single crystals exposing the respective crystal planes but rather of an agglomeration of near spherical particles without preferential planes as confirmed by the BET results. The prepared nanocubes differ in this regard. Consisting of single crystals or large crystalline domains, they clearly exhibit the preferential {001} planes. Their size in the present study was chosen so that the edge and corner sites should be negligible compared to terrace sites. Calculating the TOF, both the HCl and the amine cubes surpass the activity of all other catalyst by a factor of 3.5 to 4 (see figure 5.35). The low conversion (see figure 5.33, same mass loading for all catalysts) could potentially be overcome by reducing the size of the nanocubes as reported by Wolf et al. [155] . The authors describe a technique to prepare size controlled Co_3O_4 crystallites which are of cubic morphology at sizes around 5 nm. Compared to the nanocubes prepared in the present study, this would equate a reduction in edge length by a factor of 10 and would increase the surface area at the same Co_3O_4 loading by a factor of approximately 100. It has to be evaluated whether edge and corner sites start playing a significant role in this size range.

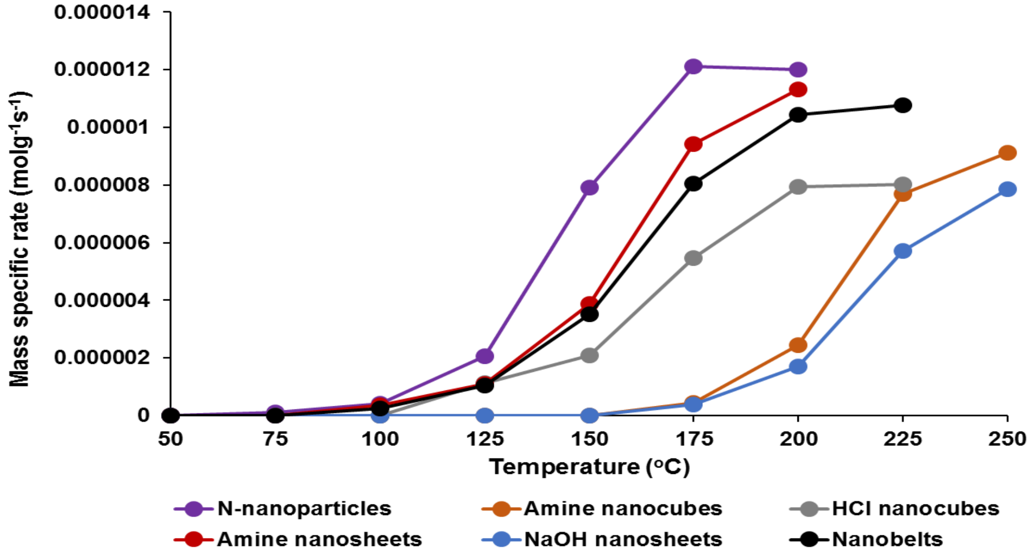

Figure 5.33: Mass specific rate of Co_3O_4 model catalyst as a function of temperature

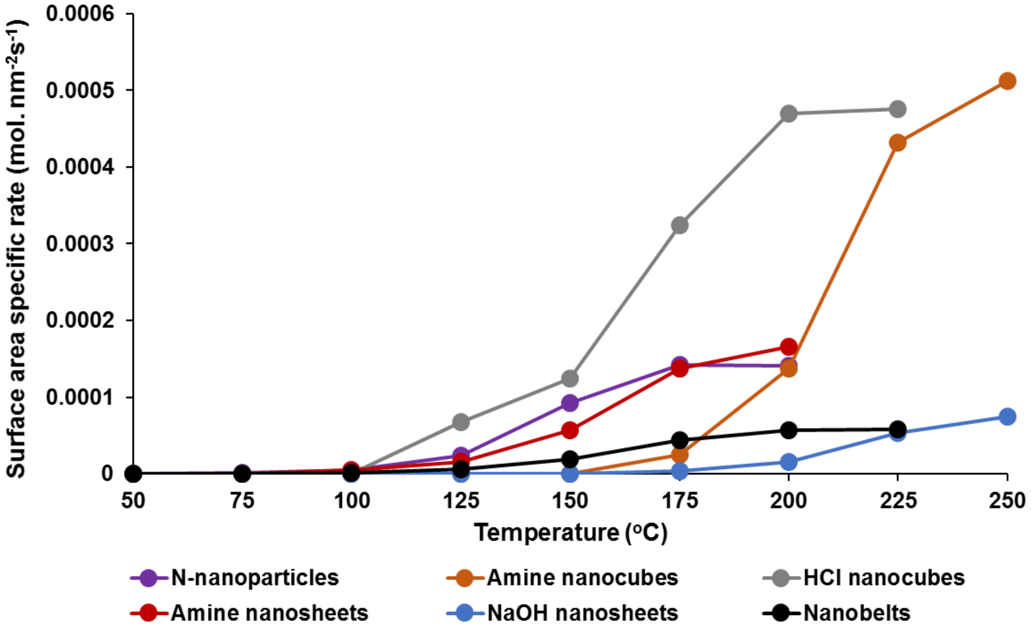

Figure 5.34: Surface area specific rate of Co_3O_4 model catalyst as a function of temperature

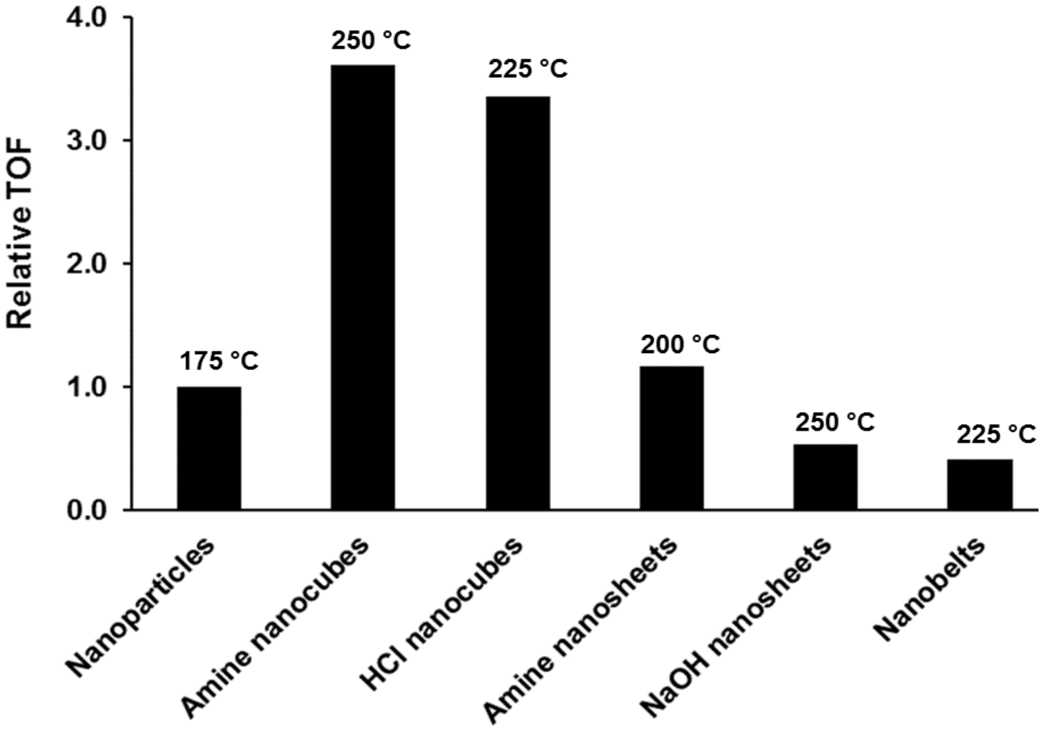

Figure 5.35: Relative turnover frequency as normalised to N-nanoparticles

6 Conclusions

The hydrothermal and precipitation based techniques were used to synthesise Stöber spheres (SiO_2) and different morphologies of Co_3O_4 nanoparticles. The nanoparticles did not show any change in size or morphology after calcination and supporting processes. The catalysts were supported on prepared Stöber spheres to get a model catalyst with a targeted loading of 5 wt.-%.

Both the unsupported and supported nanoparticles were characterized to get information about the morphology and crystallite size by the use of TEM and PXRD. The combined *in situ* studies of the model catalysts were done using the magnetometer and PXRD cell.

The nanoparticles used in this study as a base line catalytically behave similar to the nanoparticles used in Nyathi [3] work up to the temperature of 350°C, beyond which they lose activity. The prepared nanosheets and nanobelts structures contained nanoparticles that showed the same catalytic trend as the nanoparticles, with slight changes in catalytic behaviour due to particle size factor. The TEM micrographs of the spent samples of the nanosheets and nanobelts showed loss of morphology which was confirmed to occur during the reduction from CoO to Co^0. Only the nanocubes displayed a single crystal domain which resulted in superior surface specific activity. The cubic nanoparticles also lose morphology adopting a spherical shape during CoO reduction to Co^0.

7 Recommendations

One major challenge resulting from the present study is achieving single crystallite nanosheet and nanobelt samples. Efforts should therefore be directed at developing novel synthesis routes yielding Co_3O_4 crystallites preferentially exposing planes other than the {001}. Regarding nanocubes, the size of said morphologies should be decreased to increase the mass specific surface area available for reaction and potentially increase overall catalyst activity.

The composition of industrial hydrogen includes trace amounts of water vapour, so it will be important to simulate the industrial conditions for better qualification of the model catalyst systems.

References

[1] Xie, X., Li, Y., Liu, Z. Q., Haruta M. & Shen, W. (2009). Low-temperature oxidation of CO catalysed by Co_3O_4 nanorods. *Nature*. 458, 746–749.

[2] Hu, L., Sun, K., Peng, Q., Xu, B. & Li, Y. (2010). Surface active sites on Co_3O_4 nanobelt and nanocube model catalysts for CO oxidation. *Nano Research.* 3, 363–368.

[3] Nyathi, T.M. (2015). Preferential Oxidation of Carbon Monoxide in Hydrogen-rich Gases over Supported Cobalt Oxide Catalysts. Masters Thesis, University of Cape Town, Department of Chemical Engineering, Cape Town.

[4] Ndhlovu, P. (2010). Characterization of coke obtained over MgO-modified Ni/SiO_2 in the decomposition of methane. MSc Thesis, University of the Witwatersrand, Johannesburg..

[5] Economides, M.J. & Wood, D.A. (2009). The state of natural gas. *Journal of Natural Gas Science and Engineering*. 1, 1–13.

[6] Beck, F. & Martinot, E. (2004). Renewable Energy Policies and Barriers. *Encyclopedia of Energy.* 34, 365–383.

[7] Dinica, V. & Bressers, H. (2003). The implementation of renewable energy policies: theoretical considerations and experiences from Spain, Netherlands and United Kingdom. *Center for Clean Technology and Environmental Policy,* University of Twente. 1–6.

[8] Castaño, M.G. (n.d.). Design , characterization and structuring of Pt based catalysts for Water Gas Shift reaction. PhD Thesis. Universidad de Sevilla, Spain.

[9] Elliott, D.C. (2007). Historical developments in hydroprocessing bio-oils, Energy and Fuels. *Energy & Fuels (ACS Publications)*. 21, 1792–1815.

[10] Hamelinck, C.N. & Faaij, A. (2002). Future prospects for production of methanol and hydrogen from biomass. *Journal of Power Sources*. 111, 1–22.

[11] Brown Jr., M. L., Green, A. W., Cohn, G. & Andersen, H. C. (1960). Purifying hydrogen by selective oxidation of carbon monoxide. *Industrial and Engineering Chemistry.* 52, 841-844.

[12] Dry, M.E. (2002). The Fischer-Tropsch process: 1950-2000, Catalysis Today. 71, 227–241.

[13] Ma, J., Liu, W., Zhang & Zhao, S. Y. (2011). PFR cube-like core-shell nanocomposite prepared via a facile one-step hydrothermal approach. *Journal of Nanoparticle Research.* 13, 1219–1228.

[14] Gnanapragasam, N. V., Reddy, B. V. & Rosen, M.A. (2010). Hydrogen production from coal gasification for effective downstream CO_2 capture. *International Journal of Hydrogen Energy.* 35, 4933–4943.

[15] Deng, W., De Jesus, J., Saltsburg, H. & Flytzani-Stephanopoulos, M. (2005). Low-content gold-ceria catalysts for the water-gas shift and preferential CO oxidation reactions. *Applied Catalysis A: General.* 291, 126–135.

[16] Freni, S., Calogero, G. & Cavallaro, S. (2000). Hydrogen production from methane through catalytic partial oxidation reactions. *Journal of Power Sources*. 87, 28–38.

[17] Ogden, J.M. (1999). Prospects for buildingahydrogen energy infrastructure. *Annual Review of Environment and Resources*. 24, 227–79.

[18] Ghenciu, A.F. (2002). Review of fuel processing catalysts for hydrogen production in PEM fuel cell systems. *Current Opinion in Solid State and Materials Science*. 6, 389–399.

[19] Mishra, A. & Prasad, R. (2011). A Review on Preferential Oxidation of Carbon Monoxide in Hydrogen Rich Gases. *Bulletin of Chemical Reaction Engineering & Catalysis*. 6, 1–14.

[20] Alstrup, I. (1995). On the Kinetics of Co Methanation on Nickel Surfaces. *Journal of Catalysis*. 151, 216–225.

[21] Liu, P.K.T. (2012). Development of Hydrogen Selective Membranes / Modules as Reactors / Separators for Distributed Hydrogen Production. *Media and Process Technology Inc*. 53–57.

[22] Kasuya, F. & Tsuji, T. (1991). High purity CO gas separation by pressure swing adsorption. *Gas Separation & Purification.* 5, 242–246.

[23] Bion, N., Epron, F., Moreno, M., Mariño, F. & Duprez, D. (2008). Preferential oxidation

of carbon monoxide in the presence of hydrogen (PROX) over noble metals and transition metal oxides: Advantages and drawbacks. *Topics in Catalysis.* 51, 76–88.

[24] Zhao, Z., Lin, X., Jin, R., Wang, G. & Muhammad, T. (2012). MOx (M=Mn, Fe, Ni or Cr) improved supported Co_3O_4 catalysts on ceria–zirconia nanoparticulate for CO preferential oxidation in H_2-rich gases. *Applied Catalysis B: Environmental*. 115–116, 53–62.

[25] Woods, M.P., Gawade, P., Tan, B. & Ozkan, U.S. (2010). Preferential oxidation of carbon monoxide on Co/CeO_2 nanoparticles. *Applied Catalysis B: Environmental.* 97, 28–35.

[26] Su, D., Dou, S. & Wang, G. (2014). Single Crystalline Co_3O_4 Nanocrystals Exposed with Different Crystal Planes for Li-O_2 Batteries. *Scientific Reports*. 4, 5767.

[27] Omata, K., Kobayashi, Y. & Yamada, M. (2005). Artificial neural network-aided development of supported Co catalyst for preferential oxidation of CO in excess hydrogen. *Catalysis Communications.* 6, 563–567.

[28] Ozkara, S., Akin, N.A. Misirli, Z. & Aksoylu A. E. (2005). The Effect of Metal Loading on Structural Characteristics and Low Temperature CO Oxidation Activity of Coprecipitated Co/Al_2O_3. *Turkish Journal of Chemistry*. 29, 219–224.

[29] Claeys, M., van Steen, E., Visagie, J. & van de Loosdrecht, J. (2010). Patent No. PCT patent WO 2010/004419 A2. 4419.

[30] Claeys, M. & Fischer, N. (2013). Patent No. PCT patent WO2013/005180 A1. 5180.

[31] Karimi, A., Fatehifar E. & Alizadeh, R. (2013). Synthesis and Characterization of Nanostructured CuO/CeO_2 Catalysts via Ultrasound Assisted Techniques used for Selective Oxidation of CO. *Iranian Journal of Chemical Engineering.* 10, 51–59.

[32] Liu, Y., Fu, Q. & Stephanopoulos, M.F. (2004). Preferential oxidation of CO in H_2 over CuO-CeO_2 catalysts. *Catalysis Today.* 93–95, 241–246.

[33] Singh, S. (2014). Selective CO oxidation over $Fe_5(PO_4)_3(OH)_5$ supported Pt catalyst : Kinetic and mechanistic studies. *Indian Journal of Chemistry.* 53, 511–515.

[34] Manasilp, A. & Gulari, E. (2002). Selective CO oxidation over Pt/alumina catalysts for fuel cell applications. *Applied Catalysis B: Environmental.* 37, 17–25.

[35] Marbán, G., López, I. & Valdés-Solís, T. (2009). Preferential oxidation of CO by CuOx/CeO$_2$ nanocatalysts prepared by SACOP. Mechanisms of deactivation under the reactant stream. *Applied Catalysis A: General.* 1, 36160–169.

[36] Reina, T.R., Papadopoulou, E., Ivanova,S., Centeno, M.A., Ioannides, T. & Odriozola, J.A. (2013). Could an excellent WGS catalyst be useful in the PROX reaction. Universidad de Sevilla e Instituto de Ciencias de Materiales de Sevilla Centro mixto US-CSIC Avda. Américo Vespucio Seville, Spain. 49, 41092.

[37] Caputo, T., Lisi, L., Pirone, R. & Russo, G. (2008). On the role of redox properties of CuO/CeO$_2$ catalysts in the preferential oxidation of CO in H$_2$-rich gases. *Applied Catalysis A: General.* 348, 42–53.

[38] Polster, C.S. & Baertsch, C.D. (2008). Application of CuOx–CeO$_2$ catalysts as selective sensor substrates for detection of CO in H$_2$ fuel. *XXXVI Meeting of the Italian Section of the Combustion Institute.* 4046–4048.

[39] Avgouropoulos, G., Ioannides, T., Matralis, H.K., Batista,J. & Hocevar, S. (2001). CuO–CeO$_2$ mixed oxide catalysts for the selective oxidation of carbon monoxide in excess hydrogen. *Foundation for Research and Technology-Hellas*. 73, 33–40.

[40] Zhao, Z., Lin, X., Jin, R., Dai, Y. & Wang, G. (2011). High catalytic activity in CO PROX reaction of low cobalt-oxide loading catalysts supported on nano-particulate CeO$_2$-ZrO$_2$ oxides. *Catalysis Communications.* 12, 1448–1451.

[41] Xia, G.G., Yin, Y.G., Willis, W.S., Wang, J.Y. & Suib, S.L. (1999). Efficient Stable Catalysts for Low Temperature Carbon Monoxide Oxidation. *Journal of Catalysis.* 185, 91–105.

[42] Kang, M., Song, M.W. & Lee, C.H. (2003). Catalytic carbon monoxide oxidation over CoOx/CeO$_2$ composite catalysts. *Applied Catalysis A: General.* 251, 143–156.

[43] Chamousis, R. (2008). Hydrogen: fuel of the future. The Scientific Research Society. CSU Stanislaus, CA.

[44] Nithyapathi, C., R, Aravind Kumar, T. & Subanesh Shyam, R. (2013). Hydrogen As an Alternative Fuel for Commercial Airplanes, 476–480.

[45] Herzog, A. (2005). A Hydrogen future. An Economic and Environmental Assessment

of Hydrogen Production Pathways. Natural Resources Defense Council

[46] Udengaard, N.R. (2004). Hydrogen Production By Steam Reforming of Hydrocarbons. *Preprints of Papers- American Chemical Society, Division of Fuel Chemistry.* 49, 906–907.

[47] Wang, Y., Chen, K.S., Mishler, J., Cho, S.C. & Adroher, X.C. (2011). A review of polymer electrolyte membrane fuel cells: Technology, applications, and needs on fundamental research. *Applied Energy.* 88, 981–1007.

[48] Larminie, J. & Dicks, A. (2003). Fuel cell systems explained. Oxford Brookes University, UK

[49] Ouyang, X., Bednarova, L., Ho, P. & Besser, R. (2005). Preferential Oxidation of Carbon Monoxide in a Thin-Film Catalytic Microreactor: Advantages and Limitations. *AIChE Journal*. 51, 1758–1772.

[50] Ajmera, S., Delattre, C., Schmidt, M.A. & Jensen, K.F. (2002). Microfabricated Differential Reactor for Heterogeneous Gas Phase Catalyst Testing. *Journal of Catalysis*. 209, 401–412.

[51] Kim, D.H. & Lim, M.S. (2002). Kinetics of selective CO oxidation in hydrogen-rich mixtures on Pt/alumina catalysts. *Applied Catalysis A: General.* 224, 27–38.

[52] Lee, S.H., Han, J. K. & Lee, Y. (2002). Development of 10-kWe preferential oxidation system for fuel cell vehicles. *Journal of Power Sources.* 109, 394–402.

[53] Surangalikar, H. Ouyang, X. & Besser, R.S. (2003). Experimental study of hydrocarbon hydrogenation and dehydrogenation reactions in silicon microfabricated reactors of two different geometries. *Chemical Engineering Journal*. 93, 217–224.

[54] Besser, R.S., Ouyang, X. & Surangalikar, H. (2003). Hydrocarbon hydrogenation and dehydrogenation reactions in microfabricated catalytic reactors. *Chemical Engineering Science*. 58, 19–26.

[55] Zhao, Z., Bao, T., Zeng, Y., Wang, G. & Muhammad, T. (2013). Efficient cobalt-manganese oxide catalyst deposited on modified AC with unprecedented catalytic performance in CO preferential oxidation. *Catalysis Communications*. 32, 47–51.

[56] Ding, Z., Yang, H. Liu, J. Dai, W. Chen, X. Wang, X. (2011). Environmental Promoted

CO oxidation activity in the presence and absence of hydrogen over the TiO_2-supported Pt/Co–B bicomponent catalyst. *Applied Catalysis B: Environmental.* 101, 326–332.

[57] Zhao ,Z., Lin, X., Jin, R., Dai,Y. & Wang, G. (2011). High catalytic activity in CO PROX reaction of low cobalt-oxide loading catalysts supported on nano-particulate CeO_2-ZrO_2 oxides. *Catalysis Communications*. 12, 1448–1451.

[58] Kim, J.H., Woo, H.J., Kim, C.K. & Yoon, C.S. (2009). The catalytic effect of Pt nanoparticles supported on silicon oxide nanowire. *Nanotechnology*. 20, 235306.

[59] Pozdnyakova, O., Teschner, D., Wootsch, A. Kröhnert, J. Steinhauer, B. Sauer, H. (2006). Preferential CO oxidation in hydrogen (PROX) on ceria supported catalysts PART I . Oxidation state and surface species on Pt/CeO_2 under reaction conditions. *Journal of Catalysis.* 237, 1–16.

[60] Wootsch, A., Descorme, C. & Duprez, D. (2004). Preferential oxidation of carbon monoxide in the presence of hydrogen (PROX) over ceria-zirconia and alumina-supported Pt catalysts. *Journal of Catalysis.* 225, 259–266.

[61] Ko, E.Y., Park, E.D., Seo, K.W., Lee, H.C., Lee, D. & Kim, S. (2006). A comparative study of catalysts for the preferential CO oxidation in excess hydrogen. *Catalysis Today.* 116, 377–383.

[62] Luengnaruemitchai, A., Osuwan, S. & Gulari, E. (2004). Selective catalytic oxidation of CO in the presence of H2 over gold catalyst. *International Journal of Hydrogen Energy*. 29, 429–435.

[63] Wang, X.L., Yu, X. Wu, L., Yuan, F. Guo, Y.G. & Ma, Y. (2009). Synthesis of single-crystalline Co_3O_4 octahedral cages with tunable surface aperture and their lithium storage properties. *The Journal of Physical Chemistry C*. 113, 15553–15558.

[64] Atalik, B. & Uner, D. (2006). Structure sensitivity of selective CO oxidation over Pt/??-Al_2O_3. *Journal of Catalysis*. 241, 268–275.

[65] Tanaka, K.I., He, H., Shou, M. & Shi, X. (2011). Mechanism of highly selective low temperature PROX reaction of CO in H_2: Oxidation of CO via HCOO with OH. *Catalysis Today.* 175, 467–470.

[66] Hulteberg, P.C., Brandin, J.G.M., Silversand, F.A. & Lundberg, M. (2005). Preferential oxidation of carbon monoxide on mounted and unmounted noble-metal catalysts in hydrogen-rich streams. *International Journal of Hydrogen Energy.* 30, 1235–1242.

[67] Mariño, F., Descorme, C. & Duprez, D. (2004). Noble metal catalysts for the preferential oxidation of carbon monoxide in the presence of hydrogen (PROX). *Applied Catalysis B: Environmental.* 54, 59–66.

[68] Park, J.W., Jeong, J.H., Yoon, W.L., Jung, H., Lee,H.T. & Lee,D.K. (2004). Activity and characterization of the Co-promoted $CuO-CeO_2$/??-Al_2O_3 catalyst for the selective oxidation of CO in excess hydrogen. *Applied Catalysis B: General.* 274, 25–32.

[69] Kandoi, S., Gokhale, A.A., Grabow, L.C., Dumesic, J.A. & Mavrikakis, M. (2003). Why Au and Cu are more selective than Pt for preferential oxidation of CO at low temperature. *Catalysis Letters. 93,* 93–100.

[70] Park, E.D., Lee, D. & Lee, H.C. (2009). Recent progress in selective CO removal in a H_2-rich stream. Catalysis Today. 139, 280–290.

[71] Mars, P. & van Krevelen, D.W. (1954). Oxidations carried out by means of vanadium oxide catalysts. *Chemical Engineering Science.* 3, 41–59.

[72] Kabel, R.L. & Perti D. (1985). Kinetics of CO Oxidation Over $Co_3O_4/\gamma\text{-}Al_2O_3$. Department of Chemical Engineering Pennsylvania State University. 31, 1420–1426.

[73] Bobaru, S.C. (2006). High-Pressure STM Studies of Oxidation Catalysis, PhD thesis, Leiden University, Leiden, the Netherlands.

[74] Hernández, W.Y., Centeno, M.A., Romero-Sarria, F., Ivanova, S., Montes, M. & Odriozola, J.A. (2010). Modified cryptomelane-type manganese dioxide nanomaterials for preferential oxidation of CO in the presence of hydrogen. *Catalysis Today*. 157, 160–165.

[75] Mariño, F., Descorme, C. & Duprez, D. (2005). Supported base metal catalysts for the preferential oxidation of carbon monoxide in the presence of excess hydrogen (PROX), *Applied Catalysis B: Environmental*. 58, 175–183.

[76] Manzoli, M., Avgouropoulos, G., Tabakova, T., Papavasiliou, J., Ioannides, T. & Boccuzzi, F. (2008). Preferential CO oxidation in H_2-rich gas mixtures over Au/doped

ceria catalysts. *Catalysis Today.* 138, 239–243.

[77] Ratnasamy, P., Srinivas, D., Satyanarayana, C.V., Manikandan, P., Senthil, R.S., Kumaran, V. & Sachin, M. (2004). Influence of the support on the preferential oxidation of CO in hydrogen-rich steam reformates over the CuO-CeO_2-ZrO_2 system. *Journal of Catalysis*. 221, 455–465.

[78] Wang, J.B., Tsai, D.H. & Huang, T.J. (2002). Synergistic Catalysis of Carbon Monoxide Oxidation over Copper Oxide Supported on Samaria-Doped Ceria. *Journal of Catalysis*. 208, 370–380.

[79] Gamarra, D. & Martínez-Arias, A. (2009). Preferential oxidation of CO in rich H_2 over CuO/CeO2: Operando-DRIFTS analysis of deactivating effect of CO_2 and H_2O. *Journal of Catalysis*. 263, 189–195.

[80] Reitz, T.L., Ahmed, S., Krumpelt, M., Kumar, R. & Kung, H.H. (2000). Characterization of CuO/ZnO under oxidizing conditions for the oxidative methanol reforming reaction. *Journal of Molecular Catalysis A: Chemical*. 162, 275–285.

[81] Teng, Y., Kusano, Y., Azuma, M., Haruta, M. & Shimakawa, Y. (2011). Morphology effects of Co_3O_4 nanocrystals catalyzing CO oxidation in a dry reactant gas stream. *Catalysis Science & Technology.* 1, 920.

[82] He, T., Chen, D., Jiao, X. & Wang, Y. (2006). Co_3O_4 nanoboxes: Surfactant-templated fabrication and microstructure characterization. *Advanced Materials.* 18, 1078–1082.

[83] Jansson, J., Palmqvist, A.E.C., Fridell, E., Skoglundh, M., Österlund, L. & Thormählen, P. (2002). On the catalytic activity of Co_3O_4 in low-temperature CO oxidation. *Journal of Catalysis*. 211, 387–397.

[84] Guo, Q. & Liu,Y. (2008). MnOx modified Co_3O_4-CeO_2 catalysts for the preferential oxidation of CO in H_2-rich gases. *Applied Catalysis B: Environmental.* 82, 19–26.

[85] Zhao, Z., Yung, M.M. & Ozkan U.S. (2008). Effect of support on the preferential oxidation of CO over cobalt catalysts. *Catalysis Communications*. 9, 1465–1471.

[86] Yung, M.M., Zhao, Z., Woods, M.P. & Ozkan, U.S. (2008). Preferential oxidation of carbon monoxide on CoOx/ZrO_2. *Journal of Molecular Catalysis A: Chemical*. 279, 1–9.

[87] van Steen, E. & Claeys, M. (2008). Fischer-Tropsch catalysts for the biomass-to-liquid process. *Chemical Engineering & Technology*. 31, 655–666.

[88] Argyle, M. & Bartholomew, C. (2015). Heterogeneous Catalyst Deactivation and Regeneration: A Review. *Catalysts*. 5, 145–269.

[89] Bartholomew, C.H. (2001). Mechanisms of catalyst deactivation. *Applied Catalysis A: Genera.l* 212, 17–60.

[90] Fujita, S.I. & Takezawa, N. (1997). Difference in the selectivity of CO and CO2 methanation reactions. Chemical Engineering Journal 68, 63-68.

[91] Dunleavy, J.K. (2006). Final Analysis: Sulfur as a Catalyst Poison. *Platinum Metals Review.* 50, 110–110.

[92] Forzatti, P. & Lietti, L. (1999). Catalyst deactivation. *Catalysis Today.* 52, 165–181.

[93] Monyanon, S., Pongstabodee,S. & Luengnaruemitchai, A. (2007). Preferential oxidation of carbon monoxide over Pt, Au monometallic catalyst, and Pt-Au bimetallic catalyst supported on ceria in hydrogen-rich reformate. *Journal of the Chinese Institute of Chemical Engineers*. 38, 435–441.

[94] Schubert, M.M. & Gasteiger, H.R. (1997). Surface Formates as Side Products in the Selective CO Oxidation on Pt/γ-Al_2O_3. *Journal of Catalysis.* 172, 256–258.

[95] Xie, Y., Dong, F., Heinbuch, S., Rocca, J.J. & Bernstein, E.R. (2010). Oxidation reactions on neutral cobalt oxide clusters: experimental and theoretical studies. *Physical Chemistry Chemical Physics*. 12, 947–959.

[96] Moulijn, J., Van Diepen, E. & Kapteijn, F. (2001). Catalyst deactivation: Is it predictable? What to do? *Applied Catalysis A: General.* 212, 3–16.

[97] Shatokha, V. (2012). Sintering - Methods and Products. *Catalysis Reviews*. 326.

[98] Perry, R., Green, D. & Maloney, J. (n.d.) Perry's chemical engineers' handbook, http://pubs.acs.org/doi/pdf/10.1021/ed027p533.1%5Cnhttp://www.lavoisier.fr/livre/notice.asp?ouvrage=1037804.

[99] Steele, B.C. & Heinzel, A. (2001). Materials for fuel-cell technologies. *Nature*. 414, 345–352.

[100] Baschuk, J.J. & Li, X. (2001). Carbon monoxide poisoning of proton exchange membrane fuel cells, *International Journal of Energy Research.* 25, 695–713.

[101] Lu, G.Q., Diniz da Costa, J.C., Duke, M., Giessler, S., Socolow, R. & Williams, R.H. (2007). Inorganic membranes for hydrogen production and purification: A critical review and perspective. *Journal of Colloid and Interface Science.* 314, 589–603.

[102] Basile, A., Iulianelli, A., Longo, T., Liguori S. & De Falco, M. (n.d.) Membrane Reactors for Hydrogen Production Processes.

[103] van Veen, H.W., Venema, K., Bolhuis, H., Oussenko, I., Kok, J. & Poolman, B. (1996). Multidrug resistance mediated by a bacterial homolog of the human multidrug transporter MDR1. Proceedings of the National Academy of Sciences. 93, 10668–10672.

[104] Iyuke, S.E., Mohamad, B., Daud, W.R., Kadhum W., Fisal, H.Z. & Shariff, M. (2000). Removal of Co from process gas with Sn-activated carbon in pressure swing adsorption. *Journal of Chemical Technology and Biotechnology*. 75, 803–811.

[105] Linde, (2010). Hydrogen Recovery by Pressure Swing Adsorption, Engineering. 4–8.

[106] Tagliabue, M., Farrusseng, D., Valencia, S., Aguado, S., Ravon, U. & Rizzo, C. (2009) Natural gas treating by selective adsorption: Material science and chemical engineering interplay. *Chemical Engineering Journal*. 155, 553–566.

[107] Tian, D., Liu, Z., Li, D., Shi, H., Pan, W. & Cheng, Y. (2013). Bimetallic Ni-Fe total-methanation catalyst for the production of substitute natural gas under high pressure. *Fuel.* 104, 224–229.

[108] Takenaka, S., Shimizu, T. & Otsuka, K. (2004). Complete removal of carbon monoxide in hydrogen-rich gas stream through methanation over supported metal catalysts. *International Journal of Hydrogen Energy*. 29, 1065–1073.

[109] Xie, X. & Shen, W. (2009). Morphology control of cobalt oxide nanocrystals for promoting their catalytic performance. *Nanoscale.* 1, 50–60.

[110] Deori, K. & Deka, S. (2013). Morphology oriented surfactant dependent CoO and reaction time dependent Co_3O_4 nanocrystals from single synthesis method and their optical and magnetic properties. *Crystal Engineering Communication.* 5, 8465.

[111] Hayashi, H. & Hakuta, Y. (2010). Hydrothermal Synthesis of metal oxide nanoparticles in supercritical water. *Materials (Basel).* 3, 3794–3817.

[112] Jensen, K. (2013). Watching Materials Form: Particle Formation and Growth in Hydrothermal Synthesis, 159.

[113] Bremholm, M., Felicissimo, M. & Iversen, B.B. (2009). Time-Resolved In Situ Synchrotron X-ray Study and Large-Scale Production of Magnetite Nanoparticles in Supercritical Water. *Angewandte Chemie International Edition.* 121, 4882–4885.

[114] Adschiri, T., Kanazawa, K. & Arai, K. (1992). Rapid and Continuous Hydrothermal Crystallization of metal oxide. *Journal of the American Ceramic Society.* 75, 1019-1022.

[115] Adschiri, T., Hakuta, Y. & Arai, K. (2000). Hydrothermal synthesis of metal oxide fine particles at supercritical conditions. *Industrial & Engineering Chemistry Research.* 39, 4901–4907.

[116] Beuermann, S., Buback, M. & Busch, M. (1999). Chemical Synthesis Using Supercritical Fluids.

[117] Cabrera, N., Coleman, R.V. & Gilman, J.J. (1963). The Art and Science of Growing Crystals, Wiley, New York. 240.

[118] Hou, Y., Kondoh, H., Shimojo, M., Kogure, T. & Ohta, T. (2005). High-yield preparation of uniform cobalt hydroxide and oxide nanoplatelets and their characterization. *The Journal of Physical Chemistry B.* 109, 19094–19098.

[119] Rabenau, A. (1985). The Role of Hydrothermal Synthesis in Preparative Chemistry. *Angewandte Chemie International Edition*. 24, 1026–1040.

[120] Cheng, H., Ma, J., Zhao, Z. & Qi, L. (1995). Hydrothermal Preparation of Uniform Nanosize Rutile and Anatase Particles. *Chemistry of Materials*. 7, 663–671.

[121] Hu, L., Peng, Q. & Li, Y. (2008). Selective Synthesis of Co_3O_4 Nanocrystal with Different Shape and Crystal. *Journal of the American Chemical Society*. 16136–16137.

[122] Wang, Y., Zhong, Z., Chen, Y. & Lin, J. (2011). Controllable synthesis of Co_3O_4 from nanosize to microsize with large-scale exposure of active crystal planes and their excellent rate capability in supercapacitors based on the crystal plane effect. *Nano*

Research. 4, 695–704.

[123] Sun, S.G., Chen, A.C., Huang, T.S., Li, J.B. & Tian, Z.W. (1992). Electrocatalytic properties of Pt(111), Pt(332), Pt(331) and Pt(110) single crystal electrodes towards ethylene glycol oxidation in sulphuric acid solutions. Journal of Electroanalytical Chemistry. 340, 213–226.

[124] Urbaniak, M. (2012). Magnetic hysteresis and basic magnetometry.

[125] Serway, R.A. & Jewett, J.W. (2014). Physics for Scientists and Engineers with Modern Physics. Boston: Brooks/Cole

[126] Dalmon, J. (1994). Magnetic measurements and catalysis. In B. Imelik, & J. Verdrine (Eds.), Catalyst characterisation: Physical techniques for solid materials (p. 585). New York: Plenum Press.

[127] Chernavskii, P.A., Dalmon, J.A., Perov, N.S. & Khodakov, A.Y. (2009). Magnetic Characterization of Fischer-Tropsch Catalysts. *Oil & Gas Science and Technology.* 64, 25–48.

[128] Niu, H. Chen, Q. Zhu, H. Lin, Y. & Zhang, X. (2003). Magnetic field-induced growth and self-assembly of cobalt nanocrystallites. *Journal of Materials Chemistry.* 13, 1803.

[129] Wang, X.D., Shen, Z.X., Sang, T., Cheng, X.B., Li, M.F. & Chen, L.Y. (2010). Preparation of spherical silica particles by Stöber process with high concentration of tetra-ethyl-orthosilicate. *Journal of Colloid and Interface Science.* 341, 23–29.

[130] Feng, J. & Zeng, H.C. (2003). Size-Controlled Growth of Co_3O_4 Nanocubes. *Chemistry of Materials.* 15, 2829–2835.

[131] Lee, S.R. (n.d.). Cobalt Oxide Nanocubes, Department of Chemical Engineering Cornell University, Ithaca, NY, 14853.

[132] Wang, Q., Xia, Y. & Jiang, C. (2014). Mesoporous nanobelts and nano-necklaces of Co_3O_4 converted from β-$Co(OH)_2$ nanobelts via a thermal decomposition route for the electrocatalytic oxidation of H_2O_2. *Crystal Engineering Communication.*16, 9721–9726.

[133] Fischer, N., Van Steen, E. & Claeys, M. (2011). Preparation of supported nano-sized cobalt oxide and fcc cobalt crystallites. *Catalysis Today.* 171, 174–179.

[134] Fischer, N., Clapham, B., Feltes, T., van Steen, E. & Claeys, M. (2014). Sizedependent phase transformation of catalytically active nanoparticles captured in situ. *Angewandte Chemie International Edition.* 53, 1342-1345.

[135] Stöber, W. & Fink, A. (1968). Controlled Growth of Monodisperse Silica Spheres in the Micron Size Range. *Journal of Colloid and Interface Science*. 69, 62–69.

[136] Yih, H.T., Jason, A.D., Kohki F., Ganesha, N.V. Alexei V.D. & Stinea K.J. (2011). Surface area and pore size characteristics of nanoporous gold subjected to thermal, mechanical, or surface modification studied using gas adsorption isotherms, cyclic voltammetry, thermogravimetric analysis, and scanning electron microscopy. *Journal of Materials Chemistry*. 72, 181–204.

[137] Sánchez de Rojas, M.I., Pilar de Luxan, M. & Frias, M. (1986). Inductively coupled plasma emission spectrometry. *Materiales de Construcción*. 36, 31–46..

[138] Morgan, D.J. (n.d.). X-Ray Photoelectron Spectroscopy (XPS): An Introduction. Cardiff Catalysis Institute, School of Chemistry, Cardiff University, Cardiff.

[139] Iablokov, V. (2011). Manganese and Cobalt oxides as highly active catalysts for CO oxidation. PhD Thesis. Universite libre de bruxelles faculte des sciences Chimie Physique des Matériaux.

[140] Fischer, N., Clapham, B., Feltes, T., van Steen, E., & Claeys, M. (2014). Sizedependent phase transformation of catalytically active nanoparticles captured in situ. *Angewandte Chemie International Edition*. 53, 1342-1345.

[141] Fischer, N. (2011). Preparation of Nano and Ångstrøm sized Cobalt Ensembles and their Performance in the Fischer-Tropsch Synthes, Phd Thesis, University of Cape Town, South Africa.

[142] Clapham, B. 2012. The development of an in situ X-ray diffraction cell for Fischer-Tropsch catalyst characterisation. MSc Thesis. University of Cape Town, South Africa.

[143] Tian, L., Zhu, J.L., Chen, L., An, B., Liu, Q.Q. & Huang, K.L. (2011) Synthesis and characterization of cobalt hydroxide nanobelts. *Journal of Nanoparticle Research*. 13, 3483–3488.

[144] Che, H., Liu, A., Hou, J., Zhang, X., Bai, Y. & Mu, J. (2014). Synthesis of one-

dimensional porous Co_3O_4 nanobelts and their ethanol gas sensing properties. *Materials Research Bulletin.* 59, 69–76.

[145] Vladislav, G., Zuev, M.G. & Sokovnin, S.Y. (2015). Properties of Silicon Dioxide Amorphous Nanopowder Produced by Pulsed Electron Beam Evaporation. *Journal of Nanotechnology*. 2015, 8.

[146] Lv, Y., Li, Y., Ta, N. & Shen, W. (2014). Co_3O_4 nanosheets: synthesis and catalytic application for CO oxidation at room temperature. *Science China Chemistry*. 57, 873–880.

[147] Zeng, L., Li, K., Huang, F., Zhu, X. & Li, H. (2016). Effects of Co_3O_4 nanocatalyst morphology on CO oxidation: Synthesis process map and catalytic activity. *Chinese Journal Catalysis*. 37, 908–922.

[148] Holm, A.C. F. & Clark, A. (1968). Reduction studieson suupported metal oxide catalysts. *Journal of catalysis.* 11, 305-316.

[149] Fischer, N. Minnermann, M. Baeumer, M. Van Steen, E. & Claeys, M. (2012). Metal Support Interactions in Co_3O_4/Al_2O_3 Catalysts Prepared from w/o Microemulsions. *Catalysis Letters.* 142, 830–837.

[150] Khodakov, A.Y., Chu, W. & Fongarland, P. (2007). Advances in the Development of Novel Cobalt Fischer−Tropsch Catalysts for Synthesis of Long-Chain Hydrocarbons and Clean Fuels. *Chemical Reviews (ACS Publications).* 107, 1692–1744.

[151] Jacobs, G., Ji, Y., Davis, B.H., Cronauer, D., Kropf, A.J. & Marshall, C.L. (2007). Fischer-Tropsch synthesis: Temperature programmed EXAFS/XANES investigation of the influence of support type, cobalt loading, and noble metal promoter addition to the reduction behavior of cobalt oxide particles, *Applied Catalysis A: General.* 333, 177–191.

[152] Sirijaruphan, A., Horvath, A., Goodwin, J.G. & Oukaci, R. (2003). Cobalt aluminate formation in alumina-supported cobalt catalysts: Effects of cobalt reduction state and water vapor. *Catalysis Letters.* 91, 89–94.

[153] Jasik, A., Wojcieszak, R., Monteverdi, S., Ziolek, M. & Bettahar, M.M. (2005). Study of nickel catalysts supported on Al_2O_3, SiO_2 or Nb_2O_5 oxides. *Journal of Molecular Catalysis A: Chemical.* 242, 81–90.

[154] Rynkowski, J.M., Paryjczak, T. & Lenik, M. (1993). On the nature of oxidic nickel phases in NiO-Al_2O_3 catalysts. *Applied Catalysis A: General*. 106, 73–82.

[155] Wolf, M., Fischer, N. & Claeys, M. (2016). Effectiveness of catalyst passivation techniques studied *in situ* with a magnetometer. *Catalysis Today*. 275, 135–140.

[156] Lukashuk, L., Föttinger, K., Kolar, E., Rameshan, C., Teschner, D. & Hävecker, M. (2016). Operando XAS and NAP-XPS studies of preferential CO oxidation on Co_3O_4 and CeO_2-Co_3O_4 catalysts. *Journal of Catalysis*. 344, 1–15.

[157] Karaca, H., Safonova, O.V., Chambrey, S., Fongarland, P., Roussel, P. & Griboval-Constant A. (2011). Structure and catalytic performance of Pt-promoted alumina-supported cobalt catalysts under realistic conditions of Fischer-Tropsch synthesis. *Journal of Catalysis*. 277, 14–26.

[158] Siegel, J. & Olsen, C. (2008). Feed Contaminants in Hydroprocessing Units. *Advanced refining technologies Chicago*. 2, 2–6.

[159] Mohandas, J.C., Gnanamani, M.K., Jacobs, G., Ma, W., Ji, Y. & Khalid, S. (2011). Fischer-tropsch synthesis: Characterization and reaction testing of cobalt carbide. *ACS Catalysis.*1, 1581–1588.

[160] Ducreux, O., Rebours, B., Lynch, J. Roy-Auberger, M. & Bazin D. (2009) Microstructure of Supported Cobalt Fischer-Tropsch Catalysts. *Oil & Gas Science and Technology*. 63, 9–19.

[161] Ribeiro Da Silva, M.A.V., Monte, M.J.S., Lobo Ferreira, A.I.M.C., Oliveira, J.A.S.A. & Cimas, Á. (2010). Experimental and Computational Thermodynamic Study of Three Monofluoronitrobenzene Isomers. *The Journal of Physical Chemistry B*. 114, 7909–7919.

[162] Nyathi, T., Fischer, N., York, A. & Claeys, M. (2016). Effect of crystallite size on the performance and phase transformation of Co_3O_4/Al_2O_3 catalysts during CO-PrOx - An *in situ* study, Faraday Discussion [Acepted manuscript].

[163] Guo, Q., & Liu, Y. (2016). MnO_x modified Co_3O_4-CeO_2 catalysts for the preferential oxidation of CO in H_2-rich gases. *Applied Catalysis B: Environmental* 82, 19–26.

[164] Chang, L., Sasirekha, N., Chen, Y., & Wang, W. (2006). Preferential oxidation of CO in

H2 stream over Au/MnO_2-CeO_2 catalysts. *Industrial & Engineering Chemistry Research* 45, 4927–4935.

[165] Liua, Y., Fub, Q. & Stephanopoulos, M.F. (2004). Preferential oxidation of CO in H_2 over CuO-CeO_2 catalysts. *Catalysis Today* 93–95, 241–246.

[166] Papavasiliou, J., Avgouropoulos, G. & Ioannides, T. (2006). In situ combustion synthesis of structured Cu-Ce-O and Cu-Mn-O catalysts for the production and purification of hydrogen. *Applied Catalysis B: Environmental* 66, 168–174.

[167] Minemura, Y., Kuriyama, M., Ito, S., Tomishige, K. & Kunimori K. (2006). In situ combustion synthesis of structured Cu-Ce-O and Cu-Mn-O catalysts for the production and purification of hydrogen. *Catalysis Communications* 7, 623–626.

[168] Snytnikov, P.V., Sobyanin, V.A., Belyaev, V.D., Tsyrulnikov, P.G., Shitova, N.B., & Shlyapin, D.A. (2003). Selective oxidation of carbon monoxide in excess hydrogen over Pt-, Ru- and Pd-supported catalysts. *Applied Catalysis A: General* 239, 149–156.

[169] Chang, L., Sasireka, N., Chen, Y. & Wang, D.A. (2006). Preferential Oxidation of CO in H_2 Strean over Au/MnO_2-CeO_2 Catalysts. *Industrial & Engineering Chemistry Research* 45, 4927–4935.

[170] Bion, N., Epron, F., Moreno, M., Marinõ, F. & Duprez. D. (2008). Preferential Oxidation of Carbon Monoxide in the Presence of Hydrogen (PROX) over Noble Metals and Transition Metal Oxides: Advantages and Drawbacks. *Top Catal* 51, 76–88.

[171] Liotta, L.F., Di Carlo, G., Pantaleo, G. & Venezia. A.M. (2010). Supported gold catalysts for CO oxidation and preferential oxidation of CO in H_2 stream: Support effect. *Catalysis Today* 158, 56-62

[172] Andreea, C.G., Huib S.V., Johan W.B. & Bernard E.N. (2005). Activation of CO, O_2 and H_2 on gold-based catalysts. *Applied Catalysis A: General* 291, 145–150.

Appendix A: Calibration of magnetometer

The sample of unsupported metallic cobalt with a mass of 0.1 g was placed into the in situ magnetometer and then heated to 700°C (heating rate: 4 °C/min) in 100 mL (NTP)/min of hydrogen. Upon reaching the temperature of 700°C, the sample was held for two hours in argon (100 mL (NTP)/min). The temperature was then cooled at the rate of 1°C/min to 25°C and held at 25°C for 3 hours.

A calibration factor of Co obtained for the *in situ* magnetometer reported as 16.8486 emu/g was used to convert the signal to magnetic units.

$$m_{Co\,formed}\,(g) = \frac{M_{experimental} \cdot 0.1\ g}{M_{calibration}}$$

Equation A. 1

$$\boldsymbol{Degree\ of\ reduction}\ (\%) = \frac{m_{Co\,formed}}{m_{Co\,loaded}} \times \mathbf{100}$$

Equation A. 2

Where $m_{Co\,formed}$ is mass of cobalt formed, $M_{experimental}$ is the sample magnetisation and $M_{calibration}$ is magnetisation measured during the calibration of the magnetometer using the 100 mg of bulk cobalt. All the measure measurements are taken at temperature T_i during the cause of the experiment. $m_{Co\,loaded}$ represents the mass of cobalt loaded initially as determined by AAS and ICP.

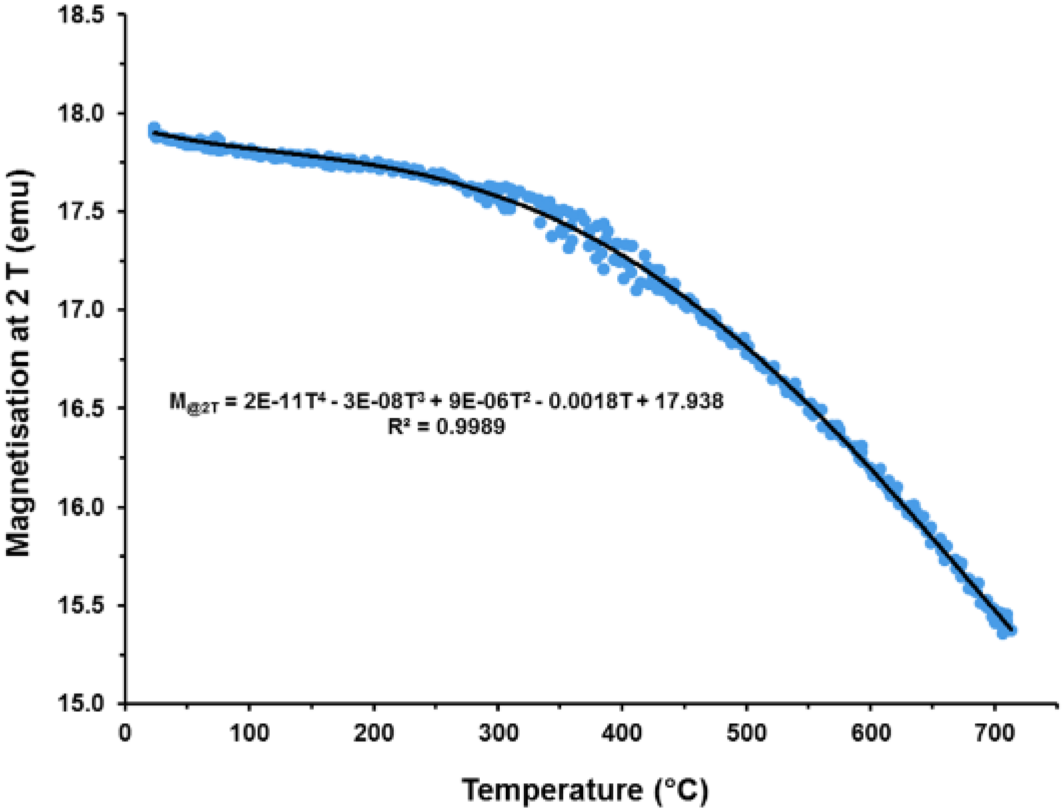

Figure 0.1: Reduction of metallic cobalt sample in in situ magnetometer as a function of temperature

Appendix B: TCD-GC calibration

The TCD calibration was done using gas mixtures of know composition as shown in table C.1. An average of five TCD areas was used to calculate the relative response factors, F$_i$, for each gas component normalised for nitrogen. To calculate the response factors, equation C.1 was used.

$$\boldsymbol{F_i = \frac{A_{N_2} n_{i,in}}{A_i n_{N_2,in}}}$$ Equation C.

1

Where $\boldsymbol{F_i}$ is the response factor of gas component $\boldsymbol{i}$ with reference to nitrogen. The variable $\boldsymbol{A_{N_2}}$ and $\boldsymbol{n_{N_2,in}}$ are the calculated peak area and the molar gas flow rate of nitrogen respectively. $\boldsymbol{A_i}$ is the calculated peak area of gas component $\boldsymbol{i}$ and $\boldsymbol{n_{i,in}}$ is the molar gas flow rate of gas component $\boldsymbol{i}$ entering the TCD.

Table A.1: GC-TCD calibration results used to obtain response factors

Gas component, i	Cylinder 1						Cylinder 2	
	N_2	CO	CO_2	CH_4	H_2	Ar	N_2	O_2
Volume %	5.20	20.10	9.80	15.20	39.60	10.10	79.0	21.0
Average of 5 peaks	619	2266	7065	1498	217864	-	20831	366
Response factor, F_i	1.00	1.067	0.326	1.161	0.022	-	1.000	1.26

Appendix C: XPS profiles

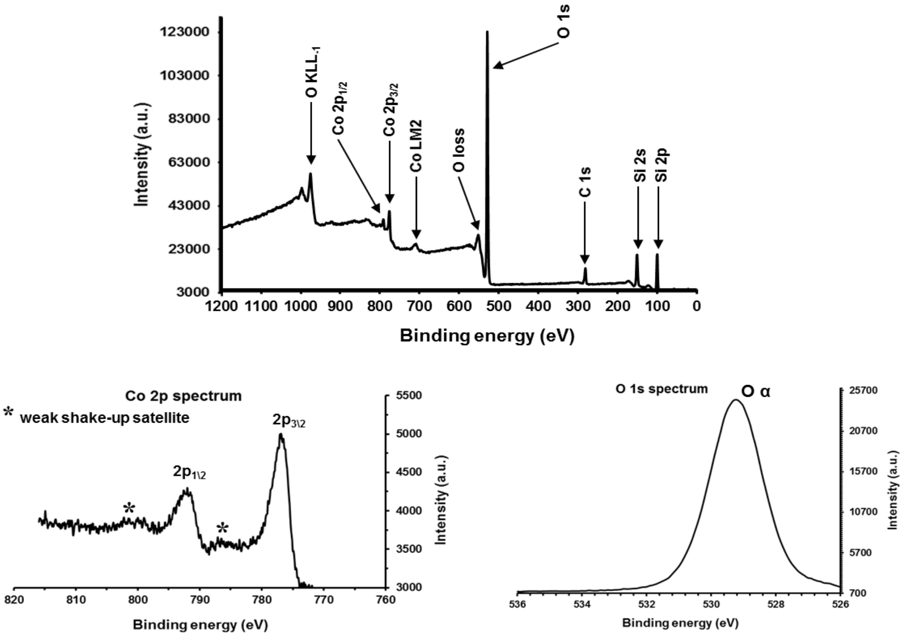

Figure B.1: XPS profiles of wide spectrum, Co 2p and O 1s in the Co_3O_4 amine nanocubes

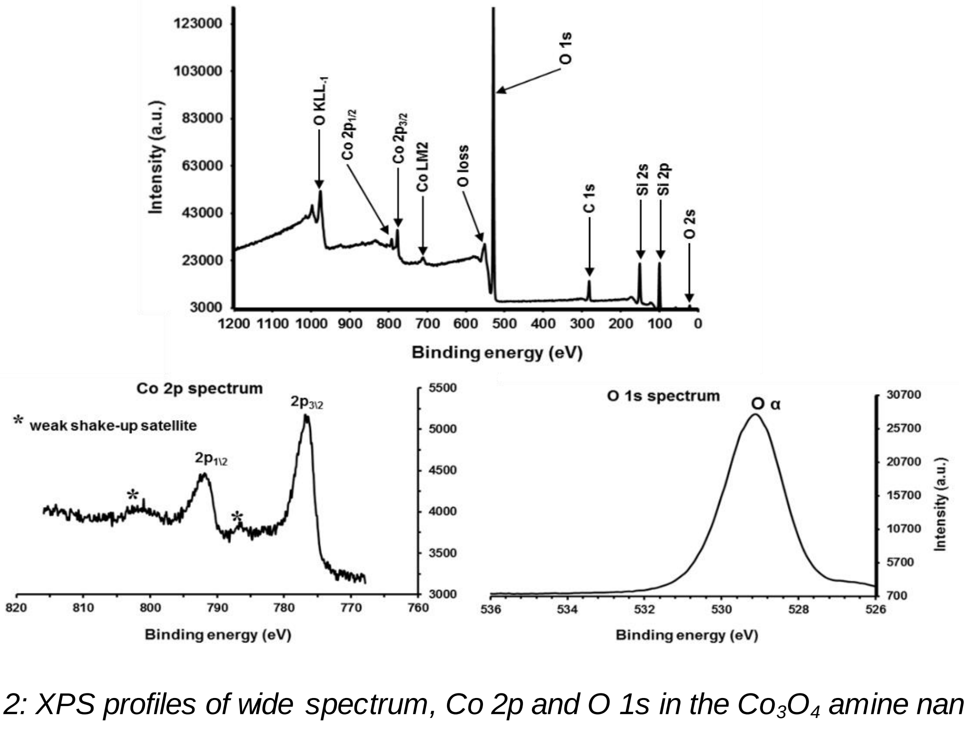

Figure B.2: XPS profiles of wide spectrum, Co 2p and O 1s in the Co_3O_4 amine nanosheets

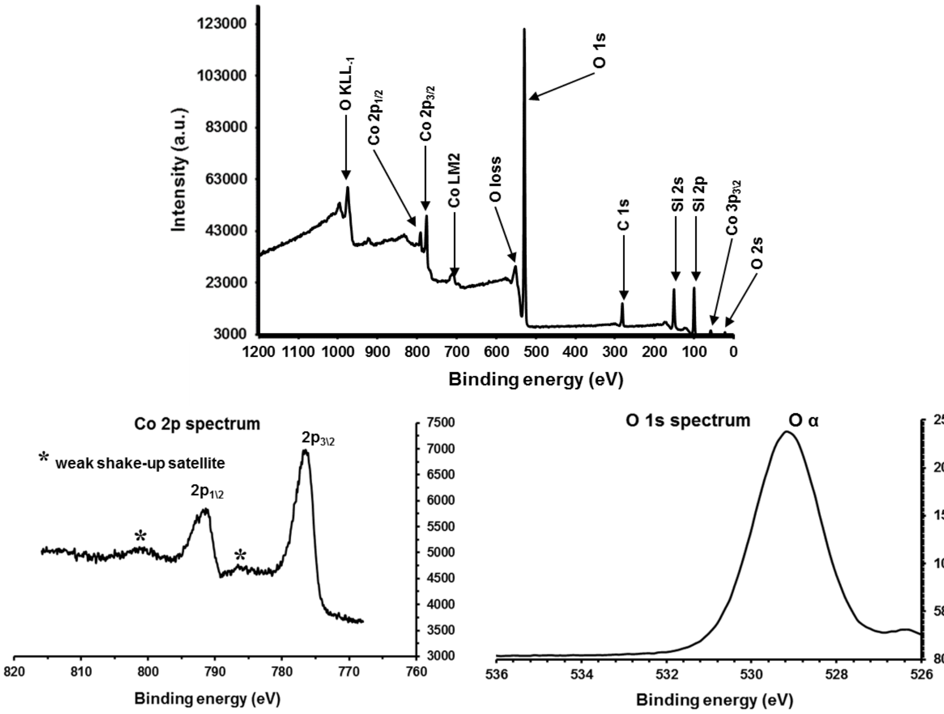

Figure B.3: XPS profiles of wide spectrum, Co 2p and O 1s in the Co_3O_4 NaOH nanosheets

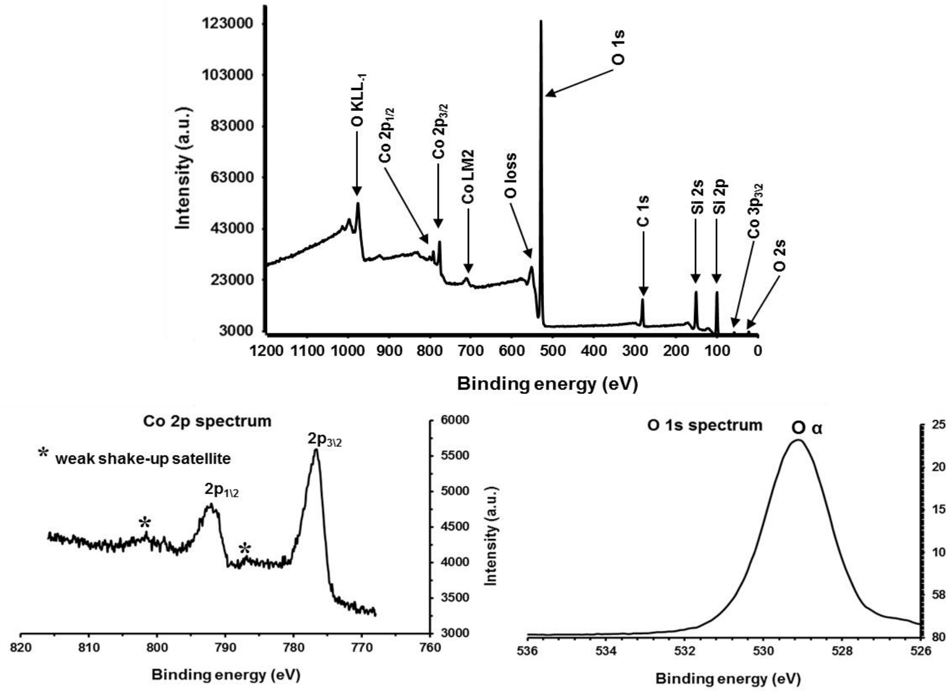

Figure B.4: XPS profiles of wide spectrum, Co 2p and O 1s in the Co_3O_4 nanobelts

Plagiarism declaration

This thesis/dissertation has been submitted to the Turnitin module (or equivalent similarity and originality checking software) and I confirm that my supervisor has seen my report and any concerns revealed by such have been resolved with my supervisor.

Motlokoa Khasu

Signed

………………………